Wind Energy Potential Prediction and Investigation of Aerodynamic Effects of Surface Dimples over the surface of Wind Turbine Blade

M.Sc. Thesis

By

Gedyon Fikade Alemu

Thermal and Aerospace Engineering Program

School Of Mechanical, Chemical and Materials Engineering

Adama Science and Technology University

Adama, Ethiopia

September, 2019

Wind Energy Potential Prediction and Investigation of Aerodynamic Effects of Surface Dimples over the surface of Wind Turbine Blade

A Thesis Submitted to Thermal and Aerospace Engineering Program of School of Mechanical, Chemical and Materials Engineering, Adama Science and Technology University in partial fulfillment of the requirement for the award of degree of **Master of Science in Thermal Engineering**

By

Gedyon Fikade Alemu

Advisor**: Dr Addisu Bekele**

Adama, Ethiopia

September, 2019

APPROVAL OF BOARD OF EXAMINERS

We, the undersigned, members of the Board of Examiners of the final open defense by Gedyon Fikade Alemu have read and evaluated his thesis entitled "**Wind Energy Potential Prediction and Investigation of Aerodynamic Effects of Surface Dimples over the surface of Wind Turbine Blade**" and examined the candidate. This is, therefore, to certify that the thesis has been accepted in partial fulfillment of the requirement of the Degree of Master of science in Thermal Engineering.

…………………….	…………………….	……………………….
Chair Person	Signature	Date
…………………….	…………………….	……………………….
Internal Examiner	Signature	Date
…………………….	…………………….	……………………….
External Examiner	Signature	Date

DECLARATION

I hereby declare that this M.Sc. Thesis entitled "Wind Energy Potential Prediction and Investigation of Aerodynamic Effects of Surface Dimples over the surface of Wind Turbine Blade" in partial fulfillment of the requirement of the degree of Master of Science in Thermal Engineering is an authentic record of my own work carried out from September 2018 to September 2019 under supervision of Dr. Addisu Bekele, Assistant Professor of Thermal Engineering program, Adama Science and Technology University.

The matter embedded in this thesis has not been submitted for the award of a degree or diploma in any other university. All relevant resource information used in this paper has been duly acknowledged

…………………. ………………. ……………………..

Student name signature Date

This is to certify that the above statement made by the candidate is correct to the best of my knowledge and belief. This has been submitted for examination with my approval.

…………………. …………………… …………………………..

Advisor signature Date

ACKNOWLEDGEMENT

Foremost, I would like to address my deep gratitude for the Almighty Holy-Savior, whom have never cease his mercy and blessing up on me. Besides to God, I would like to express my sincere gratitude to my thesis advisor Dr. Addisu Bekele for his continuous support, motivation and guidance on this study. His guidance help me in all of the time of research and writing of this thesis. My sincere thanks also goes to Adama Science and Technology University for offering me a scholarship of Master's program, for all coordinators in Col. John C. Robinson American Center for their support and inherent advice while preparing the physical models, Thermo-fluid lab assistants for their intense advice while conducting Experimental work. Last but not the least, I would like to thank my family and friends: my parents Fikade Alemu and Sofia Abrar for their support by giving me tremendous love, advices and financial support across the study.

ABSTRACT

Wind energy is one of the fastest growing sectors in Renewable Energy. Wind turbine is a device that transduce kinetic energy from the atmosphere (wind) into electrical energy. The main purpose of this study is to present and perform an investigation on the **wind energy** potential of an area named **WETER** (9.222^0 latitude, 41.790^0 longitude), Horizontal Axis Wind Turbine (HAWT) blade design and investigation of the aerodynamic effect of **surface dimples** over the wind turbine blades.

Wind data collected from Diredawa Metrological station and satellite's wind data over a period of ten years of the region were used in order to figure out the wind energy potential of the site. Analytical result of the potential assessment is used as an input for blade design. Among the different methods of blade design, Blade Element Momentum (BEM) theory is used to optimize the chord and twist distributions of the blades. National Renewable Energy Laboratory's (NREL) **S830** wind turbine airfoil is selected for the blade design. The aerodynamic performance of the designed blade is examined using Computational Fluid Dynamic (CFD) analysis; Due to its ability to capture flow separation and accuracy, Large Eddy Simulation (LES) transient turbulence model is preferred and implemented using ANSYS-FLUENT.A number of dimple configuration were added on both pressure and suction side of the blade surface and their corresponding effect on the aerodynamic performance is studied.

Experimental investigation on scaled down S830 model is carried out using a sub-sonic **wind tunnel** for validation. 3D printing technology was used to manufacture two HAWT airfoils with dimple and without dimple. The result of these studies reveals that the intended site have a tremendous wind energy potential to install a wind farm with a mean annual wind power density ranging from 458.96 W/m^2 to 663.63 W/m^2 and with prevailing wind direction of South-East-South (SES). The designed blade have a rated power output of 0.5MW with a power extraction coefficient (C_p) of 0.41, while the numerical and experimental study result of dimpled wind turbine shows some dimple arrangement will enhance the **aerodynamic performance** by delaying flow separation. The computational result illustrate dimpled HAWT blade have 6.78% increment in Energy capturing efficiency.

Keywords*:* **WETER, Wind Energy, S830, Wind Turbine Blade, surface Dimple, Aerodynamic Performance, Wind Tunnel.**

TABLE OF CONTENT

Content Page Number

LIST OF TABLES

LIST OF FIGURE

ACRONYMS

ADM	Actuator disc model
AOA	Angle of attack
ABL	Atmospheric Boundary Layer
BEM	Blade Element Momentum
CFD	Computational Fluid Dynamics
CONFIG#1	Dimple Orientation One
CONFIG#2	Dimple Orientation Two
CONFIG#3	Dimple Orientation Three
CONFIG#4	Dimple Orientation Four
CONFIG#5	Dimple Orientation Five
CONFIG#6	Dimple Orientation Six
DES	Detached Eddy Simulation
DNS	Direct Numerical Simulation
GOE	Government of Ethiopia
HAWT	Horizontal Axis Wind Turbine
K-ε	Turbulence Model
K-ω	Turbulence Model
K-ω SST	Turbulence model
LES	Large Eddy Simulation
MCP	Measure Correlate Predict
MEXICO	Model Experiments in Controlled Conditions
MOFAOD	Ministry of Foreign Affairs of Denmark
NACA	National Advisory Committee of Aeronautics
N-S	Navier-Stokes
NREL	National Renewable Energy Laboratory
RE	Renewable energies
RANS	Reynold Average Navier-stoke equation
RSM	Reynold Stress Model
WECS	Wind energy Conversion Systems
SGS	Sub-grid scale
S809	HAWT airfoil
S830	HAWT airfoil
S827	HAWT airfoil
SG6041	HAWT airfoil
SG6050	HAWT airfoil
SE 7715	SANY wind turbine
VAWT	Vertical Axis wind turbine
WTG	Wind Turbine Generator

WRF-Weather Research and Forecasting

WASP- Wind Atlas Analysis and Application Program.

SYMBOLS

Φ	Angle of twist (^{0} degree)
(**α**)	Angle of attack (^{0})
AEP	Annual Energy Production (GWh)
CF	Capacity Factor
C	Closure coefficients
C	Chord Length (m)
ρ	Density (kg/m^3)
Cd	drag coefficient
U_{wd}	Design wind speed (m/s)
μ_t	Eddy Viscosity(kg/ms)
ED	Energy Density (kJ/m^2)
Θ	Fluid domain
$\psi(x,t)$	–flow variable
G	Filter function
Z	Height (m)
ν	Kinematic Viscosity (m^2/s)
$^L/_D$	Lift–To–Drag Ratio
r-	Local radius (m)
C_L	Lift coefficient
$\bar{U}_i$	Large-scale filtered component
$\bar{\psi}(x,t)$	– Large scale filter function
λ_r	Local Tip Speed Ratio
l mix	Mixing Length (m)
Vm	mean wind velocity (m/s)
N	Number of Wind data
NB	Number of blade
Copt	Optimum Chord length (m)
Cp	Power coefficient
p	– Pressure (N/m^2)
F (V)	probability density function
V_{ref}	Reference Velocity (m/s)
K	Shape Factor
Re	Reynold Number
A	Swept Area (m^2)
Δx	Spatial Step (m)
z_{ref}	Reference height (m)
R	radius (m)
Ω	–rotational speed (rpm)
C_S	Smagorinsky constant
τ_{ij}	Stress tensor
$\psi'(x,t)$	Subscale filter function
τ_{sgs}	Sub grid scale stress
μ_{sgs}	-SGS eddy viscosity
z_o	Surface roughness length of the site
δ_v	Standard deviation
TSR (λ)	Tip speed ratio
Δt	Time step (s)
V	Wind speed (m/s)
P_V	Wind power (W)
u	X Component Speed (m/s)
V	Y Component Velocity (m/s)
y^+	Y plus
W	Z Component Velocity (m/s)

CHAPTER ONE

INTRODUCTION

1.1 Background

Energy is a prominent factor; which express the wealth or development level of a nation. Ethiopia possess a lot of natural resources; nevertheless they are not harnessed in adequate manner, as a consequence Ethiopia is categorized under undeveloped nation's category. In 2014/15 G.C, Ethiopia had a total amount of power generating capacity of 4,180 MW; among this 93.4 % from hydro-potential, 0.04% from wind energy remaining from fossil fuel and biomass. The Government of Ethiopia (GOE) had planned for an expansion of its wind power capacity to 5,200 MW by 2020 to be developed through the private sector, i.e. by Independent Power Producers. (MOFAOD, 2016).

Renewable energies (REs) represent a foundation to steer our energy system in the direction of sustainability and supply security and a wide set of different RE technologies and resources occur today. The worldwide requirement for renewable energy is growing rapidly because of the climate setbacks and limited amount of oil resources. The contemporary focus on discovering solutions for mitigating global warming has resulted in renewable energy technologies gaining importance. Wind energy appears as a clean and good solution to cope with a great part of this energy demand; Among the renewable energy technologies, wind power is one of the fastest growing technologies globally at an average annual growth rate of more than 26% since 1990. (Usha et al., 2009) As it's expressed previously Ethiopia's primary source of energy is renewable energy, among them wind have a part of only 0.04 %, generated from four wind farms across the country. Developed nations like Denmark generate *42*% of total consumption from wind energy. (MOFAOD, 2016) Figure 1.1 shows an average wind speed contour of Ethiopia.

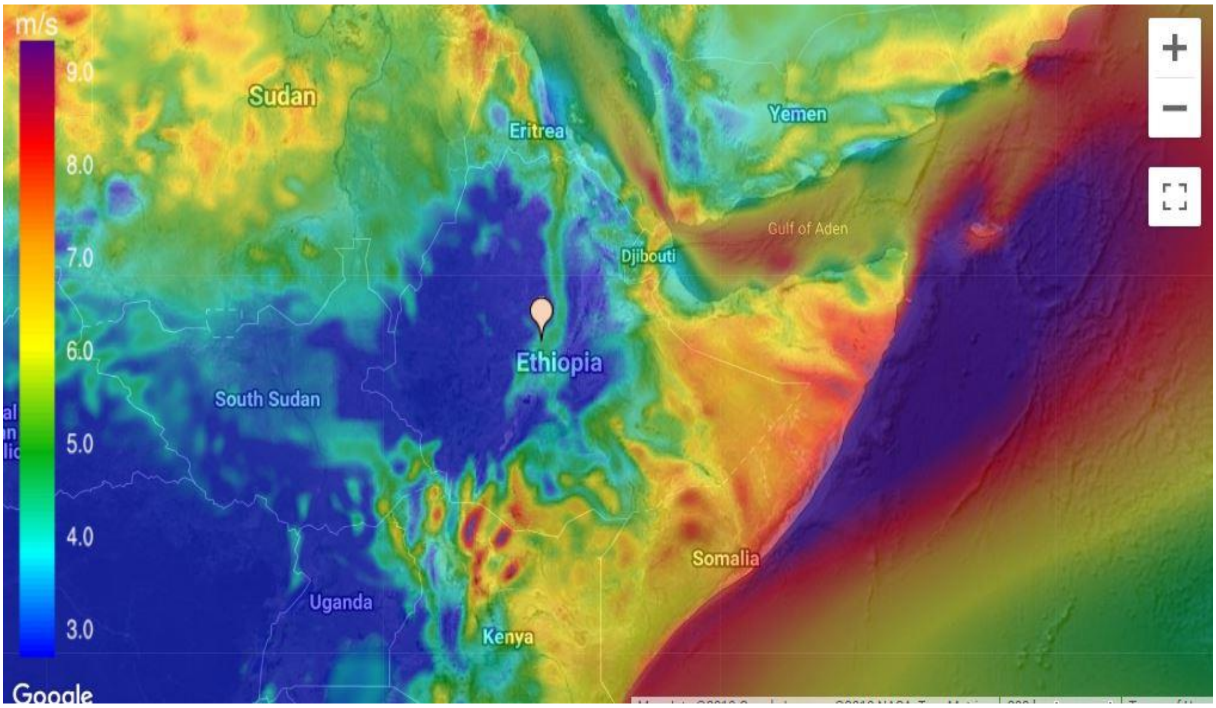

Figure 1.1: Annual Average Wind Speed Contour of Horn of Africa (Vortex Interface 2019)

Wind exist everywhere in the universe. As long as the Earth continues to impart the right conditions, it will remain that way. All it takes is a difference in pressure to get a mass of air moving. This movement of air from areas of high pressure to areas of low pressure is what generates wind. Because this mass of air is moving, it has energy, renewable energy that has been consumed to give thrust to sailboats and ships crossing the oceans, to windmills used to pump water for irrigation or grinding up grain. It is believed that the earliest windmills were invented 2000 years ago by the Persians and also by the Chinese and were used to grind corn and also to lift water. Later the Dutch develop windmills to drain their land in the 14th century and, by the 19th century, millions of small windmills were installed in the United States. The 19th century also saw the development of small wind machines (0.2 - 3 kW producing 32 V direct current) in countryside regions in America to operate appliances. The generation of grid electricity, using wind turbines, has its origins in the United States in the 1970s (Hansen and Butterfield, 1993). Even today, wind is still harnessed for much the similar reason as it was thousands of years ago. Today, only a small fraction of the world's electricity is generated by wind. (Hansen and Butterfield, 1993)

A new market in wind energy technology has emerged that has the means of efficiently transforming the energy available in the wind to a useable form of energy, such as electricity. The cornerstone of this anew technology is the **wind turbine**.

A wind turbine is a device that transduce kinetic energy from the atmosphere (wind) into electrical energy. Two major types of wind turbines exist based on their blade configuration and operation. The first kind is the horizontal axis wind turbine (HAWT). This kind of wind turbine is the most common and can often be seen littered across the landscape in areas of relatively level terrain with predictable year round wind conditions. HAWT's sit atop a large tower and have a set of blades that rotate about an axis parallel to the stream direction. These wind turbines have been the main subject of wind turbine research for decades, mainly because they share common operation and dynamics with rotary aircraft. A combination of the lift and drag causes the rotor to spin. This turns the generator and makes electricity

The second major type of wind turbine is the vertical axis wind turbine (VAWT). This kind of wind turbine turn around an axis that is perpendicular to the oncoming stream; hence, it can take wind from any direction. VAWTs consist of two major kinds, the Darrieus rotor and Savonius rotor. The Darrieus wind turbine is a VAWT that turn around a central axis due to the lift produced by the rotating airfoils, whereas a Savonius rotor turn around due to the drag created by its blades. There is also an innovative kind of VAWT emerging in the wind power industry which is a mixture between the Darrieus and Savonius designs.

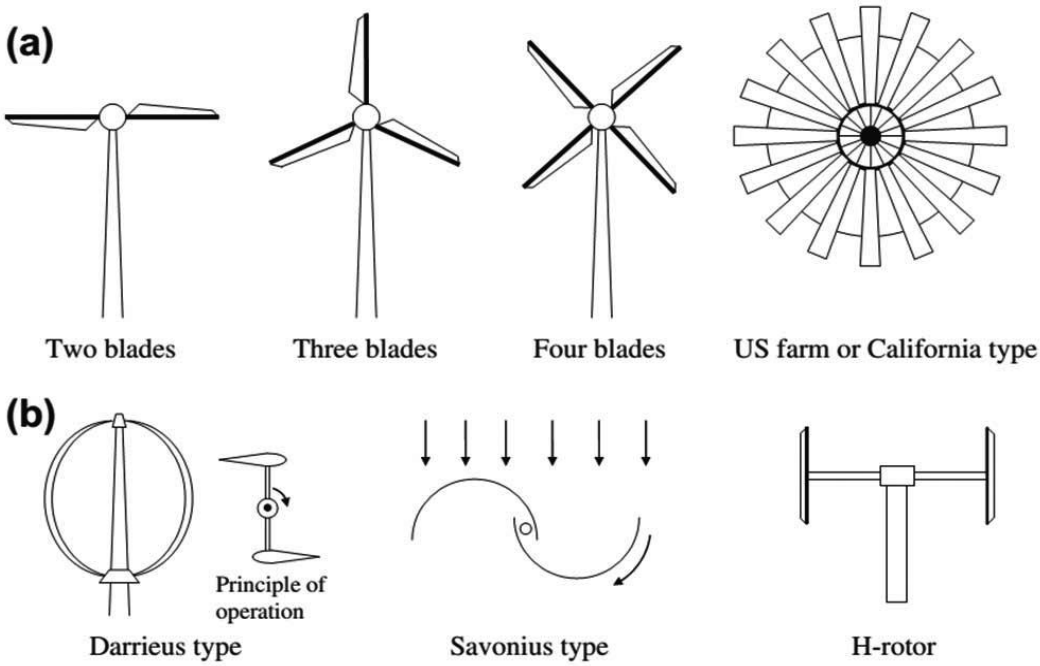

Figure 1. 2 a) Type of HAWT B) Type of VAWT (Kalogirou, 2014)

Each variety of wind turbine has its strengths and weaknesses, nevertheless in the end, all wind turbines accomplish the same task The amount of power extracted by a wind turbine is proportional to the cube of the wind speed, V, and is directly proportional to the swept area of the rotor "A", so the bigger blade the more power can be extracted

$$p = \frac{1}{2}\rho v^3 ACp \quad \text{………………………………………….. …… .. (1.1)}$$

C_P, is a measure of aerodynamic performance for a wind turbine. It represents the fraction of kinetic energy streaming through the swept area of a wind turbine that is transduced into mechanical energy. It depend upon the aerodynamic performance of the wind turbine blade.

Physical description of lift

The physical description of lift is based primarily on Newton's three laws and a phenomenon named the Coanda effect (David and Scott, 2001). Lift is recognized as a reaction force, that is, wings develop lift by diverting air down. Newton's first law states "A body at rest will remain at rest, and a body in motion will continue in straight-line motion unless subjected to an external applied force." In the context of flight this means that if an object (such as a mass of air), initially motionless, starts to move, there has been force acting on it. Likewise, if a stream of air bends (such as over a blade), there also must be a force acting on it. Newton's third law can be stated as "For every action there is an equal and opposite reaction". By Newton's third law, the air must be putting an equal and opposite force on whatever is bending it, in this situation the blade. Then by using Newton's second law the lift force (or thrust) generated is equal to the amount of air expelled per time, times the velocity of that air.

The Coanda effect has to do with the bending of fluids around an object. Because of viscosity when a moving fluid comes into contact with a solid object, some of it sticks to the surface. A small distance from the surface the fluid has a small velocity with respect to the object. The transition layer between the surface and the fluid at the uniform flow is named the boundary layer. Hence for device which will depend up on the lift force the fluid element should bend by clinging on the solid surface.

1.2. Statement of the Problem

Energy is one of the essential inputs for economic development and industrialization; Because of environmental pollution problems and economics benefit of fuel saving; there has been a growing interest in renewable energy sources, especially in the wind energy conversion systems (WECS). The preliminary stage for harnessing wind energy is assessing the sites' wind energy potential. Diredawa is a city located at eastern part of Ethiopia .The primary source of electric energy for the city is from diesel power generation; meanwhile have a tremendous wind energy potential. The intended site is located on southern periphery of the city at a longitude and latitude of 9.222^0 and 41.790^0 respectively.

Wind power must be rapidly further deployed for addressing the current environmental challenges associated with the generation of electricity. This necessitates reliable and cost-effective wind turbines. In this thesis site specific aero dynamical design of wind turbine and wind energy potential estimation based on data from satellite and National Metrological institute is conducted. .

According to the analysis of Lanchester and Betz the maximum possible amount of energy extraction from a wind by wind turbine is 59.3% of the incoming kinetic energy (Betz, 1930). Nevertheless, most wind turbines can't achieve this efficiency. The common challenge for the wind turbine designer is to maximize the energy capture within the given restrictions (White, 1997). Wind turbine rotor blades are made by stacking airfoils along the blade span. The main incentive of blade rotation is the lift force created by pressure difference in the flow over of airfoils. Contemporary research findings reveal that dimples on the surface of aircraft's airfoils enhance the aerodynamic efficiency and maneuverability of the aircraft by mitigating stall. (Deepenshu, 2012, Livya, et al., 2015). Even though airfoil of aircraft and wind turbine have a distinct difference; from these finding it's possible to predict, dimples can also enhance the power extraction coefficient of wind turbine. This thesis investigate suitability of dimples for HAWT blade.

1.3. Objective

1.3.1. General Objective

The general aim of this thesis is wind energy potential prediction of a site named WETER; located at eastern part of Ethiopia and investigation on aerodynamic effect of surface dimples over wind turbine blades for efficiency enhancement.

1.3.2. Specific Objective

The general objective will be demonstrated via the achievement of the following specific objectives

- Analyze the wind data of the site and estimate the power density.
- Design wind turbine blade based on the wind phenomena.
- Examine the aerodynamic characteristics of the designed blade.
- Examine the aerodynamic effect of dimples on surface of wind turbine blade.
- Compare the power extraction coefficient for the baseline and dimpled turbines.
- Experimentally evaluate and validate dimple effect on scaled downed wind turbine airfoil.

1.4. Scope and Limitation of the Study

1.4.1. Scope of the Study

This thesis is mainly devoted to the study of the flow over wind turbine blades by means of Computational Fluid Dynamics (CFD) simulations and experimental work. Special attention is paid to the study of the dimple effect at different size and orientation on regions of the rotor blades, the scope can be summarized in the following points.

- Analytical estimation of wind potential of the site
- Analytical design of wind turbine blade using BEM
- Numerical simulation of HAWT blade with dimples and exempting dimples.
- Experimental work on subsonic wind tunnel

1.4.2. Limitation of the Study

- The wind data source is merely from one metrological mast and satellite data from vortex interface.
- Experimental evaluation is not conducted on full scale wind turbine blade.
- This thesis do not investigate the aero-acoustic and aero-elastic effect of dimples on HAWT blade.

1.5. Significance of the Study

- Examine the suitability of the site for wind farm application.
- Provide a way to enhance the aerodynamic efficiency of wind turbines, hence maintain an efficient wind farm.
- Fill the Scientific gap of examining the consequence of dimples at wind turbine blades.

1.6. Thesis Overview

This thesis is divided into seven chapters. The opening chapter describes the motivation, key concepts and principles for the research described in this thesis. Chapter 2 involves a literature review covering previous theoretical, experimental and numerical work on wind energy potential assessment, HAWT blade design and aerodynamic effect of dimple. Concentrating on current numerical methods and the theory following the methods used in this thesis. From Chapters 3 up to chapter 5 describes approaches followed to conduct the three studies; these are potential assessment, blade design and dimple effect investigation on wind turbine blade. Chapter 6 details the results and discussion of the studies, described in Chapter 3,4, and 5 .Finally, Chapter 7 presents the major conclusions of the work conducted in this thesis, highlighting the findings and concluding with recommendations for further work.

CHAPTER TWO

LITERATURE REVIEW

2.1 Wind Energy Potential Assessment

The subsequent section reviews preceding works on wind energy potential assessment technique and assessment findings of local and foreign researches.

The Government of Ethiopia has prearrange to scale up and diversify the Renewable energy mix, to lessen hydropower dependency; consequently the focus has been shifted to Renewable energy sources to fulfill the demand. The Ethiopian Government had prepared a Master Plan for wind and solar energy for investigating at hand wind and solar energy resource that suggest the major policy options to be developed for wind and solar energy expansion along with recommendation of 51 wind projects having an aggregate planned capacity of 5,280 MW. (MOFAOD, 2016)

A wind potential survey has been performed at Adama I site and Wind Farm has also been constructed, in the course of the feasibility study, taking into account data from on-site measurement stations. In January 2005, a 10 m measuring mast was installed during the campaign for identification of promising wind potential sites in Ethiopia. Nazareth was considered as a site with favorable wind conditions and second mast been erected in September 2005, equipped with anemometers at 10 m and 40 m above ground level height and a wind vane at 10 m height in order to determine the wind conditions close to the hub height of the wind turbines. (GTZ, 2006)

To impart additional data for validation of the measurements, a third anemometer was established in January 2006 at the nearby. All metrological masts have been equipped with first class cup anemometers to predict the long-term wind speed at Adama I site, long-term correlations using MCP (Measure-Correlate-Predict) method have been performed, and using NCEP (US-National Center for Environmental Prediction) reanalysis wind data of a period of 25 years. The findings of these correlations were adapted to the measured wind speeds in order to make them long-term representative. Additionally, the NCEP data were used for validation of the calculated wind resources. The calculations of energy production are executed by means of the wind resources collected by the wind measurements. Wake effects between the wind turbines were taken into account by applying the PARK model that is integrated in the international standard Wind Park planning software Wind-Pro.

Figure 2.1: Adama I Wind Farm (Kasahun, 2014)

The wind potential assessment at Ashegoda site has been performed by means of the feasibility study, taking into account data from two measurement stations on-site; the first one of 10 m height erected in January 2005 and the second one with anemometers at heights of 10 m and 40 m above ground level, erected in mid-September 2005. Both masts had been equipped with THIES first class cup anemometers and a wind direction vane (at 10 m above ground level). The calculations for the expected energy yield at Ashegoda Wind Farm, that is based on the long-term corrected measured wind data, are executed by means of the international standard Wind Park planning software combination of WindPro and WAsP With all the methods and also the requirements to conduct and implement wind power assessment and developing the wind Farm, HCIE in a joint-venture with Chinese construction group HydroChina-CGCOC completed a 51MW plant near Nazareth (Adama), equipped with 34 GoldWind 1.5MW turbines and very recently French turbine manufacturer Vergnet had built a 120MW project at Ashegoda using Vergnet and Alstom turbines and also HCIE is developing a 51MW project at Messebo-Harena. *(*GTZ, 2006*)*

Kasahun (2014), Estimation that has been undertaken in order to quantify the wind resource available at Adama II Wind Farm using the Wind Atlas and Application Program (WAsP). It was made through retrieving the data measured by anemometer and wind vanes at Kusaye site that is stored in a data logger from 16/11/2011 to 9/12/2012 at 70 meters above ground level. The end results of the assessment presented that the prevailing wind direction is ENE direction with more than one third of wind is blowing in ENE. From the recorded data at 70 m, the mean wind speed at 50 m is estimated to be 8.22 m/s, at the mast location for a single WTG the wind power density is 452 W/m^2 and the Gross Annual Energy Production ranges from 1.5 to 11.99 GWh at 70 m height. Placing the 102 SE7715 WTGs in accordance with the proposed layout at the Wind Farm, the Gross Annual Energy Production is 664.745 GWh and net AEP at the site is 403.669 GWh.

Mengesha (2015), conduct study at Aysha Wind Farm with the aim to analyze its wind energy resource based on 10 minute mean data for the year 2008 G.C. Using different software and statistical model, the wind data has been analyzed to: select wind turbine class, power density & estimate farm AEP, develop site wind resource map and perform preliminary turbine micro-sitting. Based on the analysis and site survey, site roughness and wind shear exponent are also determined. As per the preliminary analysis of the farm based on the selected turbine, total gross AEP of 1819.21 GWh and total net AEP of 1183.62 GWh have been found. In addition the average power density and capacity factor (CF) at the wind farm are estimated at 1392.6 W/m^2 and 44.92 %, respectively. Moreover the mean wind speed at hub height (67 m) is 11.83 m/s whereas the average Weibull shape factor (k) and scale factor (A) are estimated at 3.13 and 13.22 m/s, respectively

Abdoulkader *et al.*, (2019), for the first time, examines wind energy potential at Djibouti-city using 5-years (2014–2018) wind speed data collected at 10 m height of wind power using Weibull parameters. Such a study was not feasible before due to the lack of data in this urban area. The end results showed the possibility to implement and develop urban wind energy sector in Djibouti-city for domestic applications. The statistical wind speed, the wind rose, and the power density were computed. According to the analysis of wind power production, Djibouti-city needs to install the wind turbines with high hub height greater than 80.5 m for efficient harvesting

Nikolai, (2014) Downscaling simulations performed with the Weather Research and Forecasting (WRF) model were used to determine the large-scale wind energy potential of Iceland. Local wind speed distributions are represented by Weibull statistics. In addition to seasonal and spatial variability, differences in average wind speed and power density also exist for different wind directions. Along the coast in winter, power density of onshore winds is higher by 100 -700 W/m^2 than that of offshore winds. Based on the end results, 14 test sites were selected for more detailed analyses using the Wind Atlas Analysis and Application Program (WASP).

Liaquat, (2013) carried assessment of wind potential for the coastal area of Jiwani, (Pakistan) and consequently steps are suggested to optimize the wind turbine blade for effective utilization of the available wind energy through numerical modeling and simulation Four years wind data of the Jiwani was collected and based upon the available data wind turbine blade was designed and optimized for maximum power output for that area.

Shu *et al*., (2015); have done the statistical analysis of wind characteristics and wind energy potential in Hong Kong. Among all the available probability distribution functions, the Weibull distribution is undoubtedly one of the most frequently applied models for the statistical analysis of wind characteristics and wind energy potential assessment. The advantages of the Weibull distribution function have been well addressed by Hennessey (1977). Hennessey (1977) stated that the Weibull distribution model not only impart good representation for wind speed distribution, it also contributes to an easy estimation of the mean and standard deviation of the total wind power density. This paper ends its work by mentioning the end results obtained from the methods and calculation of the necessitated parameters like wind power density

Ozgur, (2006) in this study, wind characteristics have been analyzed in Kutahya, Turkey. Characteristics such as annual, seasonal, monthly and diurnal wind speed, and wind direction variations are examined between July 1, 2001 and June 30, 2004. A practical assessment has been made of the electricity generation using ALWIN program for the wind turbines that have different sizes between 300 and 2000 kW rated power. The energy production analysis showed that the average wind speed, that indicates the suitability with small size wind turbines, produces electricity to fulfil the deficient electric power during the peak hours.

Bharani *et al.*, (2019) creates collection of dataset to calculate the wind energy potential in the selected location across India using large volume of wind dataset. The wind energy potential data were collected at 100 m height from MSL (Mean Sea Level) from 2014 to 2016. The wind speed and direction were used to analyze wind energy characteristics and suitable site for wind turbine installation. The maximum wind power density was observed at four different monitoring sites. Based on the outcome the paper come across a conclusion of “The altitude of the monitoring station and geomorphology of the site significantly controls the wind power density”.

Belabes *et al.*, (2015) have studied evaluation of wind energy potential and estimation of cost using wind energy turbines for electricity generation in north of Algeria. A practical assessment has been made for the generation of electricity using wind turbines at six sites. They have used power law for extrapolation to obtain the wind speed at the highest by using the surface roughness coefficient value that is 0.143. Various kinds of wind turbines were selected with various characteristics and have able to find wind energy output that can be produced by wind turbine. It was concluded with amount of energy or power that could be produced by wind turbines.

2.2 Wind Turbine Blade Design

Mulugeta, (2009) studied computer-aided aerodynamic and structural design of horizontal axis wind turbine blades. In his paper detailed review of the designing horizontal-axis wind turbine (HAWT) blades to achieve satisfactory levels of performance starts with knowledge of the aerodynamic forces acting on the blades and HAWT blade design was studied from the aspect of aerodynamic view. BEM method is selected for the blade design. Additionally the basic principles of the aerodynamic behaviors HAWTs was investigated.

Haseeb *et al.*, (2014) studied on Low Reynolds Number Airfoil for Small Horizontal Axis Wind Turbine Blades. In this Study an approach to design new airfoils for small horizontal axis wind turbines operating at low wind speeds and consequently at lower Reynolds numbers (Re). The so called ‘direct design method’ is employed. Post-design viscous study tool ‘Xfoil’ is used for optimization of the airfoil. The aim is to attain higher values of lift–to–drag ratio (L/D ratio) for the tip of the blades. The new airfoil, named ‘UBD-5494’, was tested in ‘Xfoil’ with Re in the range of 30 000, 55 000, 70 000, and 100000. Each of these situations is analyzed at various angles of attack, ranging from 0 to 20 degrees at one degree increments. Performances of other existing airfoil options are also compared with ‘UBD-5494’. The new airfoil shows distinctively higher efficiency in comparison to other existing airfoils at low Re in terms of Lift-to-drag ratio at its design lift coefficient and is therefore recommended for tip of small horizontal axis wind turbine blades

Siraj, (2011) studied design and analysis of horizontal axis wind turbine rotor**.** In his paper, an optimization model for rotor design of 750 kW horizontal axis wind turbine having the blade length of 21.0 m was presented and S809 airfoil type was used for the blade. The outcome obtained from ANSYS was compared with the existing design.

Peter and Richard, (2012) studied wind turbine blade design. They presented that the detailed review of the current state-of art for wind turbine blade design, including theoretical maximum efficiency, propulsion, practical efficiency, HAWT blade design, and blade loads. The review was provided a complete picture of wind turbine blade design and shows the dominance of modern turbines almost exclusive use of horizontal axis rotors. The aerodynamic design principles for a modern wind turbine blade are detailed, included blade plan shape/quantity, airfoil selection and optimal attack angles, described aerodynamic, gravitational, centrifugal, gyroscopic and operational conditions

Jason, (2011) studied design and experimental testing of small-scale wind turbines. They presented that the increasing environmental and economic cost of fossil fuels, alternative sources of energy were needed. Much of the current wind turbine research focused on large-scale wind turbines. An alternative approach is small-scale wind turbines designed specifically to produce power at low wind speeds. This thesis investigated the design and testing of these turbines. Concerned specific to small-scale design, such as low Reynolds number flow, separation, and low wind speed power generation were addressed. A test apparatus was developed to validate the design procedure, and specific methods to increase power generation under these conditions, such as span wise and axial roughness, two, three, and four-bladed systems and tip-speed ratios of 1, 3, and 7, were investigated

Jonkman et al., (1993) developed a 2D CFD model to calculate the stream field and aerodynamic coefficients of S809 HAWT airfoil and concluded that the standard k-ε turbulence model was not appropriate to model the stream separation on the suction surface of the airfoil. Comparing the SST k-ω model and the Renormalization Group (RNG) k-ε model, their results confirmed that the SST k-ω model can grant satisfactory solutions for turbulent flows.

Freudenreich, (2002) studied both by experiments and CFD modelling using the standard k-ω and SST k-ω models for DU97-W-300 wind turbine airfoil. The SST k-ω model has a better agreement with experimental outcomes than other turbulence models such as the S-A model, the k-ε model and the Reynolds Stress Model (RSM); suggested to use the SST k-ω model with an imposed transition location that was 10 % offset downstream from the predicted point of a fully turbulent model and concluded that the Menter's SST transition model could improve the agreement with experiments

Serhat, (2005) studied computer- aided design of horizontal- axis wind turbine blades. In this paper, HAWT blade design was studied from the aspect of aerodynamic view and the basic principles of the aerodynamic behaviors of HAWTs are investigated. Blade-element momentum theory (BEM) known as also strip theory, that is the current mainstay of aerodynamic design and analysis of HAWT blades, is used for HAWT blade design in this paper. Firstly, blade design procedure for an optimum rotor according to BEM theory is performed. Then designed blade shape was modified such that modified blade will be lightly loaded regarding the highly loaded of the designed blade and power prediction of modified blade was analyzed. When the designed blade shape was modified, it has seen that the power extracted from the wind was reduced about 10% and the length of modified blade was increased about 5% for the same necessitated power.

Wubow *et al*., (2006) investigated the structure of turbulence intensity comparing their outcomes to common empirical methods. Their study focused on the wake structure following a single MW class turbine using both k-ε RANS model and a detached eddy simulation (DES) model. The empirical model investigated casts the turbulence intensity in the far wake as the sum of the upstream turbulence intensity and a bell-shaped turbulence intensity defined as a function of thrust coefficient and the tip-speed ratio. The outcomes of their study gave an idealized modification to the empirical model by casting the additional turbulence intensity as three bell-shaped curves with the primary peaks aligned with the tip vortices.

The k-ε RANS study simulated a previously studied 55 kW turbine with a neutral ABL using a multiple reference frame model in FLUENT. Outcomes were relatively successful at reproducing velocity profiles measurements downstream, yet due to the averaging nature of RANS models the turbulence intensities near the edges of the wake were under-predicted. The DES simulation used a homogeneous ABL to model an ENERCON E66 turbine for which turbulence data was available. This model also produced relatively successful outcomes. The error in the DES model was attributed to boundary influences from a limited domain size. This resulted in an under-prediction of turbulence intensity just outside the wake region.

Tachos *et al*. (2010) performed a parametric study of RANS closure models on the NREL Phase II wind turbine to determine the applicability of RANS closure models. The models used include Spalart-Allmaras (SA), k-ε, k-ε renormalization group (RNG), and the k-ω shear-stress transport (SST) closure models. The simulation was set up using a single blade from the NREL Phase II turbine in a single reference frame with 120˚ periodic boundary conditions. As a perspective of the size and computation time, the mesh was 4.2 million cells and the k-ω SST model took the equivalent of 20 days of central processing unit (CPU) time. The model was run as steady state in FLUENT. The means of validation used was pressure distribution on the blade surfaces. They found that the k-ω SST model had a very good correlation with measured values. The k-ε RNG and SA models had fairly good correlation. The miscorrelations found were determined to be an outcome of flow separation. The k-ε closure model performed very poorly, likely as a result of its lack of an explicit term to account for rotation. Overall it was concluded that because of the near wall formulation, the k-ω SST model was the most suited RANS turbulence closure model for wind turbine simulations.

Porté-Agel, *et al*., (2011): Even if RANS simulations can achieve accurate and meaningful outcomes they only calculate the mean flow and parameterize the scales of turbulence for more accurate and descriptive results LES simulations are necessitated. LES models employ a filter based on grid size so that where the mesh is fine enough the stream is resolved, similar to direct numerical simulation (DNS), and where the mesh size is too coarse, a SGS turbulence closure scheme is employed to model the flow. Following this performed a LES study using a tuning-free Lagrangian dynamic SGS model recently developed for wind energy applications to model both single turbine wakes and wake interactions in an operating wind farm. Fully resolving a rotating wind turbine significantly increases CPU time and model complexity. As a means of simplifying the model and cost savings, an actuator disk model (ADM) can be implemented to act as a momentum sink with properties mirroring that of a wind turbine.

As these literature reviews illustrate, there are many different numerical solutions to the Navier-Stokes equations that have been implemented successfully for HAWT. Of the RANS closure models, the k-ω SST model was seen to have the most success. With respect to LES, the tuning-free SGS models were the most widely employed. Conversely, LES necessitates a very fine grid resolution to not over burden the SGS model. A method to mitigate large mesh sizes is the widely employed actuator disk model (ADM). A variety of ADMs exist, but the best results were found among those formulated using the BEM method over a disk or actuator lines.

2.3 Concept of Dimple

The Concept of dimples arrive from golf balls. Golf balls have inner dent in form of dimples on their outer surfaces. These dimples aid golf balls to lower drag. Drag is resisting force from air. A liquid streaming over a protest tends to drag the question along its stream bearing. A question going through a liquid that is stationary there is a tendency to back the protest off. For a stationary question in a liquid that is streaming there is an inclination to move the protest in the liquid streaming heading. This tendency of streaming liquid is known as drag. As dimples reduce drag of golf ball they can be useful on reducing wings drag. That grows the attention of several researchers about dimple. There were a lot of experiments and numerical investigations have been conducted by several researchers around the world on dimpled effect on airplane wings, golf ball and as a way to enhance heat transfer.

2.3.1 Dimples on Golf Ball

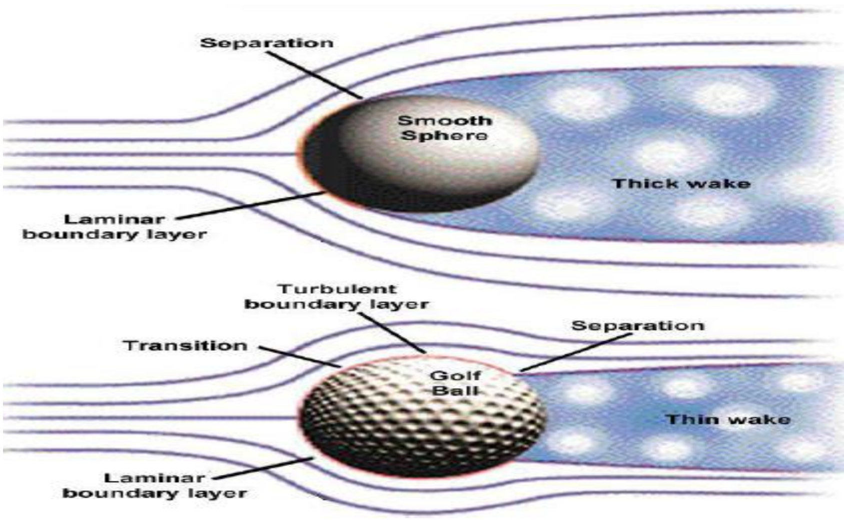

Figure 2.2: Dimple Effect on Golf Ball (Burger, 2006)

Josué, (2006) test the effects of dimples on the magnitude of the drag force that is exerted on a golf ball during flight. The outcomes of the tests demonstrate that the presence of dimples on a golf ball cause it to experience drag forces that are smaller than those on a smooth ball of the similar diameter.

Harun, (2016), examines the aerodynamic consequence of dimple depth on golf balls.3D printing technology was employed to manufacture 11 balls with varied dimple depth. RMIT Aero Wind Tunnel was employed to measure the drag forces over a range of wind speeds. It was found that the drag coefficient of golf ball varied significantly due to varied dimple geometry. The outcomes indicate that the increase of the dimple depth ratio or surface roughness of the golf ball can shift the transition to a lower Reynolds number and increase the drag coefficient in Trans-critical regime. The outcomes also established a positive linear correlation between relative roughness and drag coefficient.

2.3.2 Dimples on Aircraft

Deepenshu, (2012); presents a research paper on Flow Control over Airfoils using Different Shaped Dimples at International Conference on Fluid Dynamics and Thermodynamics Technologies. He performed a CFD investigation in 3-D by taking a fragment of the airfoil with one dimple on it. He prepared his CAD model using CatiaV5 R18 and simulations were carried out in Comsol 3.4 and Comsol 4.2a.His outcomes were in agreement that dimples at first glance on wing model does not influence the weight drag much since it is now streamlined fit as a fiddle conversely it can influence its optimal design when the airfoil is at various angle of attack. This venture confirms if the dimples that decrease a golf ball's drag, can additionally modify stream elements around airfoil for better streamlined productivity.

Moses *et al.*, (2016); published their research paper "CFD study on aerodynamic consequences of dimples on aircraft wings" in International Journal of Engineering & Science Research. There venture likewise includes in decreasing the take-off separation by accomplishing high Coefficient of lift at higher angle of attack. Their computational analysis outcomes have bear the following conclusions for Boeing 737 wings.

- ✓ The dimples at 25 % C are capable of increasing the angle of stall but with less Coefficient of lift.
- ✓ The dimples at 75 % C are capable of increasing Coefficient of lift but angle of stall is unchanged.
- ✓ The dimples at 50 % C are capable of increasing Coefficient of lift as well as angle of stall.
- ✓ Thus Inward round dimple of diameter 0.1mm at 50 % C would give better performance.

Booma *et al.*, (2016) published their article on Computational Analysis of Cavity Consequence over Aircraft Wing in International Journal of Mechanical, Aerospace, Industrial, Mechatronic and Manufacturing Engineering. For their study the wing was demonstrated in CATIA V5R20 and examinations were done utilizing ANSYS CFX. Triangle and square shapes dimples were considered. They show that efficiency improvement can be achieved by improving the maximum lift co-efficient or by reducing the drag co-efficient. Their computational outcomes demonstrate an expansion in lift. Presentation of dimple is a powerful controlling strategy to increment in angle of stall and lift coefficient

Yanfeng *et al.*, (2016) conduct preliminary experiments to investigate the consequence of dimpled surface on the performance of linear cascade on gas turbine engine. Two dimple configurations with a diameter of 1.0mm and a depth-diameter ratio of 0.2 that were located in 30 % - 60 % and 75 % - 95% axial chord lengths of suction side respectively were studied to validate their effectiveness in reducing total pressure loss. Incidence angles of -5.3°, 0°, 5.3°, 7.5°, 10° and inlet Mach number of 0.4 were employed in each experiment with 1.5% Tolerance. Total pressure loss coefficients and blade loading force measurements were made on the dimpled blades by a mini 5-hole pressure probe and compared to the smooth blades. The experimental end results show that the reduction of the total pressure loss coefficients of dimpled blades is obvious at the incidence angle of 0°, 5.3°, and 7.5°, and the change of the total pressure loss coefficients of dimpled blades is very slight at the incidence angle of -5.3°, and 10°. In addition, there exists a slight increase of loading force with dimpled blades. The comparison end results also indicate that dimples on 30%-60% of suction side is more effective in loss reduction than that on 75% - 95% of suction side at all incidence angles

Livya *et al.*, (2015); published their research paper on Aerodynamic Analysis of Dimple Consequence on Aircraft Wing in International Journal of Mechanical, Aerospace, Industrial, Mechatronics and Manufacturing Engineering. Their venture incorporates both computational and exploratory investigation of dimple impact on airplanes wing, utilizing NACA 0018 airfoil. Dimple states of Semi-circle, hexagon, cylinder, square are chosen for the investigation. Their end results showed the dimple impact by expanding $^{L}/_{D}$ proportion and consequently giving the most extreme streamlined productivity, which gives the upgraded execution for the airplane.

Thamodharan *et al.*, (2016); share their article on Numerical Analysis of Consequence of Dimples on Aero-dynamics of an Airfoil in International Conference on Explorations and Innovations in Engineering & Technology. They increase the stall angle by deferring the stream detachment utilizing dimples at different areas on the suction surface of the airfoil.

Sonia and Manish, (2017) they have published a paper that has raise the following statement as an end result. "Modification of aircraft surface with vortex generator clearly gives more lift but it also increases the drag as induced vortices. It delays stream separation and stalling but also increase fuel consumption. On the other hand dimple gives more lift coefficient and less drag coefficient than vortex generator and results shows clearly that $^{Cl}/_{Cd}$ is much more in situation of dimple. Hence, Overall performance of an aircraft will increase if the airfoil surface is modified by dimple than vortex generator.”

Adding of small dimple along the entire upper surface, stopping at 8% chord length, provided benefits in both kinds of tests, symmetric and cambered. The delay in separation reduces the pressure drag and gives the airfoil less drag and more lift. Such surface modifications applied over to the surface of wing in the form of dimples proves to optimize the value of lift coefficient of the wing by delayed stream separation.

2.3.3 Dimples on HAWT

Arun, *et al.*, (2018) on their work proved this “The predominant factors influencing the efficiency of the wind turbines are lift and drag that are to be maximized and minimized respectively. Surface of turbine blades are included with dimples of various sizes and arrangements and are analyzed using CFD to obtain an optimum combination, through that efficiency of wind turbines can be maximized”. According to their work Nearly1.36MW power was found to be generated and with high levels of accuracy on comparison with actual values, preceded towards the inclusion of dimples; Based on the pressure contour obtained. Dimples are included on the high pressure bottom side of the turbine. Further analysis with dimples have increased the performance to a greater extent, about 1.56 MW power was found to be generated, a 14.5% increase in performance, to be precise. Thus, inclusion of dimples on the surface of wind turbine blades will increase performance levels.

These literature reviews could be summarized as follow. Numerous studies shows that Ethiopia possess a tremendous amount of wind energy potential (especially eastern part of the country). In order to harness this energy potential proper design of wind turbine blade is a necessity, among different methods of designing HAWT blade BEM is the most widely and preferred method in previous works. The literature review have also showed that Dimple on the surface of aircraft wing have also exhibit enhancing lift force by delaying flow separation.

In this thesis based on the reviewed literature’s method and research gap found the aerodynamic effect of surface dimple is examined and in addition to that wind energy potential prediction of a selected site area coupled with HAWT blade design using BEM is done.

CHAPTER THREE

WIND ENERGY POTENTIAL AND BLADE DESIGN ANALYSIS

3.1 WIND POTENTIAL OF THE SITE

Selecting an apt site is vital to the success of any renewable-energy project, monetarily and technically. This pertain to each kind of project, from the least residential systems to the largest utility-scale projects. It also pertain to every renewable-energy technology, from wind to solar to biomass, and further. Selecting the proper site and designing a turbine array to fit it are vital to ensuring that wind farms perform as expected.

The eastern part of Ethiopia, down through the Great Rift Valley have noticeable amount wind energy potential. The intended site is located, in the Oromia regional state, East Hararge zone at latitudinal and longitudinal coordinates of 9.2228 ^{0} and 41.79^{0} respectively. The local name of the area is “WETER” and is free from any kind of human settlement and vegetation.

Figure 3.1: Geographical Location of the Site (Google Map, 2019)

Figure 3.2 : Satellite View of the Site (Google Map, 2019)

Utilizing the available long term wind data from the meteorological stations near to the candidate site is applicable for making pilot estimates. These meteorological data, that may be accessible for long periods, will be extrapolated to estimate the wind profile of the site. Contemporary wind measurement systems grant the mean wind speed at the site averaged over a pre-fixed time duration. Ten minutes average is very common. In this analysis, five year wind (2014-2018 G.C) data from nearby metrological station (Diredawa Metrological Survey Station) and Ten years wind data (2009-2018) from VORTEX-INTERFACE (Vortex Interface, 2019*)* were collected*;* both data sources grant an hourly average wind speed. Concurrent data sets among the two sources are cross checked and illustrate sound similarity.

3.1.1 Mean Wind Speed and Wind Direction

One of the most valuable facts on the available wind spectra of a site is its mean velocity. The mean velocity (V_m) is given by: (Duffie and Beckman, 2013)

$$V_m = \frac{1}{n}\sum_{i=1}^{n} \times V_i \qquad (3.1)$$

Where: Vi = wind velocity (m/s) and n= number of wind data

Conversely, Equation (3.1) is not applicable for wind power calculation. Hence, wind power is proportional to the cube rate of wind speed, on the other hand it can be applicable on power curve for estimating wind power.

The wind direction have a tremendous influence in designing and installing of wind farm. Wind vane is the instrument to measure the wind direction .In this study both the speed and direction of the wind is found from the Diredawa metrological center wind Mast and satellite

3.1.2 Distribution of Wind Velocity

Apart from the mean wind velocity over a period, its distribution is also a critical parameter in wind resource assessment. Wind turbine installed at two distinct sites having the similar mean wind velocity will produce entirely different power output because of differences in the velocity distribution .This shows that, along with the mean wind Apart from the mean wind velocity over a period, its distribution is also a critical parameter in wind resource assessment. In order to address this issue the frequency of distribution should be measured out. Standard deviation (δ_v) shows along with the mean wind measure illustrate variability of wind velocities in a given set of wind data. Standard deviation indicates the deviation of individual velocities from the mean value. It is given by : (Duffie and Beckman, 2013)

$$\delta_v = \sqrt{\frac{\sum_{i=1}^{n}(Vi - Vm)^2}{n}} \qquad (3.2)$$

Lower value of indicate the uniformity of the wind speed data set at the site.

3.1.3 Extrapolation of Wind Speed with Height

The movement of air above the terrain is retarded by frictional resistance offered by the earth surface (boundary layer effect). This resistance caused by the roughness of the ground itself or due to vegetation, buildings and other structures present over the ground will have a significance impact to be considered in the design of wind energy plants. The rate of wind speed increase with height depends on site terrain type. It is usually represented by roughness class or roughness length and wind shear exponent of the site. Therefore, care has to be taken to determine the appropriate surface roughness length and wind shear exponent of the site before extrapolating the wind speed to the necessitated height.

The log law equation that incorporates the surface roughness length in the extrapolation of wind speed to the hub height and is given by: (Duffie and Beckman, 2013)

$$V = V_{ref} \times \frac{\ln(\frac{z}{z_o})}{\ln(\frac{z_{ref}}{z_o})} \qquad \text{……………………………………………….……………… (3.3)}$$

Where: V= Wind velocity at height z above ground level, (m/sec).

V_{ref} = Refrence velocity, i.e. a wind velocity at heightz_{ref}.

z = Height above ground for the desired velocity.

z_o= Surfase roughness length of the site.

z_{ref}= Reference height, i.e, the height where the exact wind velocity V_{ref} is known

3.1.4 Estimation of Wind Energy

Wind energy density and the energy available in the region over a period are usually taken as the index for evaluating the energy potential at the site than wind speed alone. The wind energy density (ED) is the energy available in the region for a unit rotor area and time.

Weibull based approach: - For a unit swept area of the rotor, power available (PV) in the wind stream of velocity V_I is: (Duffie and Beckman, 2013)

$$P_V = \frac{1}{2} \rho \sum_{i=1}^{n} V_i^3 \qquad \text{…….……..…………..…………………… (3.4)}$$

Where: ρ is the air density, $^{kg}/_{m^3}$ and V_I =Wind velocity, m/s

The portion of time for which this velocity V_I prevails at the site is given by the probability density function f (V). The energy per unit time contributed by V_I is PV x f (V). Thus the total energy ED, contributed by all possible velocities at the wind site, available for unit swept rotor area and time is expressed as:

$$E_D = \int_0^\infty P_V \, f(V) dV \qquad \text{……………………..…….…………………………… (3.5)}$$

Substituting for PV and f (V) in the above expression and with the standard gamma integral, it gives:

$$E_D = \frac{\rho A^3}{2} (\frac{3}{K}) \Gamma(\frac{3}{K}) \qquad \text{……………………….……..…………………………… (3.6)}$$

Once ED is known, energy available over a period EI can be calculated as

$$E_I = TE_D = \frac{\rho A^3 \, T}{2} (\frac{3}{K}) \Gamma(\frac{3}{K}) \qquad \text{…………………..…………………………………… (3.7)}$$

Where: T is the time period.

The most frequent wind velocity, f' (V) = 0, that is denoted by V_F max. Thus

$$V_{F\ Max} = A\left(\frac{K-1}{K}\right)^{\frac{1}{K}} \qquad \text{…….. (3.8)}$$

The velocity contributing maximum energy to the regime ($V_{F\ Max}$) is given by:

$$V_{F\ Max} = A\left(\frac{K+2}{K}\right)^{\frac{1}{K}} \qquad \text{…… (3.9)}$$

3.2. BLADE DESIGN ANALYSIS

The aerodynamic design of a wind turbine rotor includes the choice of the number of blades, determination of blade length, type of airfoil section, blade chord and twist distributions and the design tip-speed ratio (TSR=rotational speed x rotor radius/design wind speed at hub height). Concerning blade number (NB), a rotor with one blade can be cheaper and easier to erect but it is not popular and too noisy. The two-bladed rotor is also simpler to assemble and erect but produces less power than that developed by the three-bladed one. The latter produces smoother power output with balanced gyroscopic loads, and is more aesthetic. The determination of the blade length (or rotor size) depends mainly on the needed energy for certain application and average wind speed of a specific site. The choice of the kind of airfoil section may be regarded as a key point in designing an efficient wind rotor (Burger and Hartfield, 2006).

In this research, Blade momentum theory (BEM) is used to design a HAWT blade based up on the wind data analysis, the energy density of the site is found to be 610 w/m^2. BEM is employed for obtaining maximum lift to drag ratio for each elemental constitution of the blade. Obtaining chord and twist distribution at selected tip speed ratio of the blade, the aerodynamic shape of the blade in every part is specified with correspond to maximum accessible power coefficient. The design parameters are power coefficient, angle of attack, drag and lift coefficients.

3.2.1 Airfoil Selection

To design a wind turbine proper selection of airfoil is needed so four different types of wind turbine airfoils are selected and compare corresponding aerodynamic performance using site condition as an input. S830, S827, SG6041 and SG6050 HAWT airfoils were the nominated airfoils for the site.

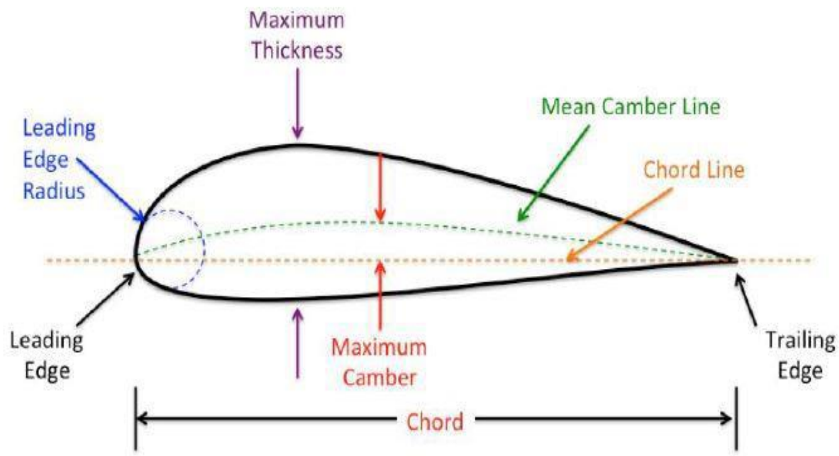

Figure 3.3 :- Airfoil Terminology (Burger and Hartfield, 2006).

For wind turbine blade design and analysis, it is essential to have the aerodynamic data of the selected airfoil at the corresponding flow conditions, i.e. Reynolds (Re) numbers. The Reynolds number is defined as

$$R_e = \frac{U_{rel}\, C}{\upsilon} \qquad \text{.......... (3.10)}$$

Where: U_{rel} is the relative wind speed (m/s).

C is chord length (m).

υ is kinematic viscosity of air ($\nu = 14 \times 10^{-6}$ m^2/s)

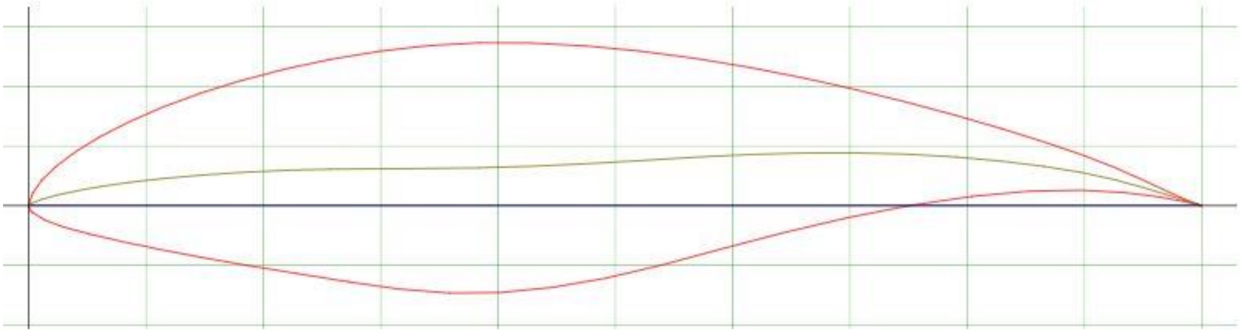

Figure 3.4 : S830 Wind Turbine Airfoil (Aerofoiltools.com, 2019)

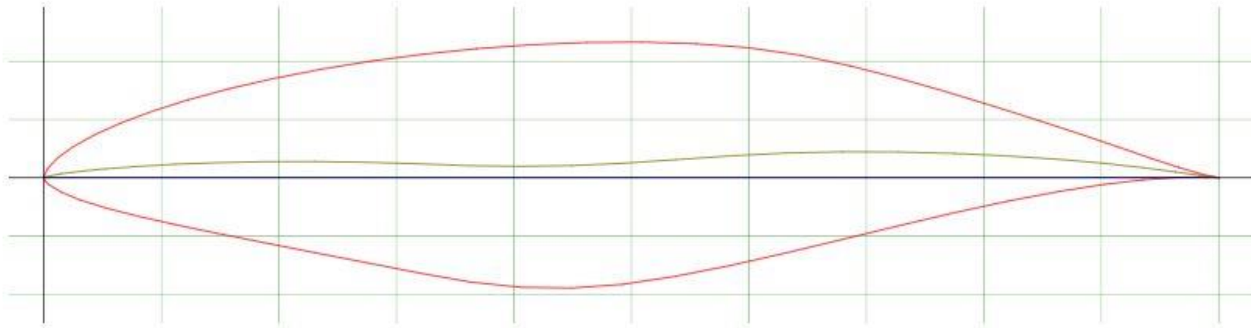

Figure 3.5 : S827 Wind Turbine Airfoil (Aerofoiltools.Com, 2019)

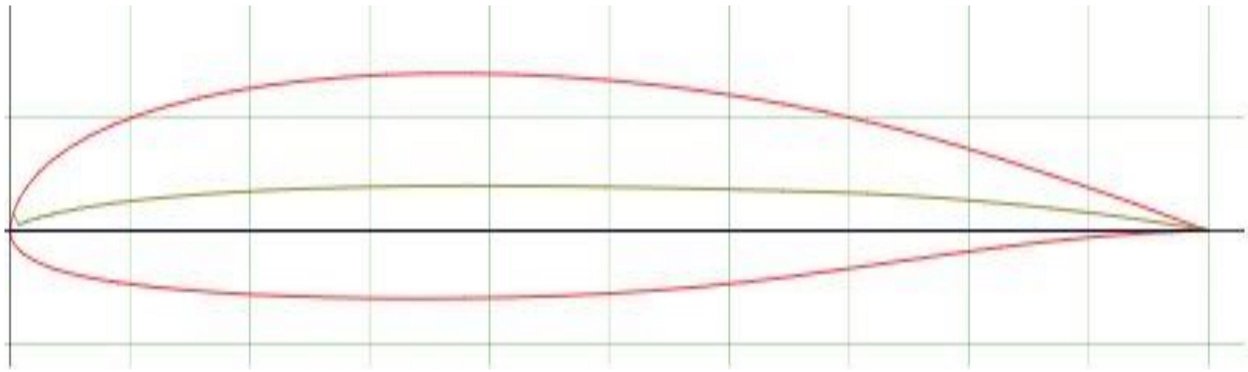

Figure 3.6 : Sg6041 Wind turbine airfoil (Aerofoiltools.com, 2019)

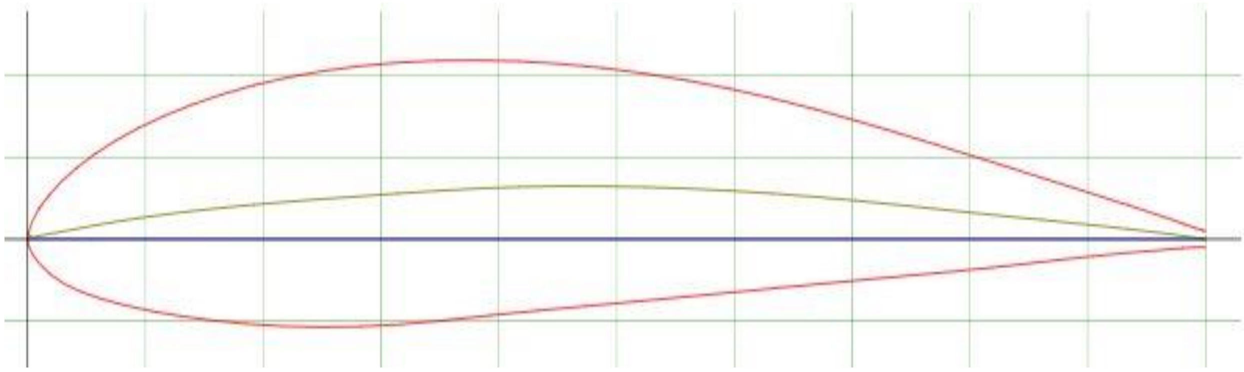

Figure 3.7 . Sg6050 Wind Turbine Airfoil (Aerofoiltools.Com, 2019)

The above listed airfoils have a distinct aerodynamic character; for the selected site based on the Reynold number the aerodynamic characteristics of these airfoils were compared.(Appendix, A-1) The comparison shows that S830 have a better performance. Therefore s830 is selected for further blade design analysis and studies.

3.2.2 Chord Distribution and Angle of Twist

Tip Speed Ratio: - The tip speed ratio defined as the relationship between rotor blade velocity and relative wind velocity Equation 3.11 is the foremost design parameter around that all other optimum rotor dimensions are calculated: (Hansen et.al, 1993*)*

$$\lambda = \frac{\Omega_r}{V_w} \quad \ldots\ldots (3.11)$$

Where: λ= Tip speed ratio Ω_r= Rotational velocity (rad/s), r = radius, V_w = Wind speed.

Features such as efficiency, torque, mechanical stress, aerodynamics and noise should be considered in selecting the appropriate tip speed as depicted in Table 3.1. The efficiency of a turbine can be increased with higher tip speeds, even though the increase is not significant when considering some drawbacks such as increased noise, aerodynamic and centrifugal stress.

Table 1: Tip Speed Ratio Design Consideration (Peter J. Schubel et.al, 2012)

Tip speed ratio	⇦ Low	High ⇨
Value	Tip speed of one to two are considered low	Tip speeds higher than 10 are considered high
Utilization	Traditional wind mill and water pump	Mainly single blade or two blade prototype
Torque	Increase	Decrease
Efficiency	Decrease significantly below five due to rotational wake created by high torque	Insignificant increase after eight
Centrifugal stress	Decrease	Increase as a square of rotational speed
Aerodynamic stress	Decrease	Increase proportional with rotational speed
Area of solidity	Increase, multiple 20^+ required	Decrease significantly
Blade profile	Large	Significantly narrow
Aerodynamics	Simple	Critical
Noise	Increase to the six power approximately	

A higher tip speed demands lessen chord widths leading to narrow blade profiles. This can steer to reduce material usage and lower production costs. Even if an increase in centrifugal and aerodynamic forces is linked with higher tip speeds. The increased forces imply that difficulties exist with maintaining structural integrity and avoid blade failure. As the tip speed increases the aerodynamics of the blade design become increasingly critical. A blade which is designed for great relative wind speeds develops minimal torque at lower speeds. This results in a higher cut in speed and difficulty self-starting. A noise increase is also associated with increasing tip speeds as noise increases approximately proportionately to the sixth power. Modern HAWT generally utilize a tip speed ratio of nine to ten for two bladed rotors and six to nine for three blades. This has been found to produce efficient conversion of the winds kinetic energy into electrical power (Peter, et al., 2012).

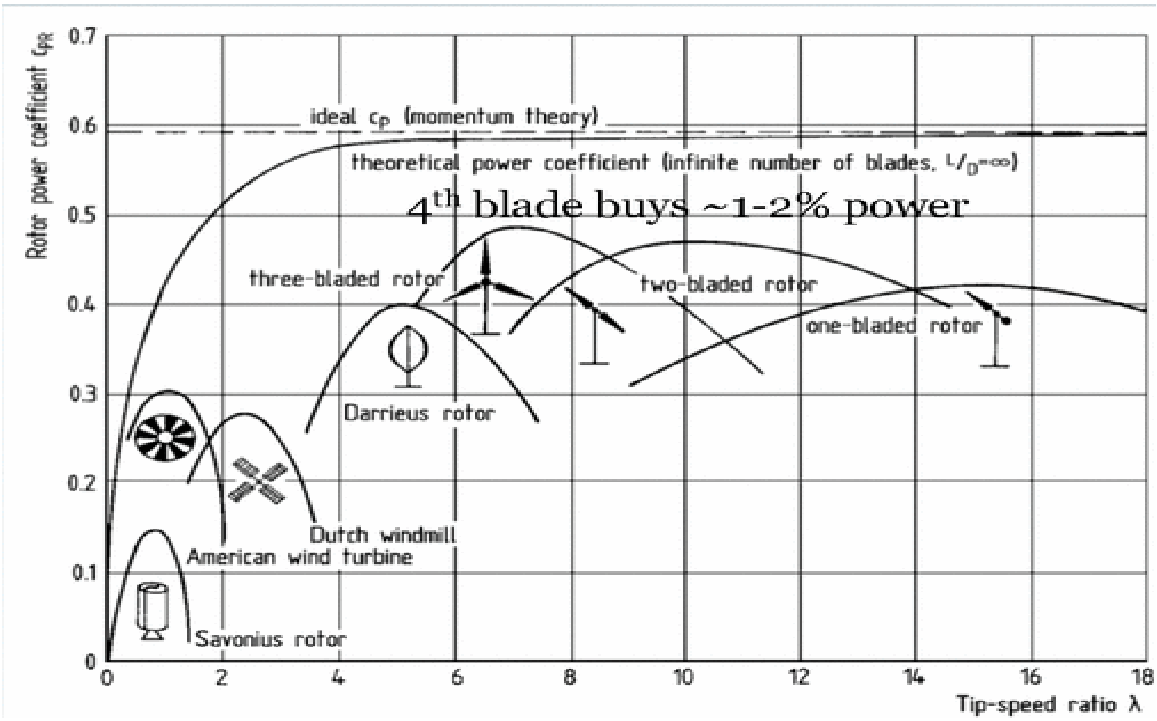

Figure 3.8: Dependence of Power Coefficient in Tip-Speed Ratio for Distinctive Wind Turbines (Hansen *et al*., 1993)

Blade Plan Shape and Quantity: - The ideal plan form of a HAWT rotor blade is defined using the BEM method by calculating the chord length according to Betz limit, local air velocities and airfoil lift. Several theories exist for calculating the optimum chord length that range in complexity (Hansen et al., 1993), with the simplest theory based on the Betz optimization (Equation 3.12). For blades with tip speed ratios of six to nine utilizing airfoil sections with negligible drag and tip losses, Betz's momentum theory gives a good approximation. (Peter et al., 2012).

In instances of low tip speeds, high drag airfoil sections and blade sections around the hub, this method could be considered inaccurate. In such situations, wake and drag losses should be accounted (Hansen et.al, 1993*)*. The Betz method gives the basic shape of the modern wind turbine blade (Figure 3.9). (Hansen et.al, 1993*)*

$$C_{opt}=\frac{2\pi r}{n}\frac{8}{9C_L}\frac{U_{wd}}{\lambda V_r} \quad \ldots\ldots (3.12)$$

Where, $V_r = \sqrt{{V_w}^2 + U^2}$

r = radius (m), n = Blade quantity,

C_L = Lift coefficient, λ = Local tip speed ratio,

V_r = Local resultant air velocity (m/s), U= Wind speed (m/s),

U_{wd} = Design wind speed (m/s), C_{opt} = Optimum Chord length

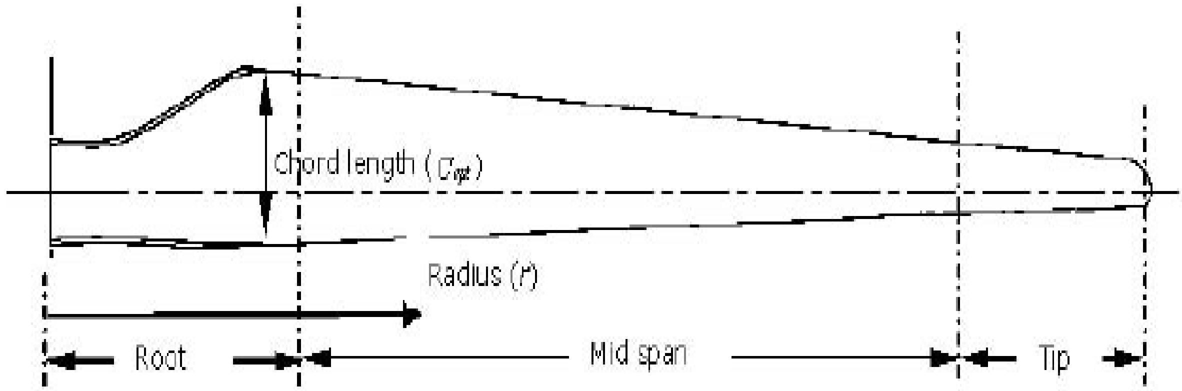

Figure 3.9 : Nomenclature of wind turbine blade

Low tip speed ratios produce a rotor with a high ratio of solidity, which is the ratio of blade area to the area of the swept rotor. It is useful to reduce the area of solidity as it leads to a decrease in material usage and therefore production costs. Conversely, problems are associated with high tip speeds.

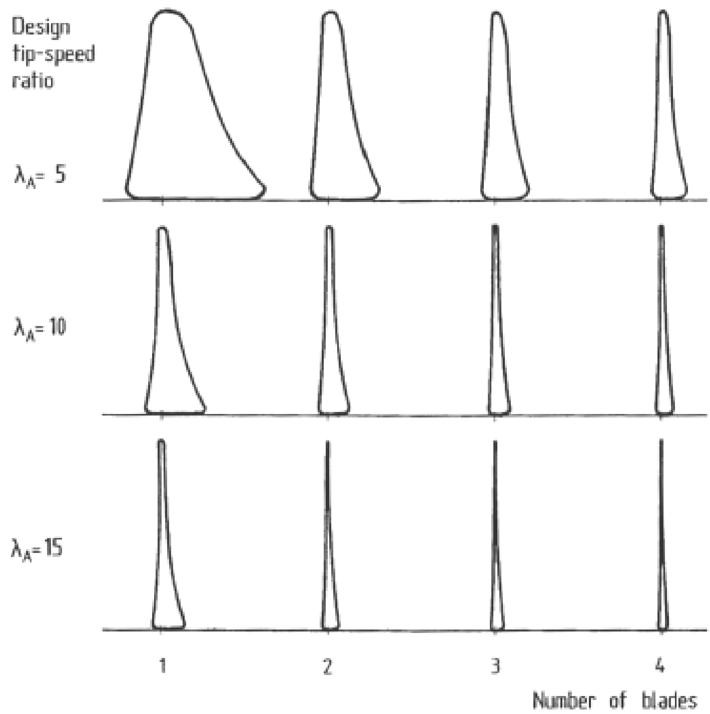

Figure 3.10 : Optimal Blade Plan Shape for Alternate Design Tip-Speed Ratios and Number of Blade

Assuming that a reasonable lift coefficient is maintained, utilizing a blade optimization method produces blade plans principally dependent on design tip speed ratio and number of blade. For this thesis based up on the wind potential it's feasible to employ 25 m span blade and TSR value of 6.75.

Turbines are designed to operate within a specific range of wind speeds. Based on the selected site cut in wind speed 3 m/s, cut off wind speed 22 m/s and rated wind speed 10m/s are selected .Tangential speed of blade vary across the span of blade amount lift vary across the blade span. In order to have a uniform lift coefficient the chord distribution of the blade vary from the root to tip. By using BEM method the chord distribution result along the span is plotted on Figure 3.11.

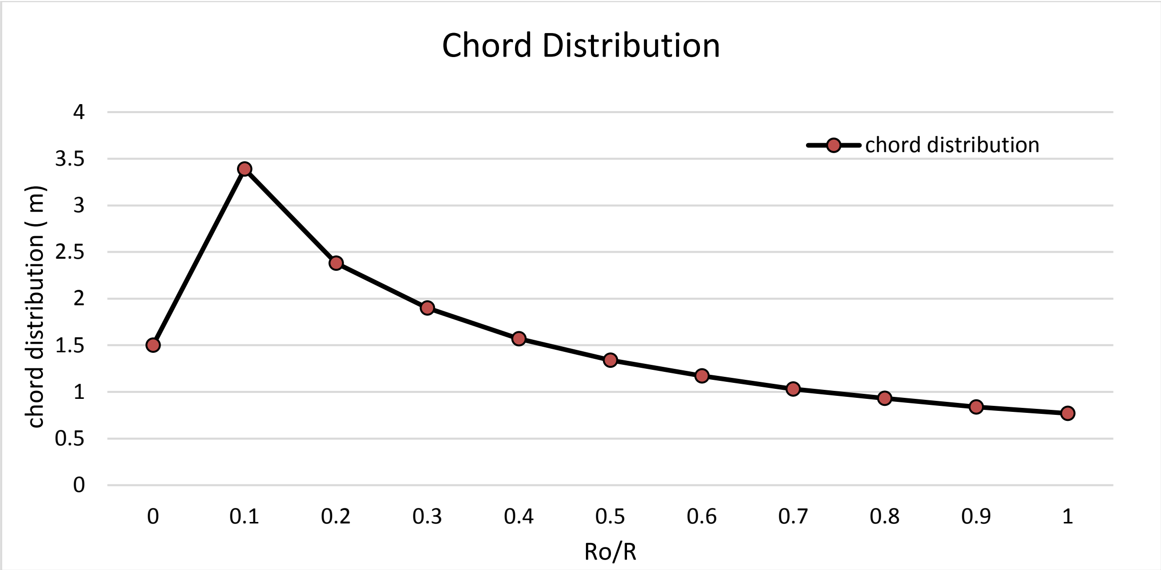

Figure 3.11 : Chord Distribution versus Span Length Ratio

Angle of Twist

The lift generated by an airfoil section is a function of the angle of attack to the inflowing air stream. The inflow angle of the air stream is dependent on the rotational speed and wind speed velocity at a specified radius. The angle of twist necessitated is reliant upon tip speed ratio and desired airfoil angle of attack. Generally the airfoil section at the hub is angled into the wind due to the high ratio of wind speed to blade radial velocity. In contrast the blade tip is likely to be almost normal to the wind.

BEM method employs Equation 3.13 to calculate blade twist angle. (Hansen et.al, 1993)

$$\varphi = \left(\frac{2}{3}\right)\tan^{-1}\left(\frac{1}{\lambda_r}\right) \quad \text{…………………………………………………………….. (3.13)}$$

Where, λ_r is the local speed ratio, φ is the blade twist angle.

The justification for the twist is to produce uniform lift from the hub to the tip. As the blade rotates, there is a difference in the actual speed of the various portions of the blade. The tip of the blade travels faster than the part near the hub, because the tip travels a greater distance than the hub in similar length of time. Figure 3.12 depict end result of the angle of twist based on the above mathematical correlation employed.

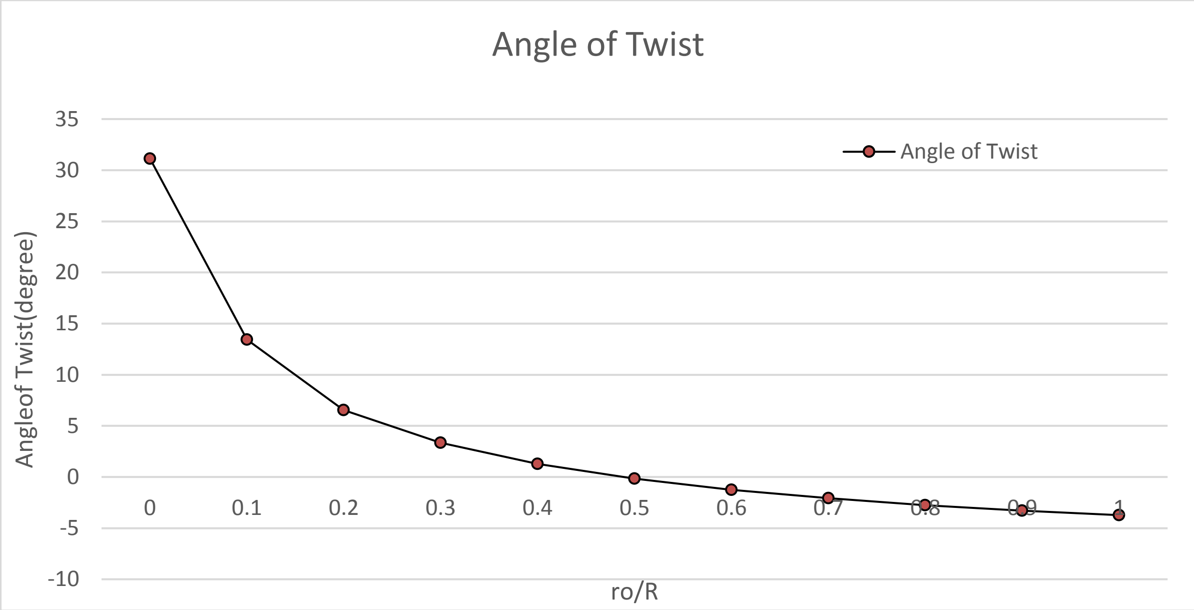

Figure 3.12 : Angle of Twist versus Span Ratio

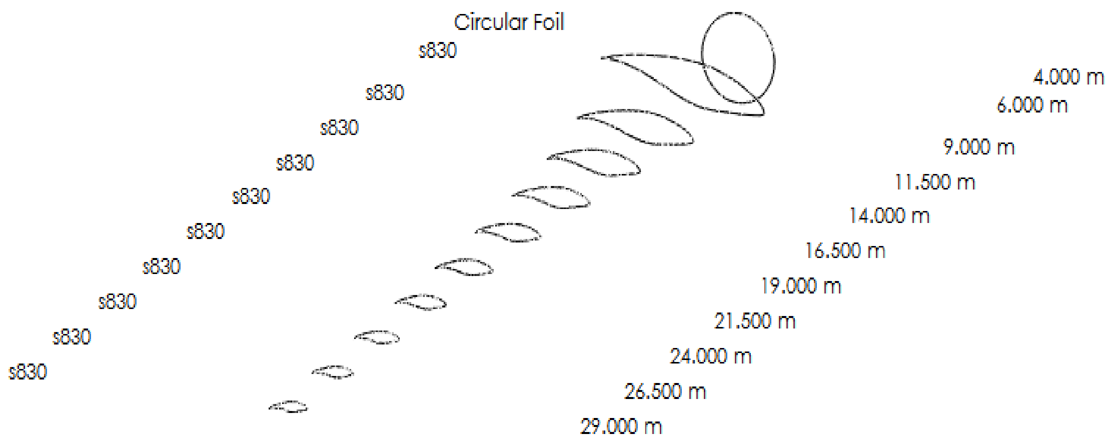

Figure 3.13 : Chord Distribution and Angle of Twist of Foils

Analytical result of BEM model gives an output of maximum chord length 3.4 m at span radius of 5 m and minimum chord length of 0.77 m at span radius of 25 m. The following figure shows schematic and surface drawing of the chord distribution and angle of Twist of the designed blade using S830 airfoil.

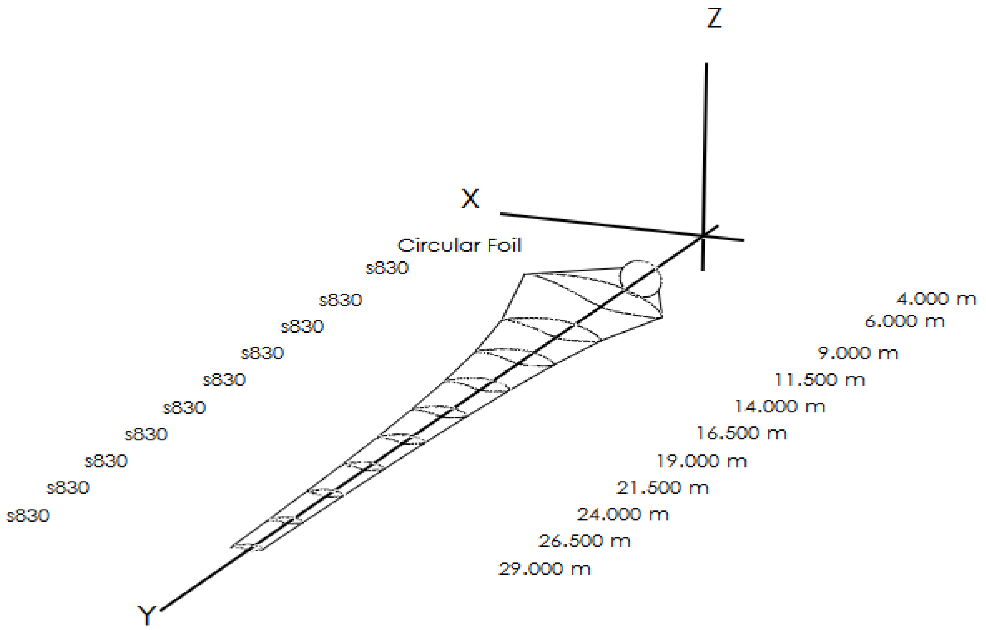

Figure 3.14 : Schematic Drawing of Designed Blade

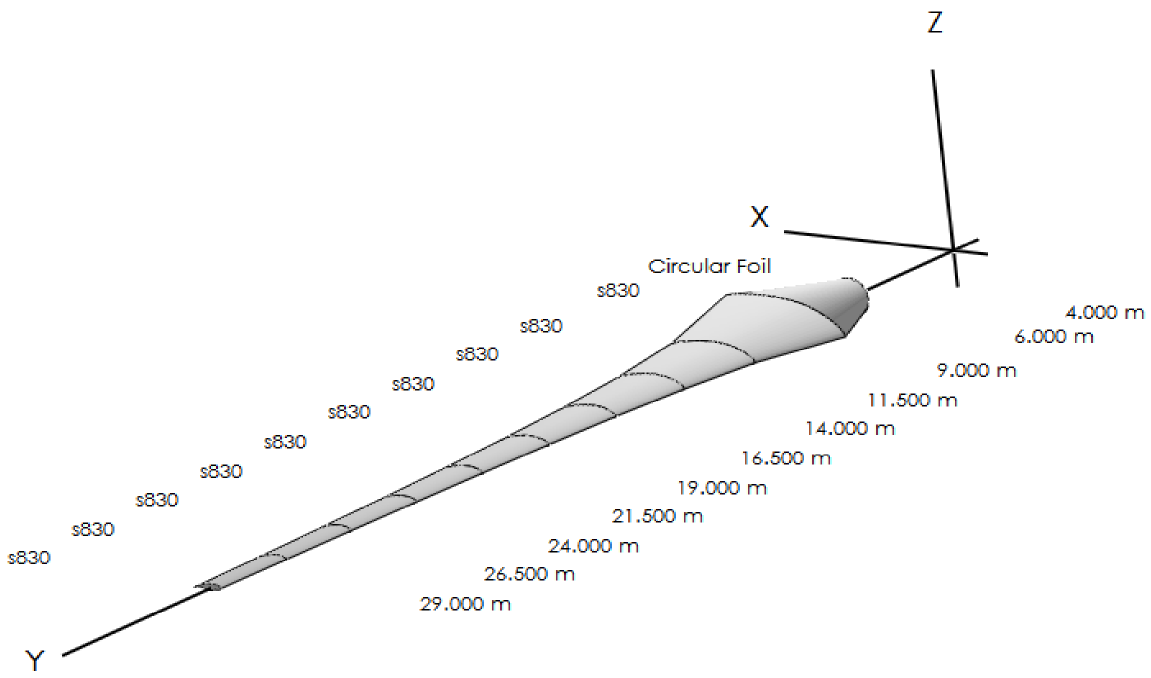

Figure 3.15 . Designed wind Turbine Blade

As it's expressed in previous sections wind turbine blade have three sections; namely root, mid-section and tip. Average angle of twist result corresponding to these section are 25^{o},-1^{o} and -3.73^{o} respectively. The total swept area of designed turbine is 1962.5 m^2.

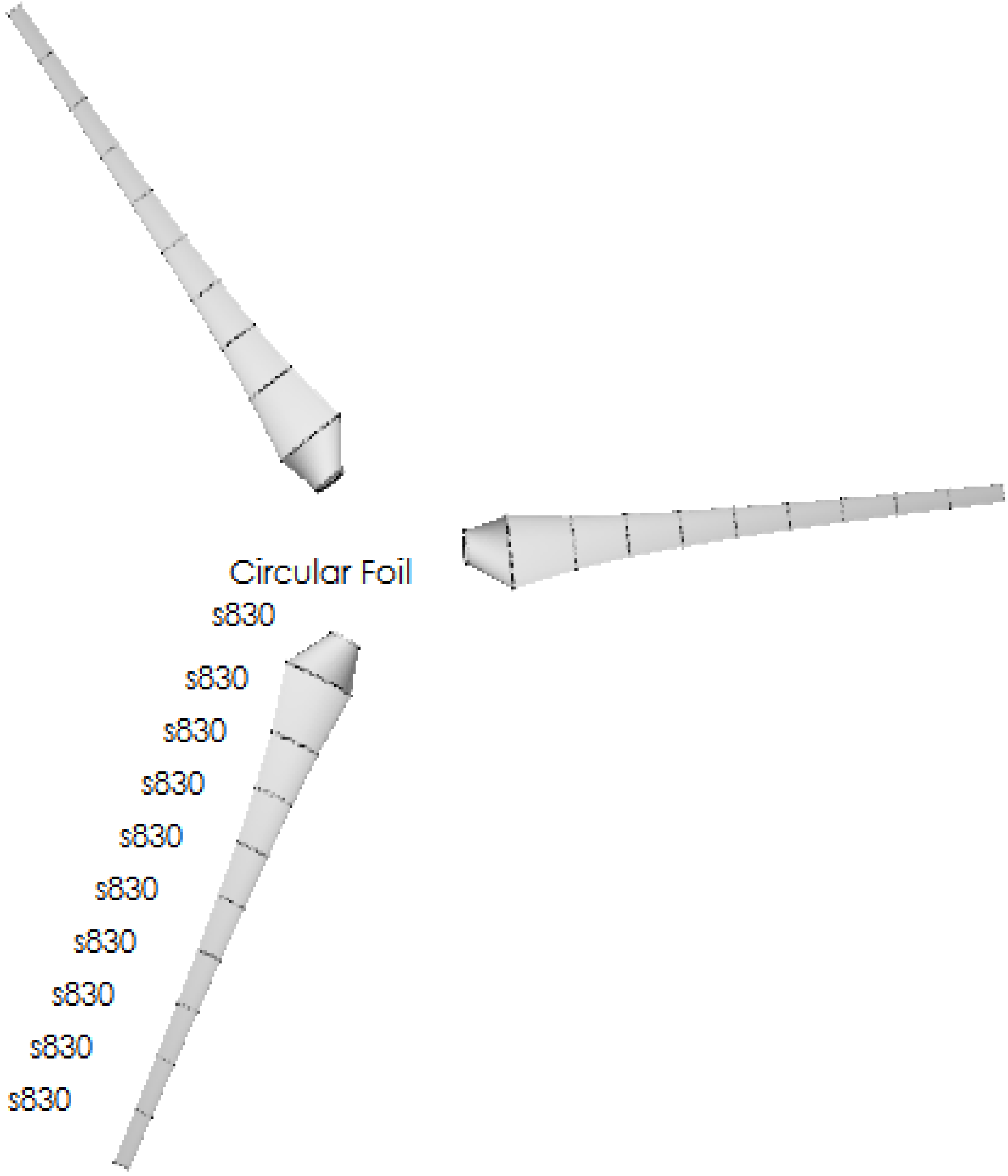

Figure 3.16 : Designed Wind Turbine

3.2.3 Aerodynamic Characteristics of the Blade

Aerodynamic performance is basic for efficient rotor design (Hansen et.al 1993). Aerodynamic lift is the force reliable for the power yield generated by the turbine and it is therefore essential to capitalize this force using appropriate design. A resistant drag force that counter the motion of the blade is also generated by friction which must be lessen. It is then vivid that an airfoil section with a high lift to drag ratio (Equation 3.14), typically greater than 3, be chosen for rotor blade design (Hansen et al., 1993):

$$Lift\ to\ Drag\ Ratio = \frac{Coefficient\ of\ lift}{Coefficient\ of\ drag} = \frac{C_L}{C_D} \qquad \text{.......} \quad (3.14)$$

According to Çetin, the power coefficient is a function of TSR, blade number and maximum lift/drag ratio (Peter et al., 2012)

$$C_p = (1 - \frac{\lambda}{Cl/_{Cd}}) \times (1 - \frac{1.84}{Z.\lambda}) \quad \text{……………………………………………… (3.15)}$$

Where Z is the blade number, which is 3, $\frac{C_L}{C_D}$ is the maximum lift to drag ratio

$C_{p\ Schmitz}$ is the Schmitz power coefficient, which is 0.5926.

An aerodynamic phenomenon known as stall should be considered carefully in turbine blade design. Stall typically occurs at large angles of attack depending on the airfoil design. The boundary layer separates at the tip rather than further down the airfoil causing a wake to flow over the upper surface drastically reducing lift and increasing drag forces. This condition is considered dangerous in aviation and is generally avoided. For pitch controlled wind turbines stall is still considered as halt so in this design the operating angle of attack of the blade is selected free from stall, meanwhile for stall-regulated wind turbines stall can be utilized to limit the maximum power output to prevent generator overload and excessive forces in the blades during extreme wind speeds and could also occur unintentionally during gusts (Hansen *et.al.,* 1993). It is therefore desirable that the onset of the stall condition is not instantaneous for wind turbine airfoil as this would create excessive dynamic forces and vibrations.

CHAPTER FOUR

NUMERICAL AERODYNAMIC PERFORMANCE ANALYSIS

4.1 Introduction

The computational fluid dynamics (CFD) approach has been employed to model and study the aerodynamic behavior of wind turbines, the detailed flow field characteristics around a rotating wind turbine rotor/blade as well as the power performance can be attained by the CFD approach. With the increasing computing capacity, the CFD approach is becoming a practical apparatus to model and simulate wind turbine aerodynamic performance in three dimensional spaces and instantaneous time domain the main interest of solving CFD problems are turbulence models and mesh topology.

Computational Fluid Dynamics (CFD) is an extension of fluid mechanics; it describes fluid motion through the use of numerical techniques using a computer. It is concerned with the solution of the velocity field and hence, the pressure field for given fluid properties (e.g. density, viscosity and surface tension). The two key obstacles in fluid mechanics to a workable theory are viscosity and geometry. In a small number of idealized situations viscosity can be neglected, rendering the stream fields inviscid. Conversely, for the vast majority of situations viscosity is present and may even vary, that increases the difficulty of constructing and using the basic equations (White, 2008). Moreover, it can have a destabilizing effect on the aforementioned stream field creating a disorderly, random phenomenon known as turbulence.

Complex geometry featuring rapid changes in the geometrical bounds of the fluid, make it difficult to find so-named ‘closed-formed analytical solutions’ of problems. It is possible to solve problems featuring complex geometry and viscosity using numerical techniques on a computer that is commonly known as Computational Fluid Dynamics (CFD).

CFD implements conservation principles, including the three fundamental conservation equations of

- Mass (continuity)
- Momentum (Newton’s second law)
- Energy (first law of thermodynamics)

By applying conservation principles to fluid motion it is possible to define the Navier-Stokes (N-S) Equations, which can be given in different forms. Equation 4.1 and 4.2 gives them in incompressible vector form. These equations describe the motion of any Newtonian fluid.

$$\nabla\vec{V} = 0 \quad (4.1)$$

$$\rho\left(\frac{\partial\vec{V}}{\partial t} + \vec{V}.\nabla\vec{V}\right) = -\nabla p + \mu\nabla^2\vec{V} + \vec{S} \quad (4.2)$$

Where $\vec{V}$ is the velocity vector, t is time, ρ is density, p is pressure, μ is the viscosity, $\vec{S}$ is a source term and ∇^2 is the Laplacian operator

Incompressibility is assumed for flows when the local Mach number (the ratio of the speed of an object to the speed of sound of the fluid) is below 0.3. For wind turbines the flow has velocities normally around 5−25m/s, resulting in a Mach number of less than 0.1, therefore the incompressible assumption is completely justifiable. (Snel, 2003).The mean wind speed of the site 10 m/s therefore the stream is assumed incompressible.

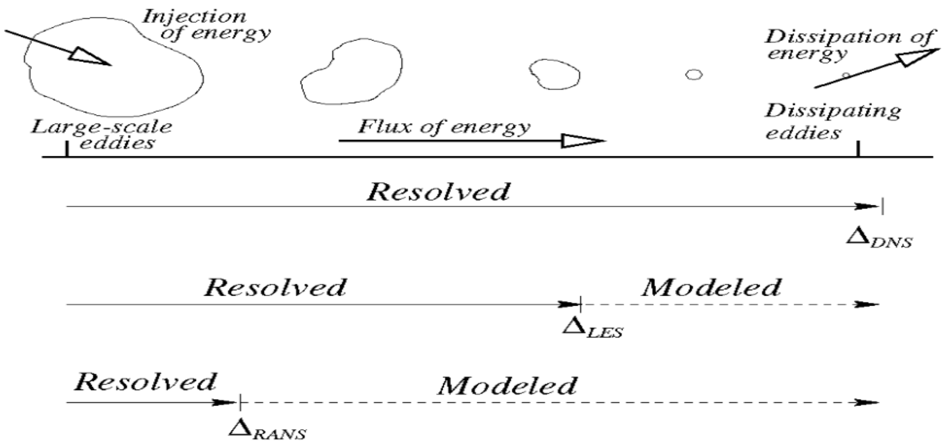

Figure 4.1 Illustration of the Resolved and Modelled Parts of the Flow (White, 2009)

Even if the incompressible Navier-Stokes equations implicitly describe turbulent flow fields they are inherently difficult to solve due to the non-linear nature, specifically the convective acceleration term .Due to this there are a number of different CFD methodologies, each of that numerically resolve the Navier-Stokes equations and model the resulting flows to varying degrees as shown in Figure 4.1. Four such methods are the Reynolds-Averaged Navier-Stokes (RANS), Large Eddy Simulation (LES), Detached Eddy Simulation (DES) and Direct Numerical Simulation (DNS) There is much research reported in the literature as well as a number of textbooks with greater detail regarding these methods. (Bechmann, 2006). The difference between these models is their consideration of turbulence modelling.

Turbulence is characterized by random velocity variations within the stream that are generally modelled using statistical methods, based on experimental work (Wilcox, 2006). If a fluid is not turbulent then it is said to be laminar, and is normally characterized by steady parallel fluid layers with no mixing. The problem with solving turbulent fluid problems is that turbulence is inherently three-dimensional, and operates at a smaller length scale than laminar (non-turbulent) flows. The Atmospheric Boundary Layer (ABL) can have a length scale ranging from approximately 1 km to as small as 1 mm (Stull, 1988) and blade boundary layers can have even smaller scales. This creates a problem in trying to resolve all the length scales. Conversely, it is sometimes feasible and is named Direct Numerical Simulation (DNS) that is extremely computationally expensive and is not always viable. To overcome this a large number of turbulence models have been constructed for these small length scales, allowing the large scales to be resolved.

Reynolds number; Re, is a dimensionless number (has no units) that is used in fluid mechanics to describe flow. In 1883 Osborne Reynolds (*Reynolds, 1883*) showed that the transition from laminar to turbulent flow occurs at a critical value. The Reynolds number is commonly calculated using Equations 4.3 and 4.4, referred to as the ratio of inertia force to viscous force; Laminar flows feature low Reynolds numbers. The higher the Reynolds number the more likely a flow is to be turbulent; and the finer the small length scales (mixing) within the flow.

$$Re = \frac{Inertia\ force}{Viscous\ force} \qquad \text{(4.3)}$$

$$Re = \frac{\rho u l}{\mu} \qquad Re = \frac{ul}{cv} \qquad \text{(4.4)}$$

Where ρ is the density, u is the speed, l is a characteristic length, μ is the dynamic viscosity and ν the kinematic viscosity.

4.1.1 Reynolds-Averaged Navier-Stokes

The Reynolds-Averaged Navier-Stokes (RANS) method is the fastest CFD approach. It was first described in 1895 by Osborne Reynolds (Reynolds, 1895). It employs time averaged motion, which introduces a new quantity known as the Reynolds stress. RANS models compute this variable either through the use of an eddy-viscosity model or Reynolds Stress model.

The eddy-viscosity models vary with complexity and approximate the Reynolds stresses using the Boussinesq hypothesis also named the Boussinesq approximation and Boussinesq eddy-viscosity assumption. The Boussinesq hypothesis, proposed by Boussinesq, is a linear relation, shown in Equation 4.5, between the stress tensor τ_{ij} and mean strain tensor (S) and is analogous to the linear relation between the viscous stress tensor and viscosity. It relates the Reynolds stresses to the velocity gradients through an eddy-viscosity, in an analogy to molecular viscosity, assuming that the Reynolds stress tensor is coincident with the mean rate tensor. In particular, Schmitt analyzed the validity of the hypothesis using databases as well as DNS and LES test situations and found that it is almost never verified. Despite this the eddy-viscosity is widely employed to model turbulence and can perform well when used correctly.

$$\tau_{ij} = -\mu_T S \qquad \text{(4.5)}$$

$$S = \frac{1}{2}\left(\frac{\partial \bar{u}_j}{\partial x_i} + \frac{\partial \bar{u}_i}{\partial x_j}\right) \qquad \text{(4.6)}$$

Where τ_{ij} is the stress tensor and S is the mean strain tensor, μ_T is the eddy-viscosity u is the mean velocity component, xi, j is the Cartesian coordinate system and i, j represent components in the i, jth direction

The eddy-viscosity models vary with complexity, ranging from algebraic models to two equation models. The most commonly employed in wind turbine applications are the two equation models k- ε (Jones, 1972**),** k-ω (Wilcox, 2006) and k-w SST (Menter, 1993), where k is the turbulence kinetic energy per unit mass (or specific turbulence kinetic energy), ε is the specific dissipation and ω is the specific dissipation rate.

There are numerous models that employ the eddy-viscosity concept to different degrees. These models are divided into algebraic models, one equation models and two equations models.

a) Algebraic Models

Algebraic or zero equation turbulence models are computationally the simplest models and often compute the eddy-viscosity in terms of the mixing length. The mixing length hypothesis was proposed by Prandtl in 1925 (Bechmann, 2006).

The hypothesis leads to defining the eddy-viscosity as:

$$\mu_T = \rho l^2{}_{mix} \left|\frac{d\bar{u}}{dy}\right| \quad (4.7)$$

Where μT is the eddy-viscosity, ρ is density and l mix is the mixing length. The mixing length is empirical, depending on the flow and must be specified in advance. Therefore, by definition the algebraic models are incomplete turbulence models.

b) One Equation Models

One equation models calculate one turbulent transport equation, usually the turbulence kinetic energy. It is technically the specific turbulent kinetic energy as it is per unit mass, shown in Equation 4.9, Even if it is commonly just named the turbulence kinetic energy. One equation models are incomplete as they normally relate the turbulence length scale to some stream parameter. The original one equation model was developed by Prandtl in 1945. *(Bechmann, 2006)* Prandtl calculated the specific turbulent kinetic energy as shown in Equation 4.9 and assumed that the turbulent dissipation (e) was proportional to $\rho k^{1/2} l$. The turbulence length scale still needs to be defined in advance to close the system.

$$k = \frac{1}{2}\left(\overline{u'^2} + \overline{v'^2} + \overline{w'^2}\right) \quad (4.8)$$

$$\rho\frac{\partial k}{\partial t} + \rho\bar{u}_j\frac{\partial k}{\partial x_j} = \tau_{ij}\frac{\partial \bar{u}_i}{\partial x_j} - C\rho\frac{k^{3/2}}{l} + \frac{\partial}{\partial x_j}\left[\left(\mu + \frac{\mu_T}{\sigma_k}\right)\frac{\partial k}{\partial x_j}\right] \quad (4.9)$$

$$\mu_T = \rho k^{1/2} l \quad (4.10)$$

Where k is the specific turbulence kinetic energy, xi, j is the Cartesian coordinate system, $\overline{u'^0}$ is the mean velocity component, t is time, ρ is density, μ is the viscosity, μ_T is the eddy-viscosity, C are closure coefficients, i, j represent components in the i, jth direction and l is the turbulence length scale. Since Prandtl's one equation model there have been many more models developed, more elaborate than his. Prandtl's model only necessitates two closure coefficients (C,sk) whereas other have many more such as Baldwin-Barth model that has seven closure coefficients and two damping functions and the Spalart-Allmaras model that features eight closure coefficients and three damping functions.

c) Two Equation Models

Two equation models are complete, providing a closed system and are the simplest complete system employed in CFD modelling. They calculate two equations: one for the specific turbulence kinetic energy and the other is related to the turbulence length scale. There are many different models, the main difference being the second equation and the variable calculated, including the turbulence length scale (l), specific dissipation (ε) or specific dissipation rate (ω) .The first two equation model was developed by Kolmogorov in 1942 that was a k-ω model. (Bechmann, 2006). All two equation models feature closure coefficients that have been employed to replace double and triple correlation terms with algebraic expression involving known properties. If turbulence theory was exact these coefficients would be set from first principles but it is not and the models are developed based on dimensional analysis and observations. There are many models but the main models employed today are the k-ε, k-ω and k-ω SST models that are discussed in more detail.

I. k-ε Model

The k-ε model is the most popular model and in many situations the default model. It features equations of the specific turbulence kinetic energy (k) and the dissipation per unit mass (e) often just referred to as the dissipation. It was first developed by Jones &Launder and later improved by Launder and Sharma. The model is so widely employed it is normally referred to as the standard k-ε model or just the k-ε model without any references. The model defines k using Equation 4.8 and $\boldsymbol{\varepsilon}$ using Equation 4.11.

$$\rho\frac{\partial k}{\partial t} + \rho\bar{u}_j\frac{\partial k}{\partial x_j} = \tau_{ij}\frac{\partial \bar{u}_i}{\partial x_j} - \rho\varepsilon + \frac{\partial}{\partial x_j}\left[\left(\mu + \frac{\mu_T}{\sigma_1^\varepsilon}\right)\frac{\partial k}{\partial x_j}\right] \quad \ldots\ldots\ldots\ldots \quad (4.11)$$

$$\rho\frac{\partial \varepsilon}{\partial t} + \rho\bar{u}_j\frac{\partial \varepsilon}{\partial x_j} = \alpha^\varepsilon\frac{\varepsilon}{k}\tau_{ij}\frac{\partial \bar{u}_i}{\partial x_j} - \beta^\varepsilon\rho\frac{\varepsilon^2}{k} + \frac{\partial}{\partial x_j}\left[\left(\mu + \frac{\mu_T}{\sigma_2^\varepsilon}\right)\frac{\partial \varepsilon}{\partial x_j}\right] \quad \ldots\ldots\ldots\ldots \quad (4.12)$$

Where k is the specific turbulence kinetic energy, $x_{i,j}$ is the Cartesian coordinates system, $\bar{u}_i$ is the mean velocity component t is the time, ρ is the density, μ is the viscosity, μ_T is the eddy − viscocity, $\alpha^\varepsilon, \beta^\varepsilon, \sigma_1^\varepsilon, \sigma_2^\varepsilon$ are closure coefficients and i,j represent components in the i ,jth direction.

The k-ε model does have a number of flaws and limitations that are well documented such as performing badly with severe pressure gradients and separation. To this extent there have been a large number of modifications to the standard model to improve it. The most commonly employed of these are: RNG k-ε model and realizable k- ε model. The RNG k-ε model or Renormalization Group Method k-ε model adds a term to the turbulence dissipation equation to account for the interaction between the dissipation and mean shear. The realizable k-ε model changes one of the closure coefficients (Cε) to allow it to vary based on the velocity gradients.

II. k-*ω* Model

There are a number of methods that apply the specific dissipation rate (ω). The most common k- $\boldsymbol{\omega}$ model is often referred to as the standard k- $\boldsymbol{\omega}$ model or the Wilcox k-ω model .This model defines k using Equation 4.13 and ω using Equation 4.14.

$$\rho \frac{\partial k}{\partial t} + \rho \bar{u}_j \frac{\partial k}{\partial x_j} = \tau_{ij} \frac{\partial \bar{u}_i}{\partial x_j} - \beta_1^{\omega} \rho k \omega + \frac{\partial}{\partial x_j}\left[(\mu + \sigma_1^{\omega} \mu_T) \frac{\partial k}{\partial x_j}\right] \quad (4.13)$$

$$\rho \frac{\partial \omega}{\partial t} + \rho \bar{u}_j \frac{\partial \omega}{\partial x_j} = \alpha^{\omega} \frac{\omega}{k} \tau_{ij} \frac{\partial \bar{u}_i}{\partial x_j} - \beta_2^{\omega} \rho \omega^2 + \frac{\partial}{\partial x_j}\left[(\mu + \sigma_2^{\omega} \mu_T) \frac{\partial \omega}{\partial x_j}\right] \quad (4.14)$$

Where k is the specific turbulence kinetic energy, xi, j is the Cartesian coordinate system, $\bar{u}_j$ is the mean velocity component, t is time, ρ is density, μ is the viscosity, μ_T is the eddy-viscosity, ω is the specific dissipation rate α^{ω}, β_1^{ω}, β_2^{ω}, σ_1^{ω}, $\sigma_2^{\omega}$are closure coefficients and i, j represent components in the i, jth direction

It is known to perform better under adverse pressure gradients and for flows featuring separation than the k- ε model. It is also considered more accurate within the wall region .Even if it has been shown to be more sensitive to free stream velocities at the boundary layer edge.

III. k-*ω* SST Model

The k-ω shear stress transport model normally written k-ω SST or SST k-ω model is a combination of the standard **k- *ω*** and **k- *ε*** models defined by Menter **.**The k-ω SST model is a variation and improvement of the baseline (BSL) model. The BSL model varies between the k-ω and k- $\boldsymbol{\varepsilon}$ models in an almost linear manner whereas the k-ω SST model also accounts for the turbulent shear stress. It applies the k-ω definition in the inner part of the boundary layer and the k- $\boldsymbol{\varepsilon}$ definition outside the boundary layer (Bechmann, 2006).

Menter created one set of equations by blending the k-ω and k- $\boldsymbol{\varepsilon}$ model equations, by first transforming the k- $\boldsymbol{\varepsilon}$ model into a k-ω formulation, shown in Equation 4.15.

$$\rho\frac{\partial\omega}{\partial t} + \rho\bar{u}_j\frac{\partial\omega}{\partial x_j} = \alpha^{\omega\varepsilon}\frac{\omega}{k}\tau_{ij}\frac{\partial\bar{u}_i}{\partial x_j} - \beta_2^{\omega\varepsilon}\rho\omega^2 + \frac{\partial}{\partial x_j}\left[(\mu + \sigma_2^{\omega\varepsilon}\mu_T)\frac{\partial\omega}{\partial x_j}\right]$$

$$+2\rho\sigma_2^{\omega\varepsilon}\frac{1}{\omega}\frac{\partial k}{\partial x_j}\frac{\partial\omega}{\partial x_j} \quad \text{……………………..……………………………………. (4.15)}$$

Where $\alpha^{\omega\varepsilon}$,$\beta_1^{\omega\varepsilon}$, $\beta_2^{\omega\varepsilon}$, $\sigma_1^{\omega\varepsilon}$, $\sigma_2^{\omega\varepsilon}$ are the new closure coefficients and all other variables are as previously defined. The two models are combined to create a new set of equations for k and ω as shown in Equations 4.15.

The k-ω SST model is an improvement over the other two equation models for many flow situations, Even if it is limited by the application of the eddy-viscosity and Boussinesq hypothesis. These models assume isotropic turbulence that is not normally valid and can cause unrealistic end results

d) Reynolds Stress Model

The Reynolds Stress Model (RSM) also known as a second moment closure model, closes the Reynolds-Averaged Navier-Stokes equations without relying on the Boussinesq hypothesis. Instead, it solves additional transport equations for all components of the Reynolds stress tensor (ti j) (Bechmann, 2006). Conversely, the derivation of the RSM necessitates higher order correlations to be modelled. RSM avoids the isotropic eddy-viscosity assumption allowing the full 3D nature of turbulence to be modelled. This added accuracy necessitates additional computational resources to solve the additional equations.

Nearly all RSMs start from the same point, the exact differential equation of the Reynolds stress tensor as shown in Equation 4.19.

$$\frac{\partial\tau_{ij}}{\partial t} + \bar{u}_k\frac{\partial\tau_{ij}}{\partial x_k} = -\tau_{ik}\frac{\partial\bar{u}_j}{\partial x_k} - \tau_{jk}\frac{\partial\bar{u}_i}{\partial x_k} + \varepsilon_{ij} - \pi_{ij} + \frac{\partial}{\partial x_k}\left[v\frac{\partial\tau_{ij}}{\partial x_k} + C_{ijk}\right] \quad \text{……………. (4.16)}$$

$$\varepsilon_{ij} = 2v\overline{\frac{\partial u_i'}{\partial x_k}}\overline{\frac{\partial u_j'}{\partial x_k}} \quad \text{…………………………………………………...............……… (4.17)}$$

$$\pi_{ij} = p'\left(\overline{\frac{\partial u_i'}{\partial x_j}} + \overline{\frac{\partial u_j'}{\partial x_i}}\right) \quad \text{……………………………………………………………….……. (4.18)}$$

$$C_{ijk} = \overline{pu_i'u_j'u_k'} + \overline{p'u_i'}\delta_{jk} + \overline{p'u_j'}\delta_{ik} \quad \text{……………………………………….…...... (4.19)}$$

$$\rho \frac{\partial k}{\partial t} + \rho \bar{u}_j \frac{\partial k}{\partial x_j} = \tau_{ij} \frac{\partial \bar{u}_i}{\partial x_j} - C\rho \frac{k^{3/2}}{l} + \frac{\partial}{\partial x_j}\left[\left(\mu + \frac{\mu_T}{\sigma_k}\right)\frac{\partial k}{\partial x_j}\right] \qquad (4.20)$$

Whereε_{ij} is the dissipation tensor, π_{ij} is the pressure-strain correlation tensor, C_{ijk} is the turbulent transport tensor, $\tau_{ij}$is the Kronecker delta and all other variables areas previously described.

RSM is good for accurately predicting complex flows as it accounts for streamline curvature, swirl, rotation and high strain rates. Even if it does struggle with stability without the eddy viscosity term and has a higher computational expense (2−3 times) compared to the other turbulence models

4.1.2 Large Eddy Simulations (LES)

As the name suggests, LES resolves large eddies while eddies smaller than the grid size are modelled using a sub-grid scale (SGS) model. This approach is based on the assumption that the smallest eddies have a more or less universal characteristic that is not dependent on the flow geometry. This distinction between resolved and modelled is done through a filtering function applied to the Navier-Stokes equations. This introduces a new term named the SGS stress (similar to the Reynolds stress tensor of the RANS method). This stress is applied to represent the effects of the SGS modelled eddies on the larger resolved eddies of the flow. This stress needs to be calculated and there are a large number of models available.

CFD modeling has come a long way in the past couple decades and has made great progress in the field of wind energy. In the most ideal simulation, the entire farm of fully resolved, rotating turbines would be modeled with a very fine grid, and the solution would be achieved using LES with a tuning-free SGS model.

LES is generally considered the engineering research standard turbulence model. It is not a RANS model, but rather a filtered solution of the continuity, Navier-Stokes, and heat equations. This formulation places in the turbulence model hierarchy between direct numerical simulations (DNS), where all scales are resolved down to the Kolmogorov length scale, and RANS where all scales are modeled. LES is able to handle unsteady anisotropic turbulent flow much better than RANS, but inquires more computational resources. LES is increasingly being applied due to the increase in computer power and resources that are now available Through this filtering method, LES resolves the larger energy-containing motions while modeling the sub grid-scale motions. This gives for a much higher accuracy than

RANS models produce. However, LES simulations necessitate a much finer grid resolution and this increases computation time at least linearly. Most LES simulations necessitate a filter and grid resolution such that 80% of the energy is resolved (Pope, 2010). For simulations in this thesis work a dynamic Smagorinsky-Lilly SGS model was applied. Relaxation factors had to be adjusted to impart stability.

The equations describing the motion of any incompressible Newtonian fluid in abounded domain are the well-known Navier-Stokes equations.

$$\rho\left(\frac{\partial u}{\partial t}+u\frac{\partial u}{\partial x}+v\frac{\partial u}{\partial y}+w\frac{\partial u}{\partial z}\right)=-\frac{\partial p}{\partial x}+\mu\left(\frac{\partial^2 u}{\partial x^2}+\frac{\partial^2 u}{\partial y^2}+\frac{\partial^2 u}{\partial z^2}\right)+S_x \quad (4.17)$$

$$\rho\left(\frac{\partial v}{\partial t}+u\frac{\partial v}{\partial x}+v\frac{\partial v}{\partial y}+w\frac{\partial v}{\partial z}\right)=-\frac{\partial p}{\partial y}+\mu\left(\frac{\partial^2 v}{\partial x^2}+\frac{\partial^2 v}{\partial y^2}+\frac{\partial^2 v}{\partial z^2}\right)+S_y \quad (4.18)$$

$$\rho\left(\frac{\partial w}{\partial t}+u\frac{\partial w}{\partial x}+v\frac{\partial w}{\partial y}+w\frac{\partial w}{\partial z}\right)=-\frac{\partial p}{\partial z}+\mu\left(\frac{\partial^2 w}{\partial x^2}+\frac{\partial^2 w}{\partial y^2}+\frac{\partial^2 w}{\partial z^2}\right)+S_z \quad (4.19)$$

Where x, y, z is the Cartesian coordinate system, u, v, w is the Cartesian velocity system, t is time, ρ is density, p is the pressure, μ is the viscosity and S x, y, z is a source term.

The differentiation between the large eddies (resolved) and the small eddies (modelled) of the flow field are accomplished using a filtering method. The filtering process effectively filters out eddies smaller than the filter width. A common filtering method decomposes a flow variable $\psi(x,t)$ into the large scale filtered part $\bar{\psi}(x,t)$ and small scale sub-filtered part $\psi'(x,t)$:

$$\psi(x,t)=\bar{\psi}(x,t)+\psi'(x,t) \quad (4.20)$$

$$\bar{\psi}(x_0)=\int_{\Theta}\psi(x,t)\,G(\Delta)dx' \quad (4.21)$$

Where Θ is the fluid domain, G is the filter function.

The filter function depends on the filter width D= $(D_1D_2D_3)^{1/3}$ where Di is the filter width in the i^{th} direction. There are a number of different filtering functions, the most common are the Gaussian filter, the top hat or box filter, and cut-off filter as shown in Equation 4.22, 4.23 and 4.24, respectively.

$$G=\left(\frac{6}{\pi\Delta^2}\right)^{3/2}\exp\left(-6\frac{|x_0-x|^2}{\Delta^2}\right) \quad (4.22)$$

$$G = \begin{cases} \frac{1}{\Delta} & \text{if } |x_0 - x| \le \frac{\Delta_i}{2} \\ 0 & \text{other wise} \end{cases} \quad \text{………………………………………………………} \quad (4.23)$$

$$G = \prod_{i=1}^{3} \frac{\sin\left(\frac{\pi}{\Delta_i}(x_0 - x)\right)}{\pi(x_0 - x)} \quad \text{………………………………………………………………} \quad (4.24)$$

Whichever filtering function is applied it is applied to the Navier-Stokes equations to create filtered equations, as shown in Equations 4.25 and 4.26, which are solved in LES simulations.

$$\frac{\partial \bar{U}_i}{\partial x_i} = 0 \quad \text{……………………………………………………………………} \quad (4.25)$$

$$\frac{\partial \bar{U}_i}{\partial x_i} + \frac{\partial(\bar{U}_i \bar{U}_j)}{\partial x_j} = -\frac{1}{\rho}\frac{\partial \bar{P}}{\partial x} - \partial\tau_{sgs} + v\frac{\partial^2 \bar{U}_i}{\partial x^2} + S_i \quad \text{…………………………………….} \quad (4.26)$$

Where $\bar{U}_i$the large-scale is filtered component and τ_{sgs} is the subgrid scale stress term.

4.1.2.1 Sub-grid Scale Models

Most sub-grid scale models are eddy-viscosity models using the Boussinesq hypothesis. The most widely applied models are based on the Smagorinsky model (Smagorinsky, 1963) that applies an algebraic eddy-viscosity. This has been applied due to its simplicity as the SGS eddy viscosity (μ_{sgs}) is determined by:

$$\mu_{sgs} = \rho(C_S\Delta)^2\sqrt{2\bar{S}_{ij}\bar{S}_{ij}} \quad \text{…………………………………………………………} \quad (4.27)$$

Where $\bar{S}_{ij}$ is the rate-of-strain tensor for the resolved scale, $C_S$is the Smagorinsky constant usually varying between 0.1 to 0.2

From the models based on the Smagorinsky model (Smagorinsky, 1963) the most commonly applied is the Smagorinsky-lilly model (Lilly, 1966) which applies a modified SGS eddy-viscosity given by:

$$\mu_{sgs} = \rho L_s^2\sqrt{2\bar{S}_{ij}\bar{S}_{ij}} \text{…………………………………………………………………………..} \quad (4.28)$$

$$L_S = \min\left(ky_d \, , C_s \, V^{1/3}\right) \text{……………………………………………………………………} \quad (4.29)$$

Where L_S is the mixing length for the SGS, k is the von Karman constant, y_d is the distance to the closest wall, C_s is the Smagorinsky constant, and V is the volume of the computational cell.

One problem with these models is that Cs is not universal. Lilly derived a value of 0.17 for homogeneous isotropic turbulence. Conversely, this can cause excessive dampening near solid boundaries and a value of around 0.1 has been found to yield the best end results for a wide range of flows.

LES is a transient method, requiring time discretization and definition of a time step. This is normally defined to keep stability and to accurately resolve turbulence in time. The most common condition is the Courant–Friedrichs–Lewy (CFL) condition that necessitates:

$$\left|\frac{u\Delta t}{\Delta x}\right| \leq 1 \qquad \text{....} \qquad (4.30)$$

Where Δt the time step and Δx is the spatial step

4.2 ANSYS-FLUENT

ANSYS Fluent is commercially available general-purpose finite volume code used to model turbulence, heat transfer, and reactions and has several solvers and discretization sorts. It has been applied for several wind turbine studies featuring single blades (Mahu, 2011; Qunfeng et al., 2011), for full rotors (WuBow et.al, 2007) as well as actuator discs (Makridis, 2009; Makridis, 2013).

4.2.1 Model Description

The geometry of the designed reference turbine was created in SolidWorks to the specifications found in the potential assessment and Blade design section (3.1 &3.2) for rated conditions. This geometry was then exported into ANSYS Design-Modeler, where the domain geometry was created. The domain was sized (15 m) upstream of the turbine, (27m) downstream of the first turbine, and (15m) span wise on either side of the turbines. The total height of the domain was set to (30m). Eventually the whole model and flow tunnel was scaled down to a ratio of one to hundred.

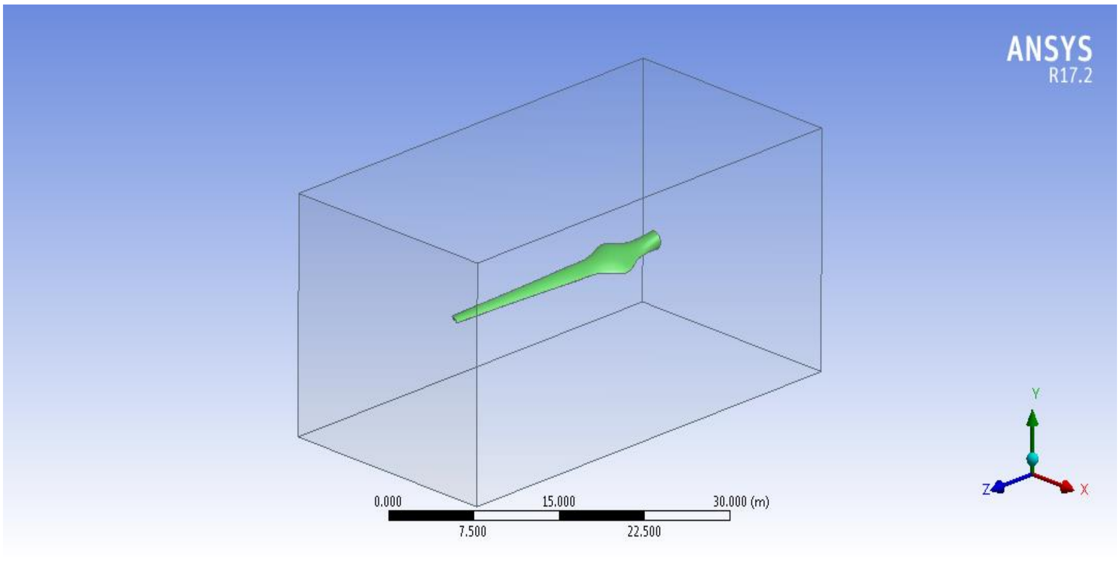

Figure 4.2 : Baseline model in Virtual flow tunnel

The following figures illustrate HAWT blades; baseline blade model and six other different dimple orientation imparted on the baseline model are included. In order to simulate the fluid mechanics phenomena these models are imported into ANSYS-DESIGN MODELER and the corresponding virtual wind tunnel is created.

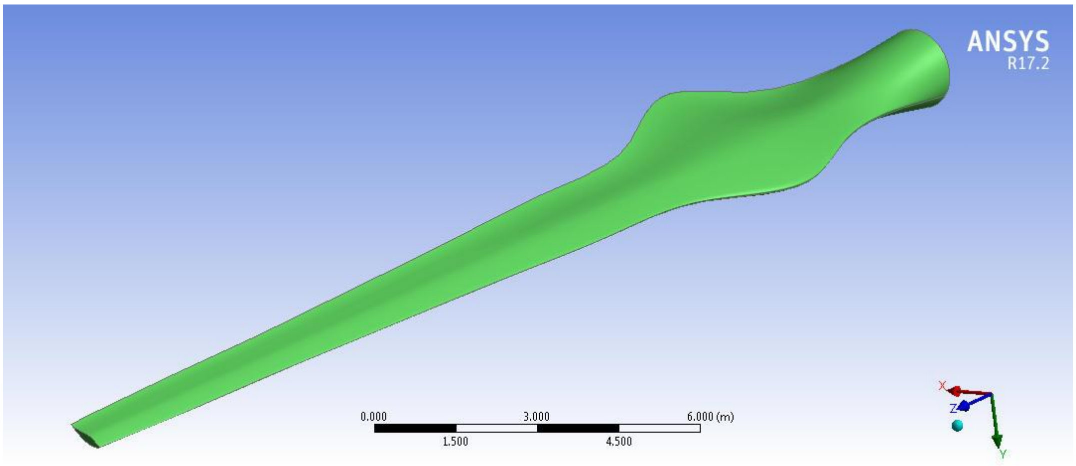

Figure 4.3 : Baseline Model

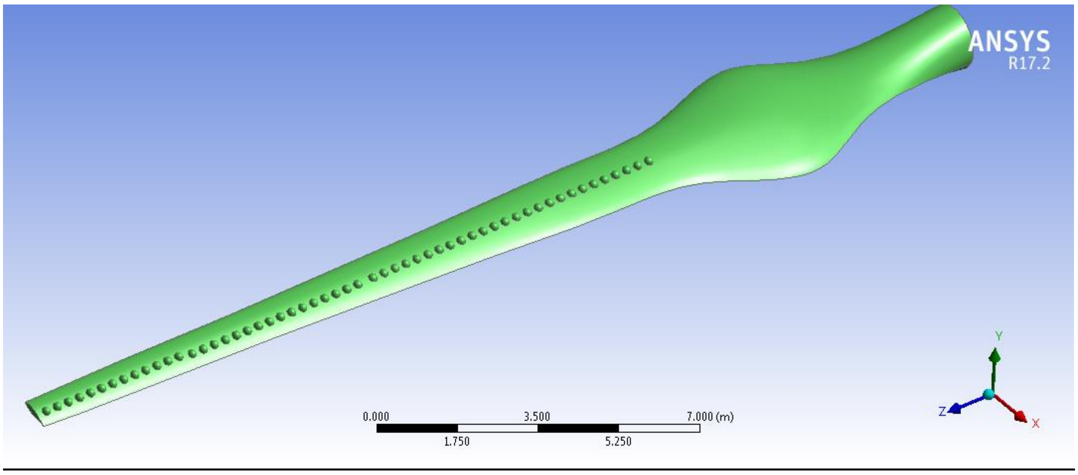

Figure 4.4 : Blade with Dimple Orientation One.

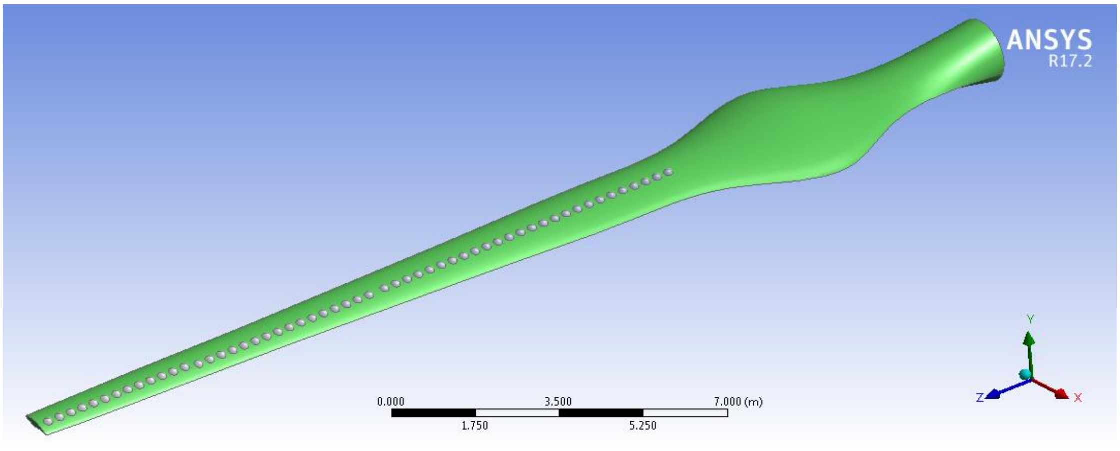

Figure 4.5 : Blade with Dimple Orientation Two.

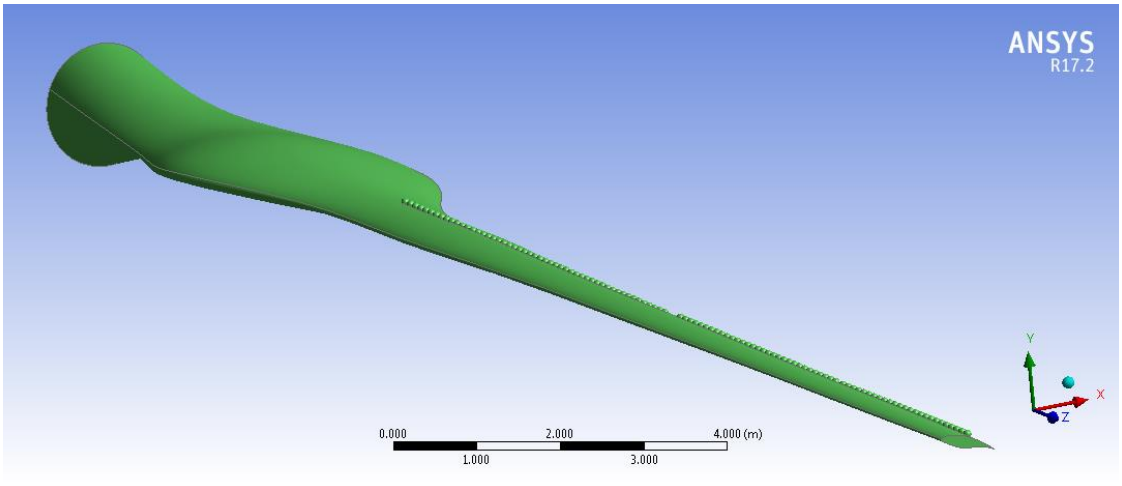

Figure 4.6 : Blade with Dimple Orientation Three.

Configuration number one, three and five include an outward dimple with a distinct diameter while, for configuration number two, four and six inward dimples are imparted and the corresponding aerodynamic consequence is examined.

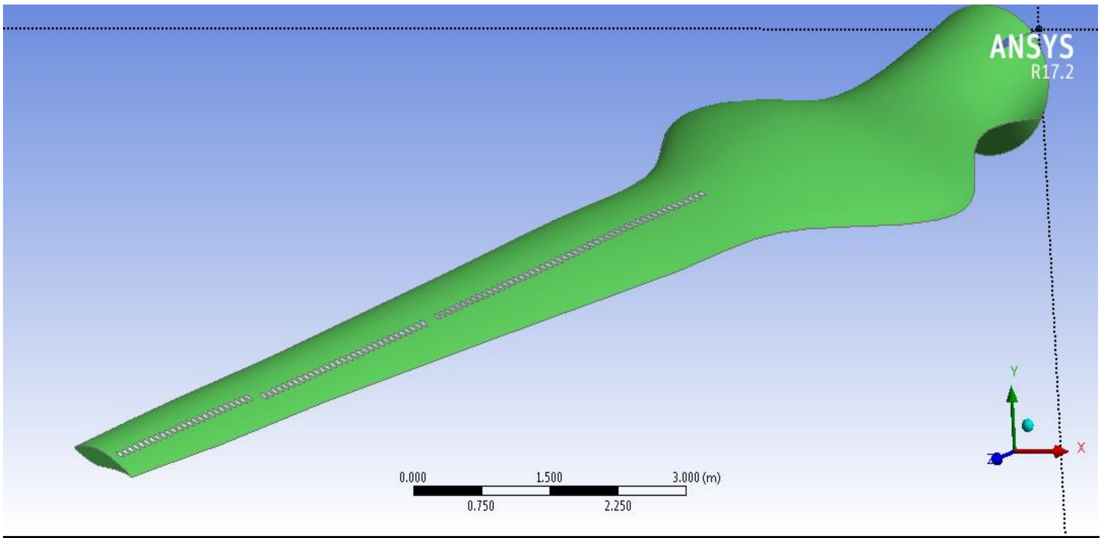

Figure 4.7 Blade with Dimple Orientation Four.

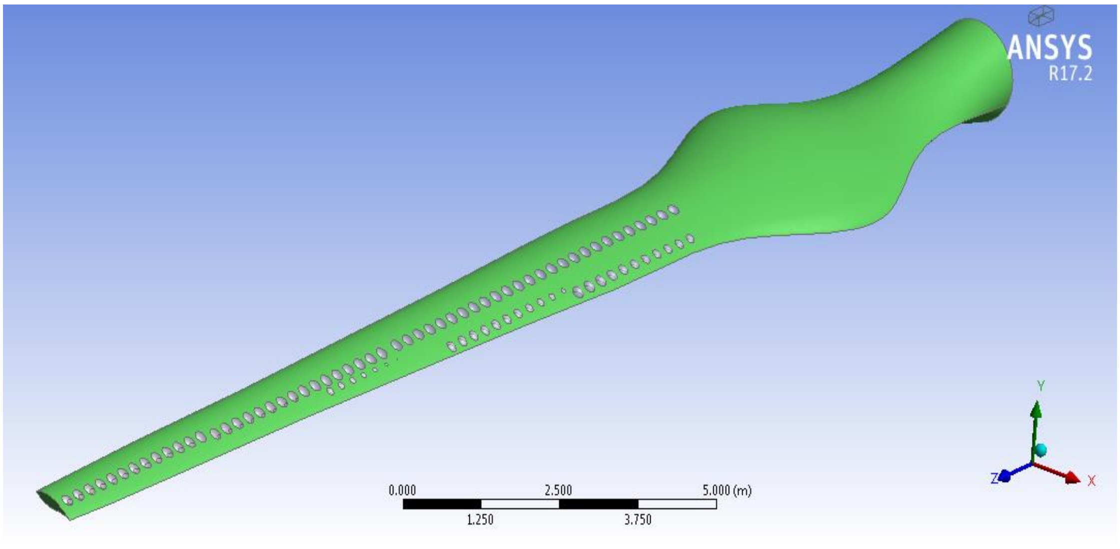

Figure 4.8 : Blade with Dimple orientation Five.

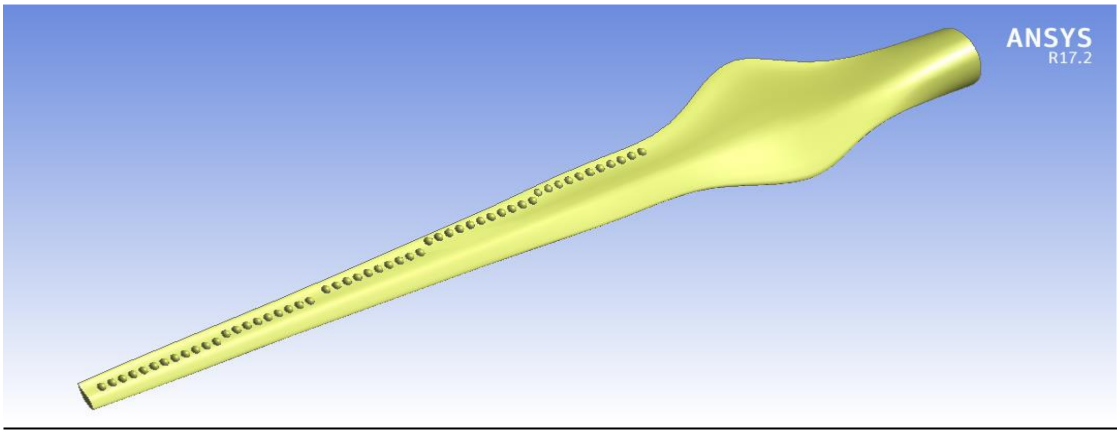

Figure 4.9 : Blade with Dimple orientation Six suction face.

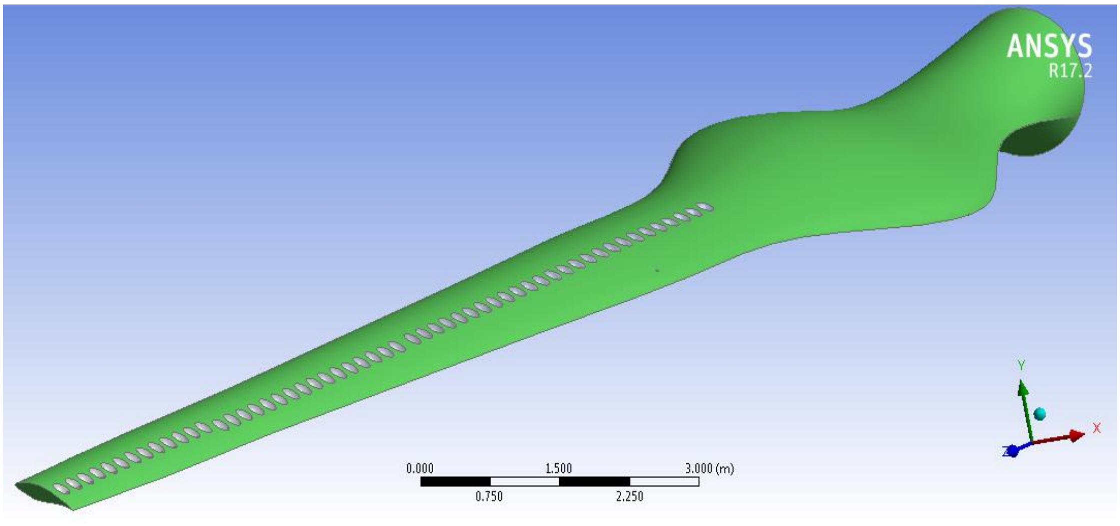

Figure 4.10 : Blade with Dimple Orientation Six.

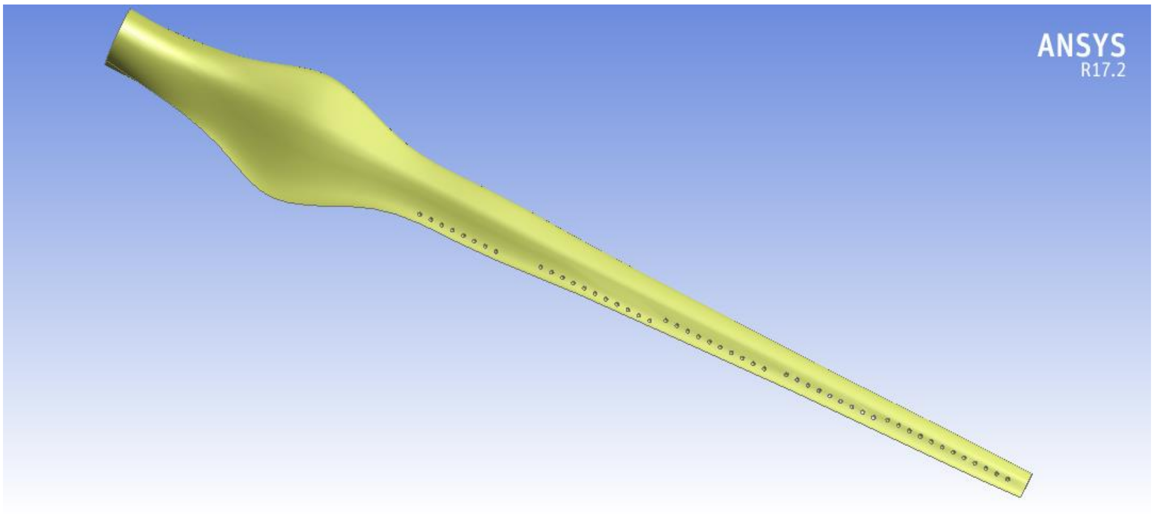

Figure 4.11 : Blade with Dimple Orientation Six Suction Face

Table 2 Specification of Models

Model Name	Span length	Airfoil type	Dimple specification	Location
Baseline	25m	S830	-	-
CONFIG. One	25m	S830	10cm, outward	0.5 of chord length on the suction surface
CONFIG. Two	25m	S830	10cm,inward	0.5 of chord length on the suction surface
CONFIG. Three	25m	S830	5cm,outward	0.4 of chord length on the suction surface
CONFIG Four	25m	S830	5cm,inward	0.4 of chord length on the suction surface
CONFIG. Five	25m	S830	10cm,outward	0.5 of chord length both on the suction and pressure surface
CONFIG. Six	25m	S830	10cm,inward and 0.5 inward at suction surface	0.5 of chord length on suction side & 0.8 of chord length on pressure side

4.2.2 Meshing

The no-slip condition is applied if the LES filtered Navier–Stokes equations are integrated to the wall, which necessitates fine grids with near-wall grid points $y^+ \leq 1$. For high Reynolds number flows with thin boundary layers it is necessary to economize on computing resources by means of graded non uniform meshes. (Versteeg, 2007)

Meshing is performed in ANSYS Meshing using an unstructured tetrahedral mesh. Cell sizes were set to one millimeter on the blade faces, 0.5 millimeter on the blade tips. Cells were kept to a maximum size of 1 mill-meters in the horizontal directions and vertical direction. Inflation layers were implemented on all solid surfaces with a maximum growth rate of 1.2. The meshes of all variations of the stationary reference turbine contained approximately two million cells.

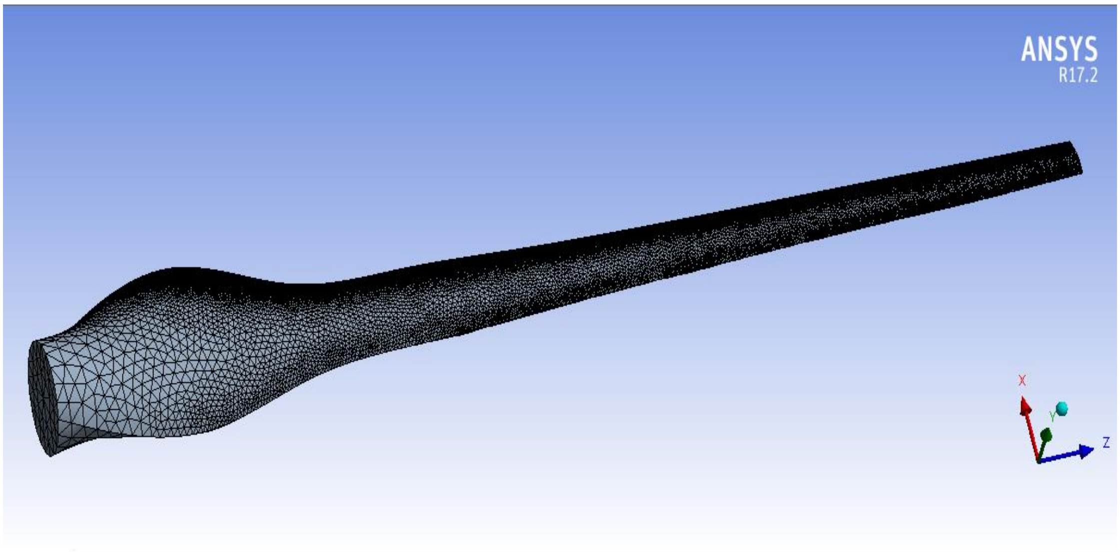

Figure 4.12 : Blade mesh.

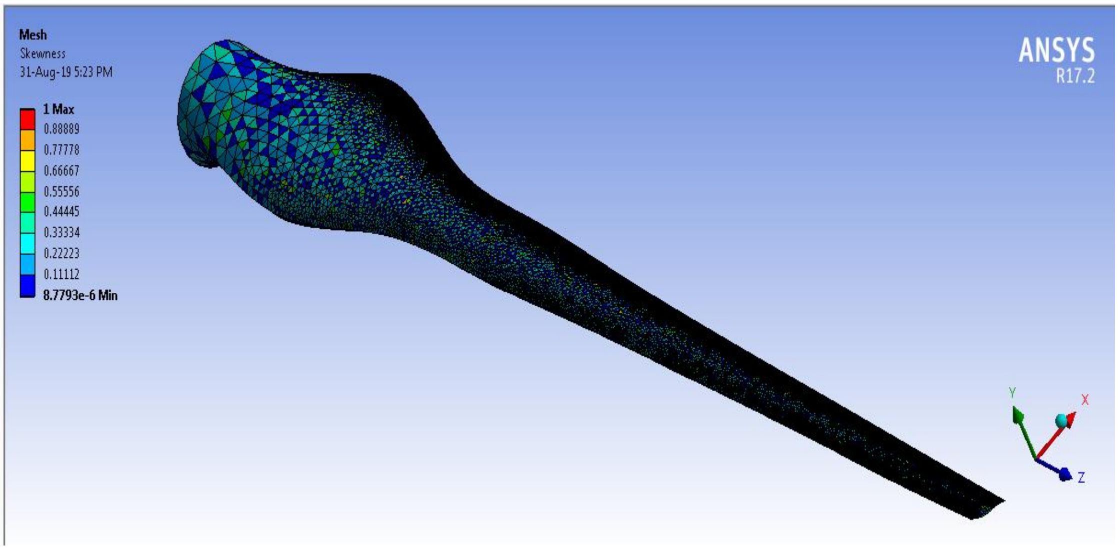

Figure 4.13 : Blade Mesh Skewness.

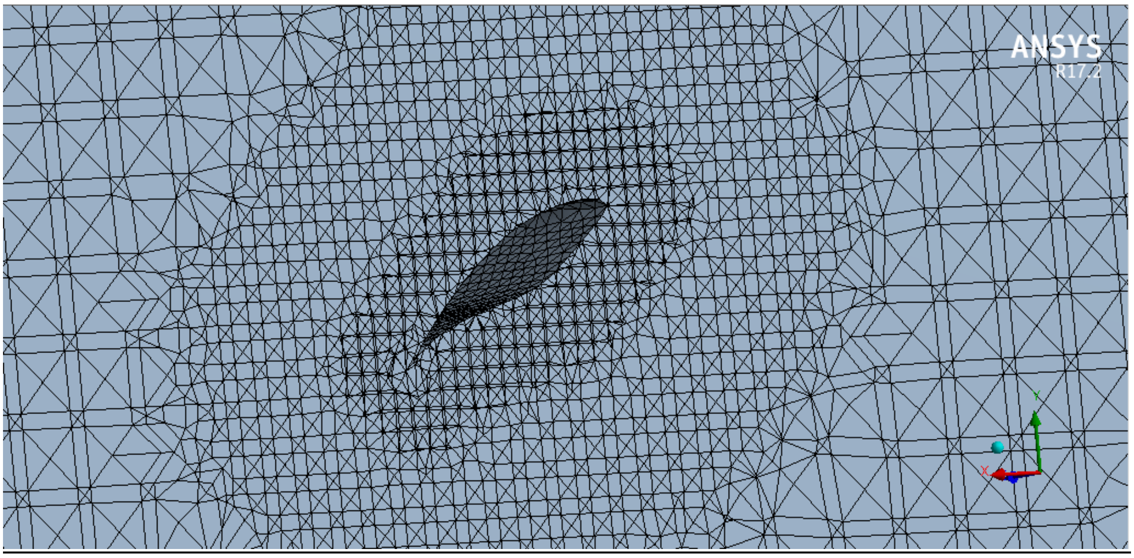

Figure 4.14 : Detail of a mesh slice, showing a blade section and the adjacent refinement region on virtual flow tunnel

4.2.3 Grid Independence Study

The first concern for the quality of the solution is the influence of the surface mesh on the Solution Since the boundary is interpolated onto the solution grid. The approximation of the Surface mesh as a representation of the geometry can cause errors if not refined enough. In order to evaluate the goodness of this approximation the surface mesh is rearranged in both finer and coarse spacing between elements. Simulations of the baseline model at $\alpha=15^{o}$ is selected for the test; similar fluid grid used were computed with the finer and coarser surface mesh, which showed that the solution is independent of the surface mesh; as can be seen in the plots Figure 6.29 and Figure 6.30. In general, the surface mesh need to be refined, but the surface used for the first simulations is accurate enough to capture the most important flow features in the present thesis. These results show that the solution is independent of the surface mesh. (ANSYS-FLUENT setup of GIS is presented in Appendix: A-3)

Table 3: Grid independence study (GIS)

Mesh name	Element size	Number of elements	Lift coefficient	Drag coefficient
Mesh-1	3mm	436,911	1.85	0.428
Mesh-2	2mm	855,713	2.08	0.3758
Mesh-3	1mm	1,942,807	2.109	0.349
Mesh-4	0.9 mm	2,234,257	2.1	0.347
Mesh-5	0.7mm	3,520,421	2.08	0.335
Mesh-5	0.5mm	5,258,523	2.072	0.332

4.2.4 Solution Scheme

All CFD modeling was performed in ANSYS FLUENT V. 17.0; Models were run as transient LES at a Reynold number of $1.32x10^6$.Lilly Model was selected for the sub-grid scale with a model constant of 0.1(Lilly, 1966) .

The pressure field is unknown in most applications and the main task in fluid stream modeling is how to relate the pressure to the velocity distribution. The main velocity-pressure coupling algorithms are SIMPLE (Semi-Implicit Method for Pressure Linked Equations) Algorithm, SIMPLER (SIMPLE Revised) Algorithm which is an improvement of simple algoritghm , SIMPLEC Algorithm(SIMPLEC differs from SIMPLE only in velocity correction) , PISO (Pressure Implicit with Splitting of Operators) Algorithm and Coupled (Versteeg, 2007).

In this thesis Coupled pressure-velocity coupling algorithm is selected for its fast convergence quality and good accuracy. For spatial discretization there are a number of methods studied in computional fluid dynamics studies among them second-order have a better accuracy and convergence rate (Versteeg, 2007); suitable initial and boundary conditions must be supplied to generate a well posed problem. Rated wind speed of the site is found as 10m/s, In spite of that for creating uniform Reynold number for actual size and scaled down model the simulation is carried out at wind speed of 1000m/s.

CHAPTER FIVE

EXPERIMENTAL EVALUATION

In this section, the details of the experimental procedures done to complete this study are explored. It covers the model preparation, test equipment needed, the measurement technique and equipment, and the uncertainty of the experimental measurements.

5.1 Model Preparation

3D printing, also recognized as additive manufacturing, is a new form of manufacturing developed in the 1980s. It append material layer by layer to create an object instead of removing it from a solid block of material like older manufacturing approaches do. Before printing a feature on a 3D printer, it is designed on a CAD software and afterward "sliced" by a specific program. It means that the needed course of the head extruder to produce the object is computed.

In this study 3D printing was the best choice to manufacture the HAWT airfoils, due to the fact that it is the best economic choice to maintain an acceptable surface resolution and to capture the geometric features. It is important to note that the different blade cross-section was mounted at the wind tunnel test section with similar phenomena of the wind to ensure the uniformity of test parameters.

Figure 5.1 : 3D-Printer

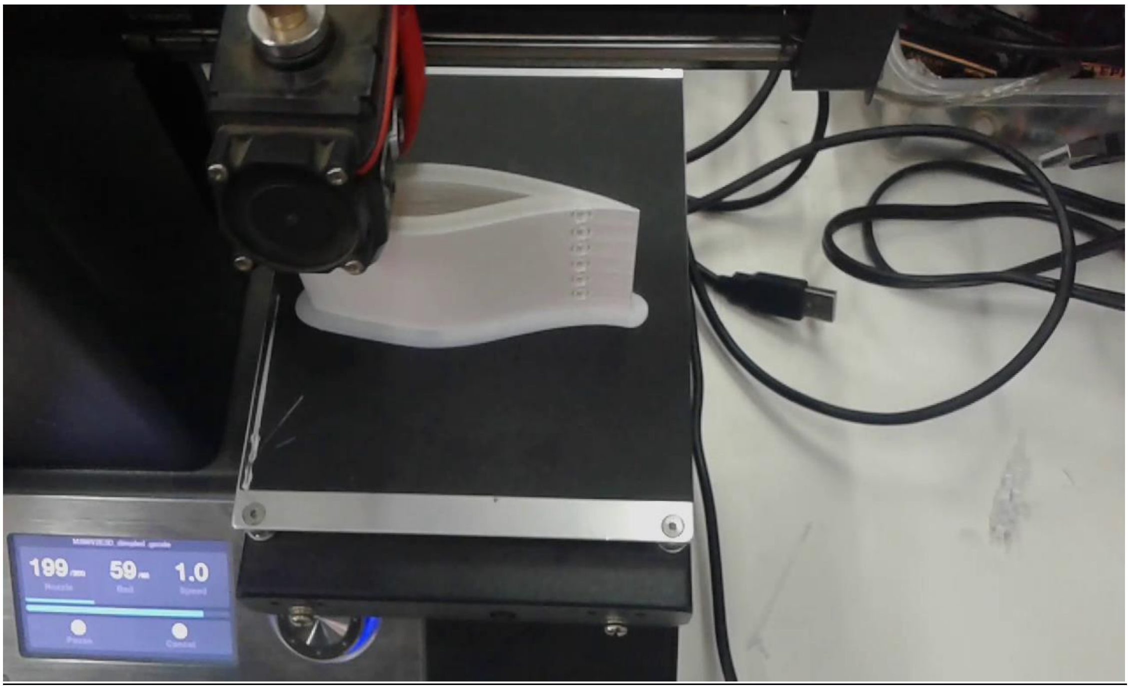

Figure 5.2 : Printing Model II

5.2 Test Equipment

All testing was performed in the ASTU Subsonic Wind Tunnel (HM 170 demonstration wind tunnel) developed for experimentation and demonstration purposes in the field of aerodynamics and fluid mechanics, by GUNT Inc. Its subsonic, open wind tunnel with a square measurement section profile. The extensive range of available accessories permits the performance of numerous experiment. The HM170 demonstration wind tunnel is an open wind tunnel of the named Eiffel type, where the air is drawn in from outside and blown back out in to the open. This wind tunnel reach a Mach number of about **Ma=0.1**.

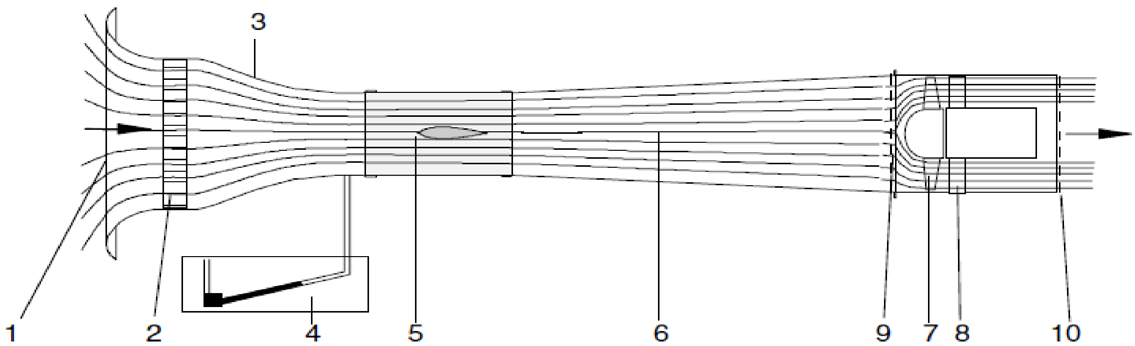

Figure 5.3 : Schematic Diagram of Astu's Wind Tunnel

The air is drawn in from the atmosphere via the streamlined funnel (1).Any transverse stream components are filtered out in the flow strainer (2).It's made of a tubular honey comb structure. The air exits from the stream strainer as a parallel flow and is accelerated to roughly 3.3 times its original velocity in the jet(3).The static pressure(4) is measured downstream of the jet entrance to the measurement section. Based on the assumption of virtually loss free flow, the stream velocity can be determined from the pressure difference with respect to ambient pressure(Total pressure at zero velocity).The air then flows through the measurement section(5) which has a constant cross-section. After the measurement section the flow is decelerated in the diffuser (6) and part of the pressure drop required to accelerate the air in the jet is recovered. The diffuser angle is designed in a way to prevent flow separation. An axial fan (7) with downstream guide (8) draws the air out of the diffuser and conveys in to the open. A guard (9) in front of the fan prevents damage caused by foreign matters or model, whereas the guard (10) following the fan prevents contact with the fan when it's in operation.

The wind tunnel has a velocity range of 0.6-28 m/s, a turbulence intensity of 0.2% and a 24x24x48 inch test section. Additionally, the velocity variation over the test section is less than +/-1%.

Figure 5.4 : ASTU wind tunnel

5.3 Test Apparatus

The airfoil testing was performed using the "GUNT" manufactured force balance constructed for the ASTU Subsonic Wind Tunnel. The mounting rig allows for the adjustment of angle of attack by a friction screw. The flow forces at the model are measured electrically in this wind tunnel. The forces are converted via the lever arm of the model holder in to proportional moments which deform a bending and torsion beam. The deformation is measured with strain gauge and displayed digitally as force on a two- channel measurement amplifier.

Figure 5.5 : Force Transducer

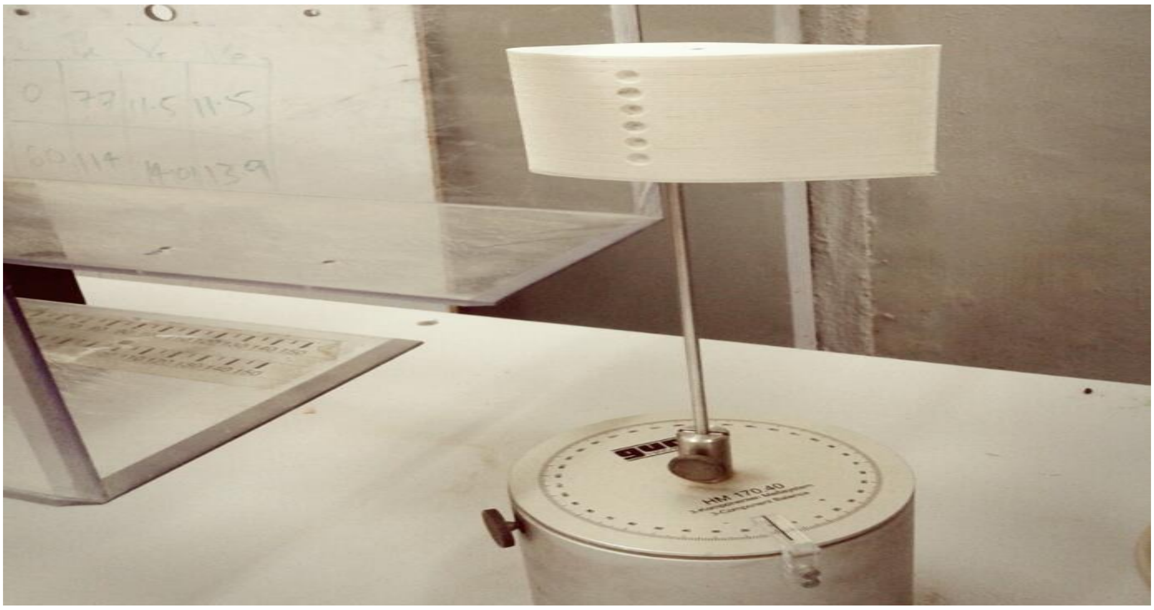

Figure 5.6 : Baseline-S830 Airfoil Model in Test Section

5.4 Testing

To ensure valid airfoil data, testing was performed at a varied angle of attack ranging from -10º to 30 º to examine the consequence of dimples on aerodynamic performance of the airfoils. Detailed testing was performed at a Re between (54486- 148082) and is within this range of insensitivity.

Figure 5.7 : Dimpled S830 Model on Test Section

At different wind speed and angle of attack six experiments were carried out .In order to change the AOA there is degree scale on the mounting ring. In one experiment for one model ten different flow phenomena are examined by varying the angle of attack.

Figure 5.8 : Force Sensor and Mounting Rig

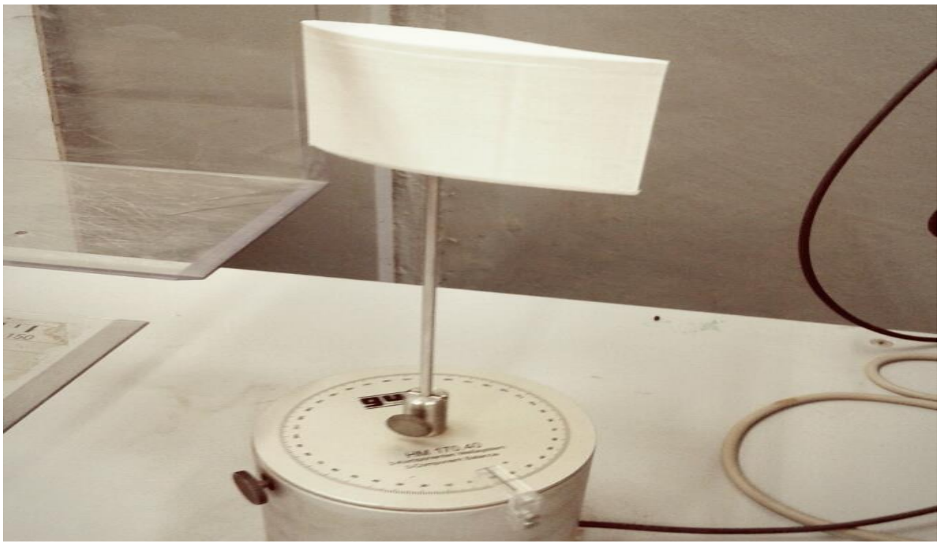

Figure 5.9 : Baseline-S830 Airfoil Model in Test Section

5.5 Summary of Experimental Procedure

Step 1: Model preparation using 3D-printer

Step2: Assemble model in the mounting Rig

Step 3: calibrating force sensor to null value

Step 4: close the test section after ensuring secure installation of the models at the required AOA

Step 5: Run wind flow at the intended wind speed

Step 6: Read the lift force and drag force from the display

Step 7: Repeat all steps starting step-2 for different Reynold number, AOA and Model

CHAPTER SIX

RESULTS AND DISCUSSIONS

This section presents the results of numerical investigations of the wind energy potential assessment, wind turbine blade design and dimples effect; Experimental validation result is also presented in this section.

6.1 Wind Potential of WETER

6.1.1 Mean Wind speed

Wind speed is prime factor which will determine sites suitability for wind farm. The mean wind of the selected site at a hub height of 80m is calculated by using the data source from metrological station Mast and satellite data. The satellite data have a wind speed phenomenon data at the inquired height while the metrology data is taken from a Mast with height of 10m; hence, it's extrapolated to 80m hub height. The two data sources results are compared and reveals a good agreement. Figure (6.1, 6.2, and 6.3) shows result of monthly mean wind speed at a height of 80m for consecutive years starting from 2009 to 2018.

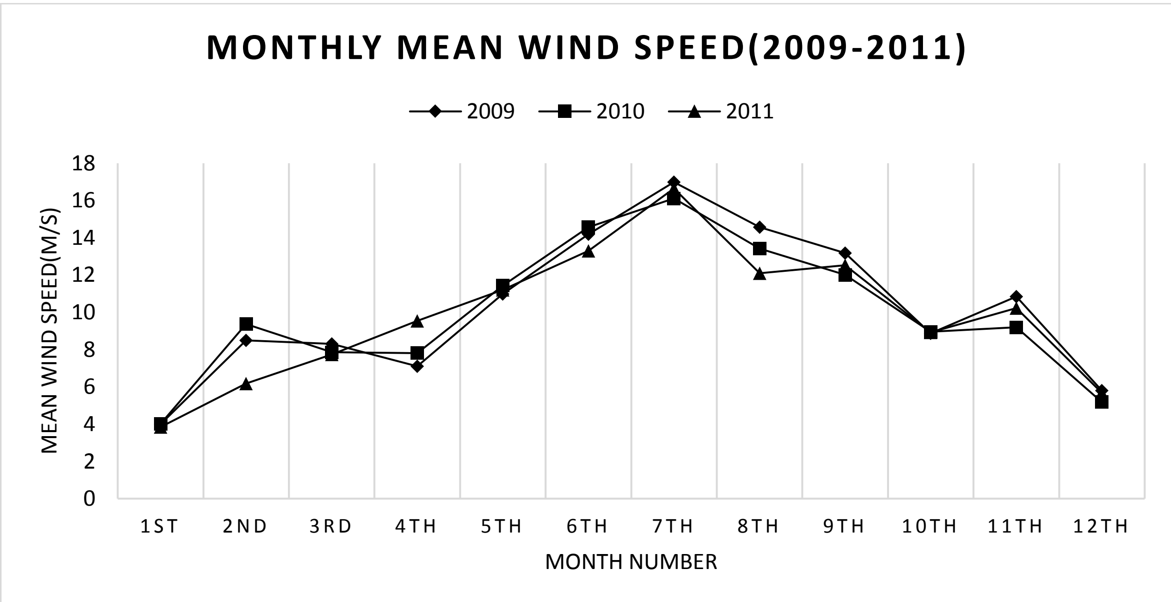

Figure 6.1 : Monthly Mean Wind Speed (2009-2011)

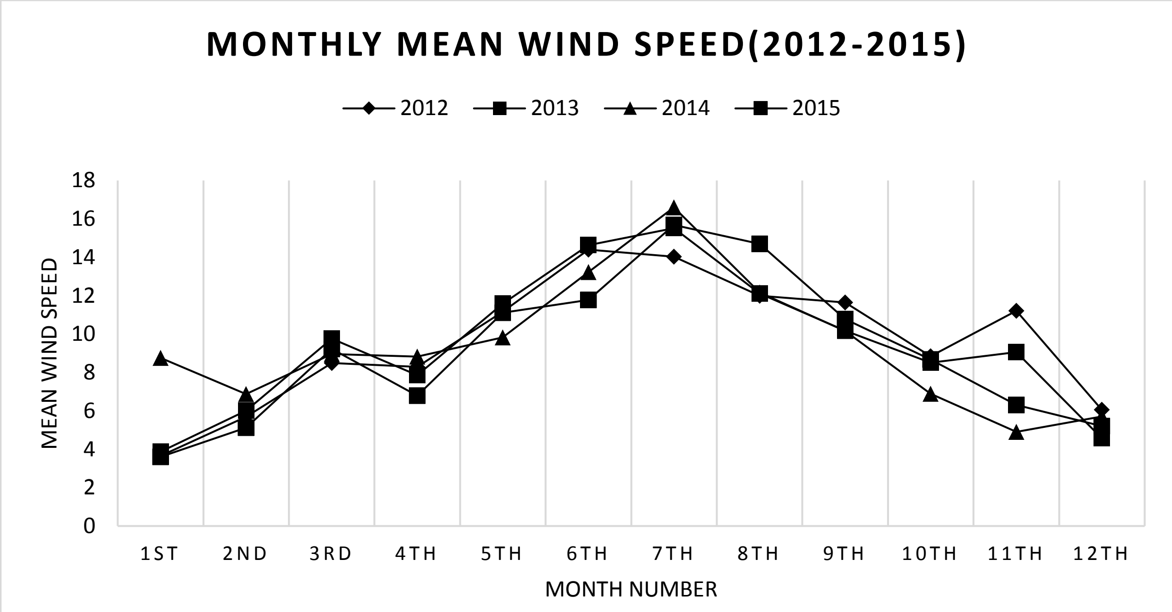

Figure 6.2 : Monthly Mean Wind Speed

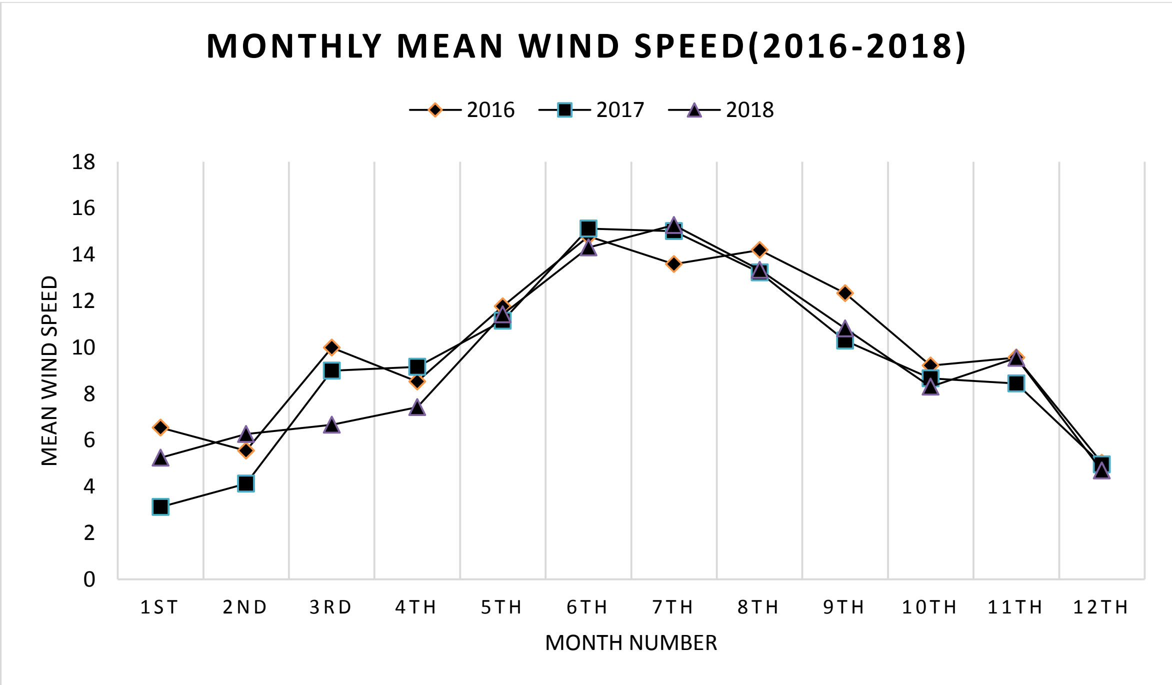

Figure 6.3 : Monthly Mean Wind Speed (2016-2018)

The above result showed that WETER have a mean wind speed ranging from 3 m/s to 18 m/s. Figure 6.1 depict the ten year average mean wind speed of the site ranges from 5m/s to 15m/s. The highest wind speed season is from May to October while the least will occur on December and January. Wind speed largely determines the amount of electricity generated by a turbine. Higher wind speeds generate more power because stronger winds allow the blades to rotate faster.

6.1.2 Sites' Wind Direction and Distribution

Wind rose is a diagram which illustrate the prevailing wind direction along with its matching frequency of occurrence .The underneath diagram shows the sites wind direction; south (S) and south-East-South (SES) is the most frequent wind direction of the site. Therefore, any wind turbine installation of the site should be facing this wind direction

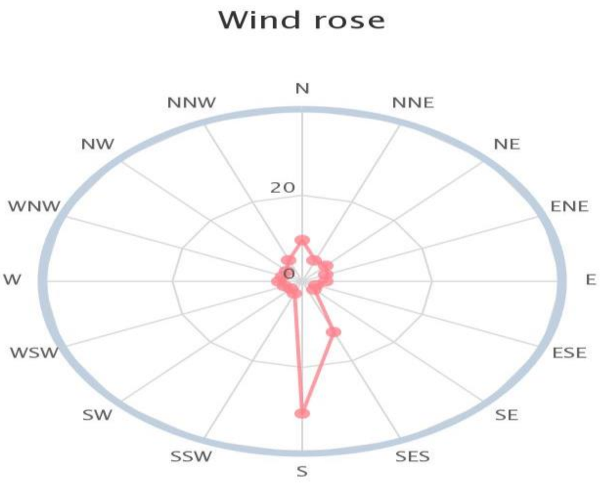

Figure 6.4 : Wind Rose of the Site

Wind energy is intermittent energy sources; occur with irregular interval. Hence hereunder Figure 6.5 depicts frequency of occurrence result for different wind speed. The result vividly exhibit most frequent wind speed of the site is between 6m/s and 13m/s.

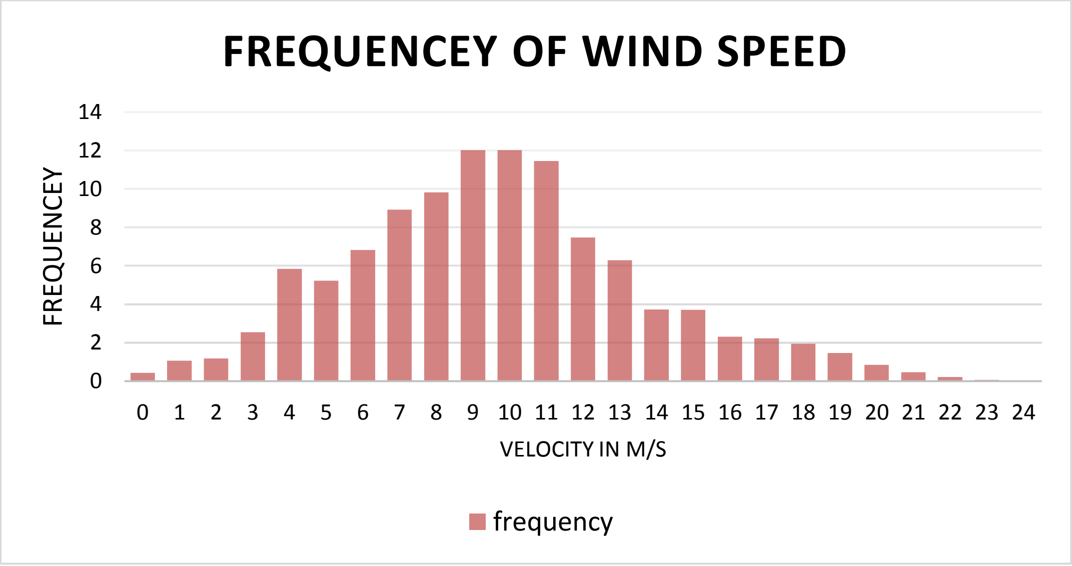

Figure 6.5 : Frequency of Occurrence of Wind Speed

6.1.3 Wind power Density (WPD)

WPD is quantitative measure of wind energy available at any location. It is the mean annual power available per square meter of swept area of a turbine, and is calculated for distinct heights above ground.

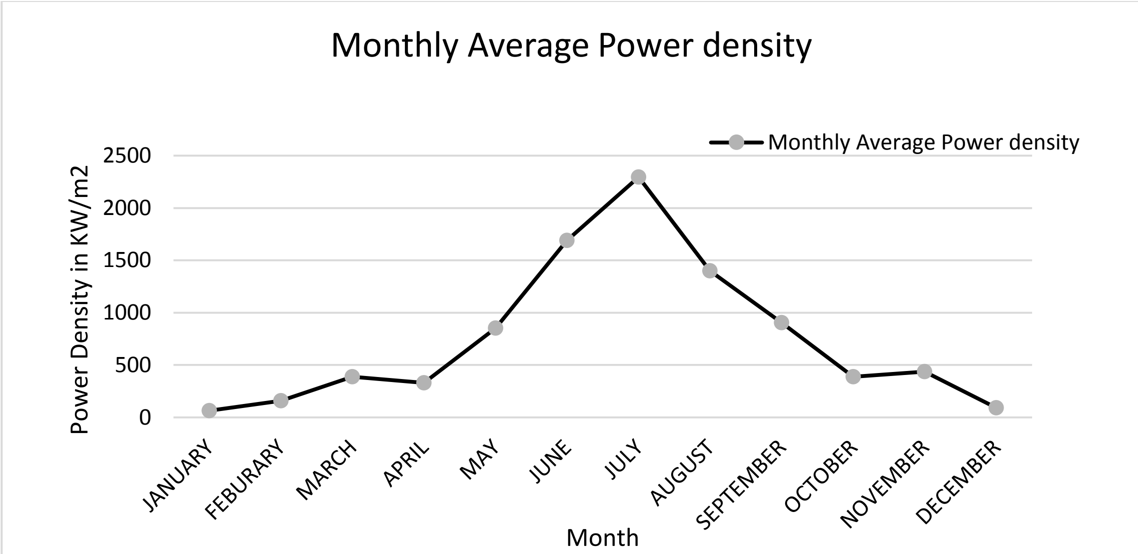

Figure 6.6 : Monthly Average Wind Power Density at Hub Height Of 80m

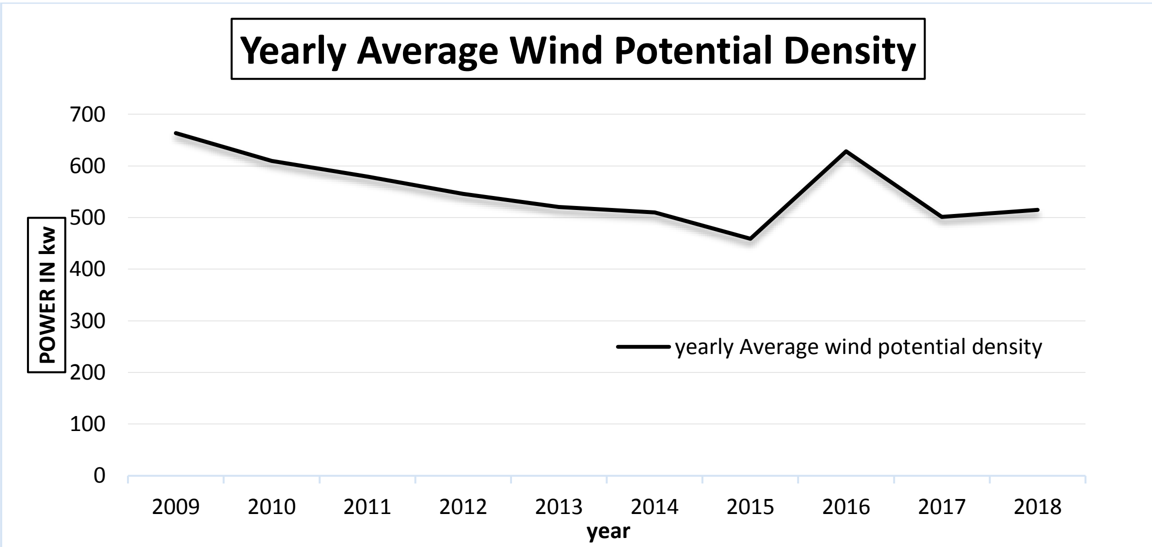

Figure 6.6 : Estimated Annual Wind power Density at Hub Height of 80m

The National renewable energy laboratory (NREL) categorize sites based on their average wind power density. Table 4 shows criteria's of the NREL for categorizing a site. The result of predicted wind power density of the studied site was at height of 80m therefore the result is extrapolated to a hub height of 50m. Employing that wind power density at 50m equals 490.64 w/m ^{2} .Therefore the site is classified under class four (GOOD) for wind farm.

Table 2. Classes of Wind Power Density (htlp://rredc.nrel.gov)

Wind power class	Resource potential	At 10 m		At 30 m		At 50 m	
		Speed (m/s)	Wind power density (W/m^2)	Speed (m/s)	Wind power density (W/m^2)	Speed (m/s)	Wind power density (W/m^2)
1	Poor	0 – 4.4	0 – 100	0 – 5.1	0 – 160	0 – 5.6	0 – 200
2	Marginal	4.4 – 5.1	100 – 150	5.1 -5.9	160 – 240	5.6 – 6.4	200 – 300
3	Moderate	5.1 – 5.6	150 – 200	5.9 – 6.5	240 – 320	6.4 – 7.0	300 – 400
4	Good	5.6 – 6.0	200 – 250	6.5 – 7.0	320 – 400	7.0 – 7.5	400 – 500
5	Excellent	6.0 – 6.4	250 – 300	7.0 – 7.4	400 – 480	7.5 – 8.0	500 – 600
6	Outstanding	6.4 – 7.0	300 – 400	7.4 – 8.2	480 – 640	8.0 – 8.8	600 – 800
7	Superb	7.0 – 9.4	400 – 1000	8.2 – 11	640 -1600	8.8 – 11.9	800 – 2000

6.2 Aerodynamic Characteristics of Baseline Blade

Aerodynamic characteristics of blade is essential to predict the extraction efficiency and flow phenomena. In this section the aerodynamic performance of the baseline (designed) blade is presented .The hereunder section present the result output of ANSYS FLUENT. The flow simulation was carried out at a Reynold number of $1.32x10^6$ utilizing LES; Hence LES has superb potential to analyze and capture flow separation.

6.2.1 Pressure contour and velocity streamline

Wind turbine blade experience different flow phenomena with respect to distinct flow conditions. Angle of attack and velocity are primary factor which influence aerodynamic forces and the flow behavior. In this thesis the designed blade flow phenomena is examined by varying the angle of attack from -10^0 to 25^0 at a constant Reynold number. The following plots pose pressure contour and velocity streamline along the designed blade; at selected AOA

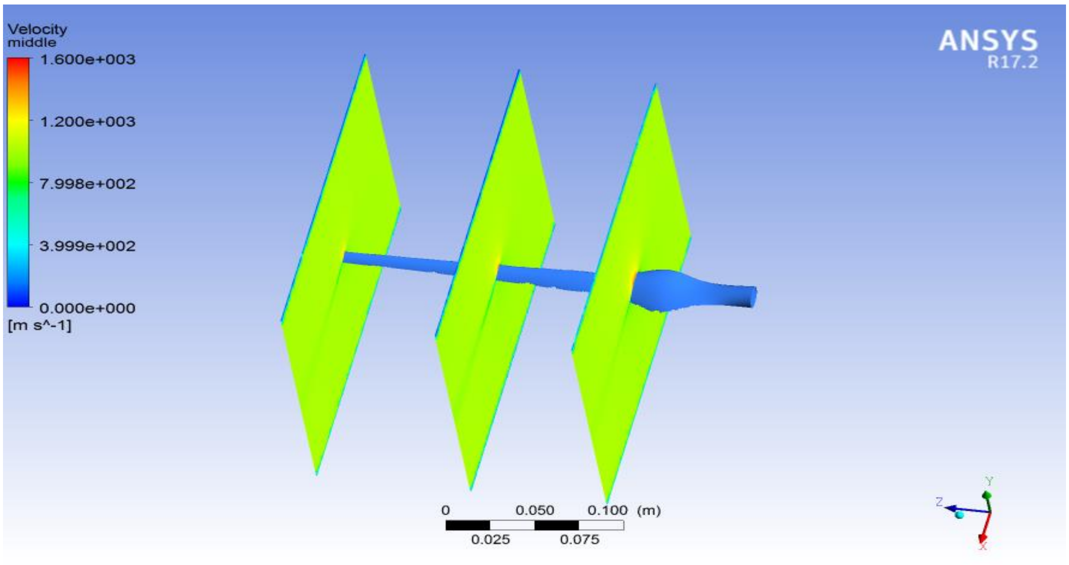

Figure 6.7 : Location of Tip, Mid and Root Section Velocity Contour

Figure (6.7) depicts three distinct contour capturing position (i.e. tip, mid & root), because of wind turbine blade have an angle of twist the fluid will also have different flow structure across the blade span.

6.2.1.1. At an Angle of Attack of (-5^0)

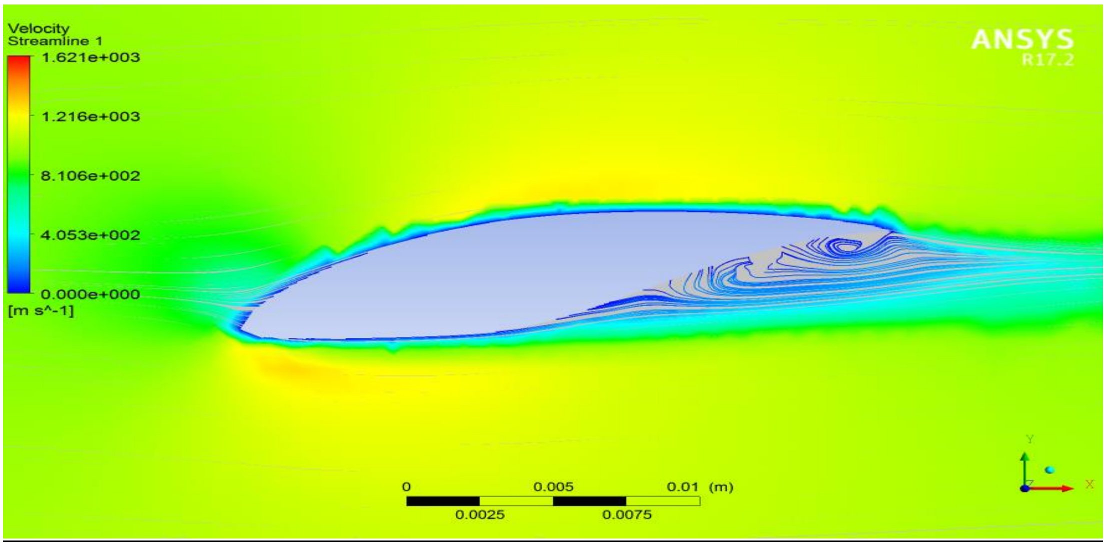

Figure 6.8 : Velocity Streamline At $\alpha = -5^0$

As its shown in Figure 6.8 at verylow angle of attack flow separation exist at pressure side of the blade,Hence the blade will have a low lift to drag ratio.The lift and Drag coefficent are -0.09 and 0.26 respectively which is minor

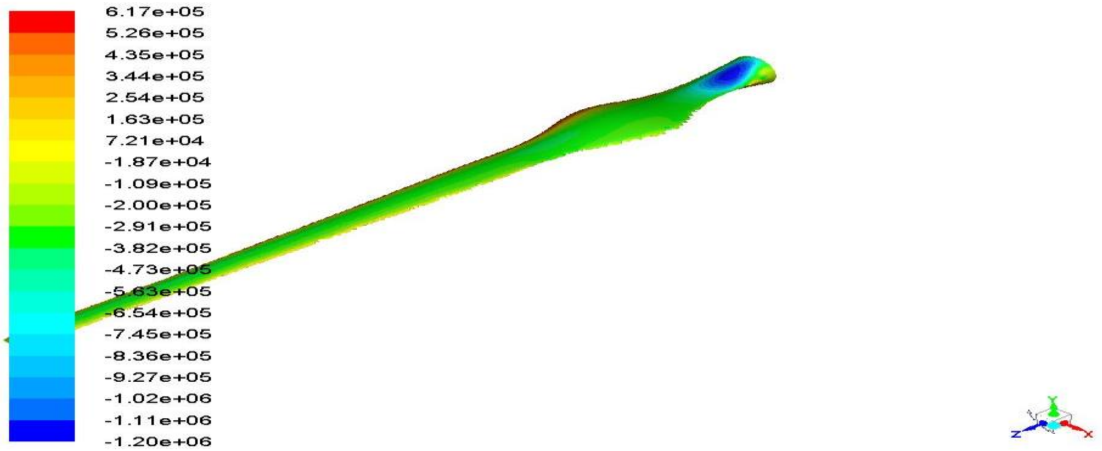

Figure 6.9 : Suction Side Pressure Contour At **$\alpha = -5^0$**

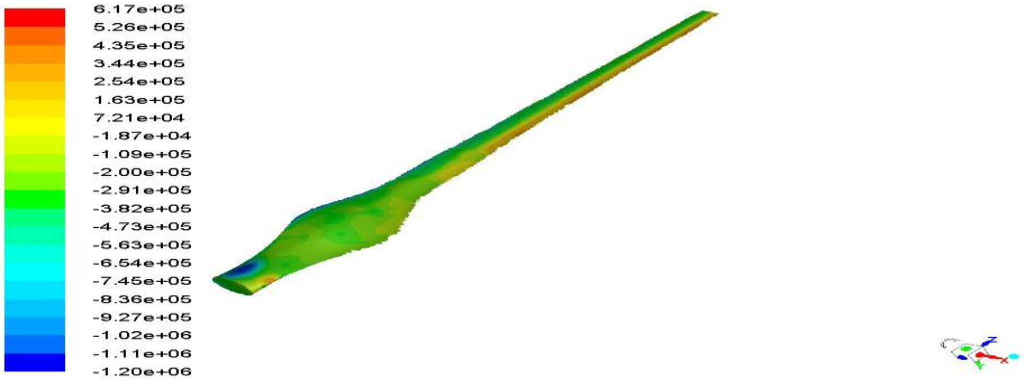

Figure 6.10 pressure Side Pressure Contour At **α= -5⁰**

At an Angle of Attack of (5^0)

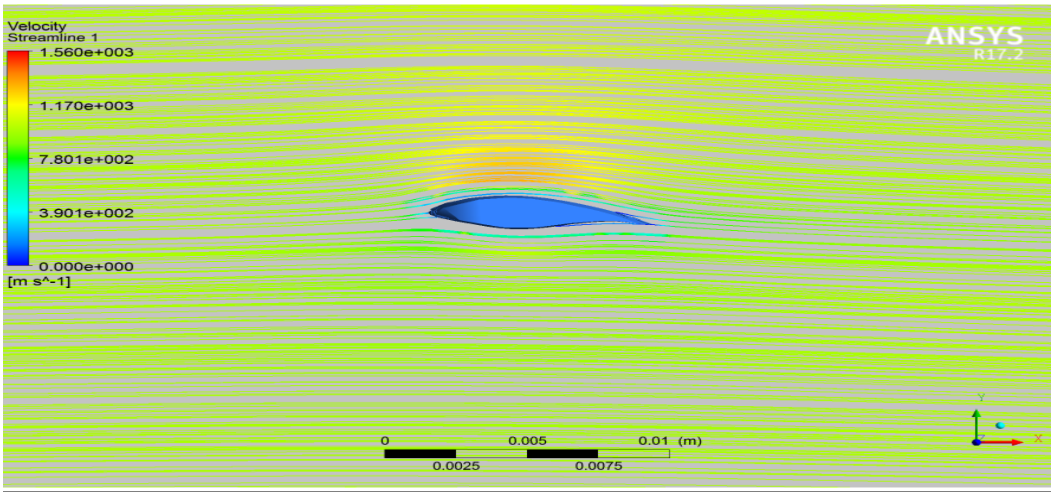

Figure 6.11 : Velocity Streamline At $\alpha = 5^0$

Figure 6.12 : Suction Side Pressure Contour At **$\alpha = 5^0$**

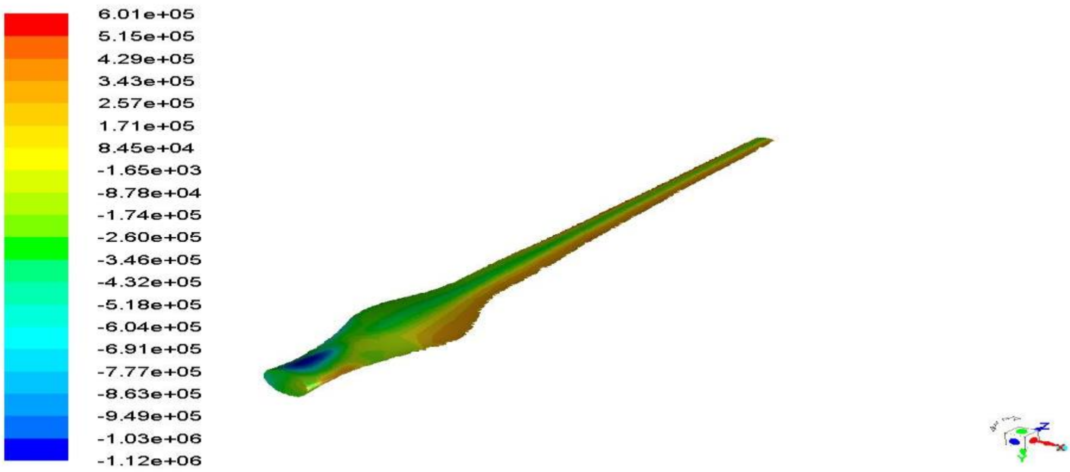

Figure 6.13 : Pressure-Side Pressure Contour At Mid-Section, **α= 5^{0}**

6.2.1.2. At an Angle of Attack of (10^{0})

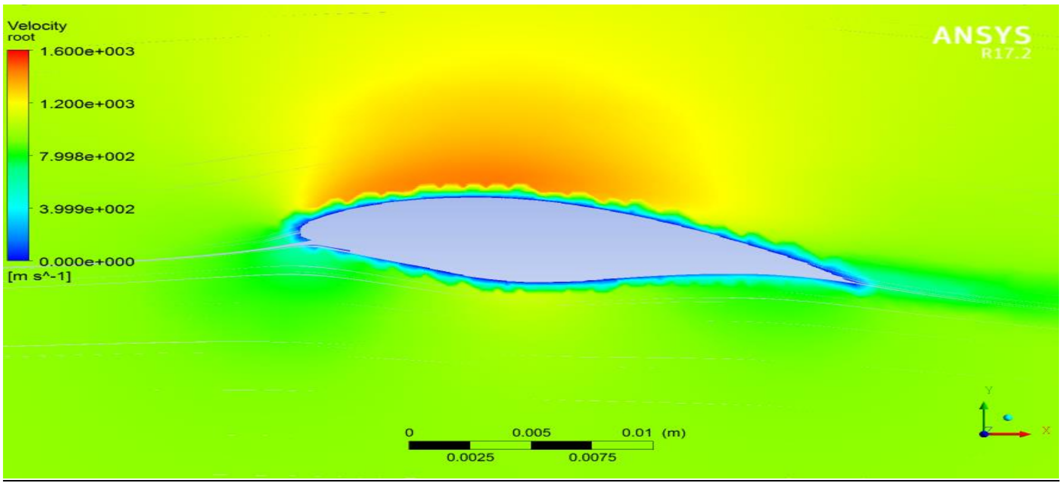

Figure 6.14 : Velocity Streamline at α = 10^{0}

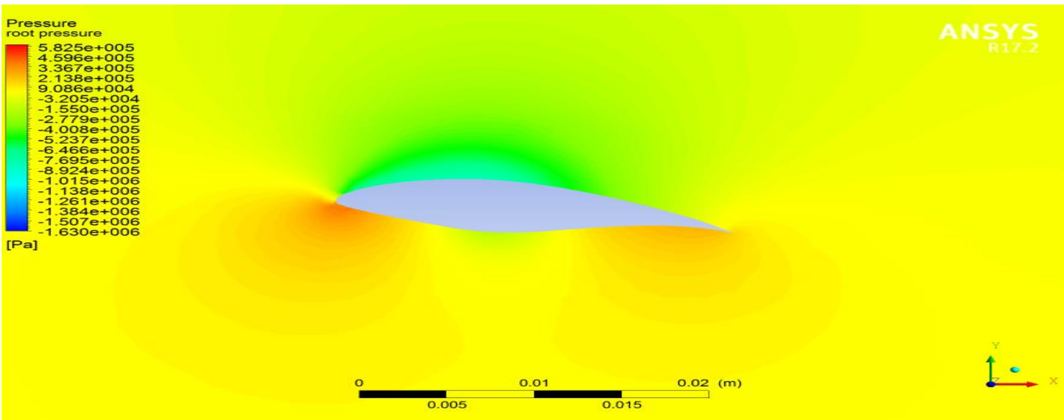

Figure 6.15 . Pressure Contour at Root Section on α = 10^{0}

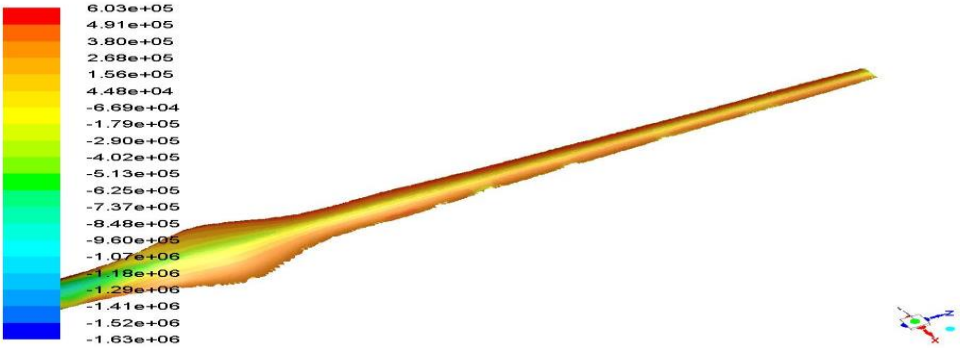

Figure 6.16 : Pressure-Side Pressure Contour At Mid-Section, **α= 10⁰**

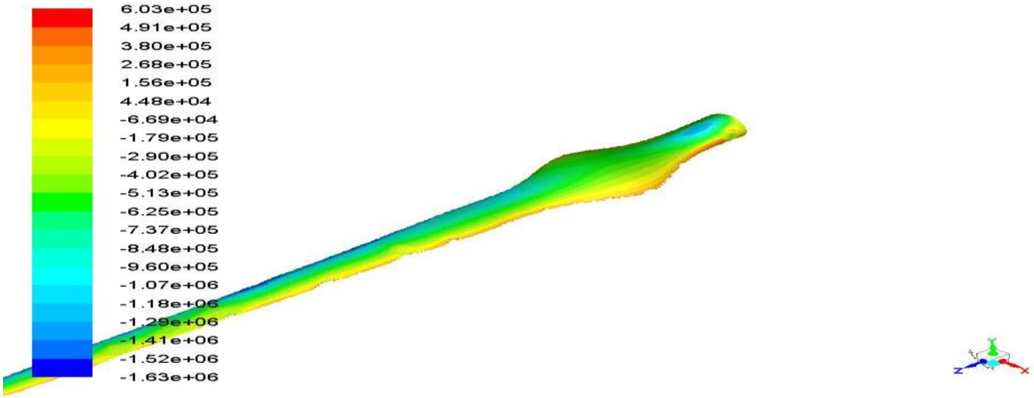

Figure 6.17: Suction Side Pressure Contour at Mid-Section, α= 10^0

In the above three figure the fluid streamlines at an angle of attack of 0^o, 5^o and 10^o are presented. As it's shown the fluid element reaching the leading edge reaches the trailing edge hence there is no flow separation. As a consequence of that the amount of lift force on the blade become high and Drag force is minimized. At **α=**10^o ratio of CFD result of lift force to drag force is 9.76 which is very good for wind turbine blades

6.2.1.3. At an Angle of Attack of (15^0)

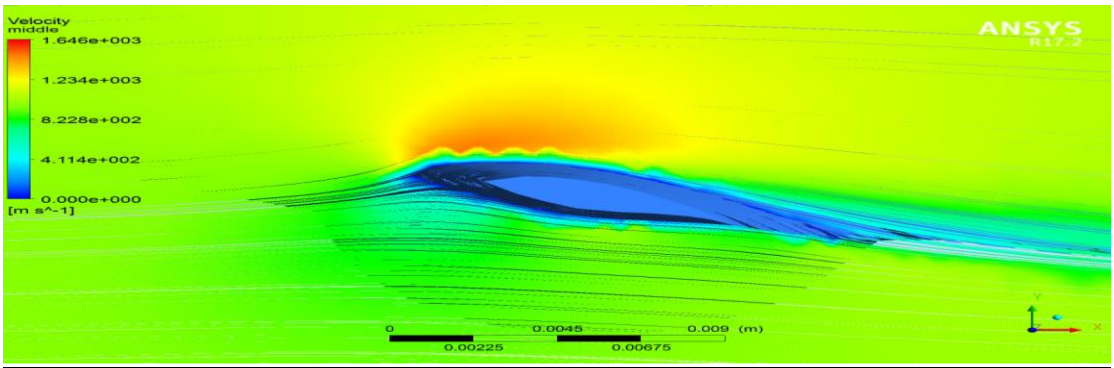

Figure 6.18 : Attached Flow at Mid-Section at α= 15^o

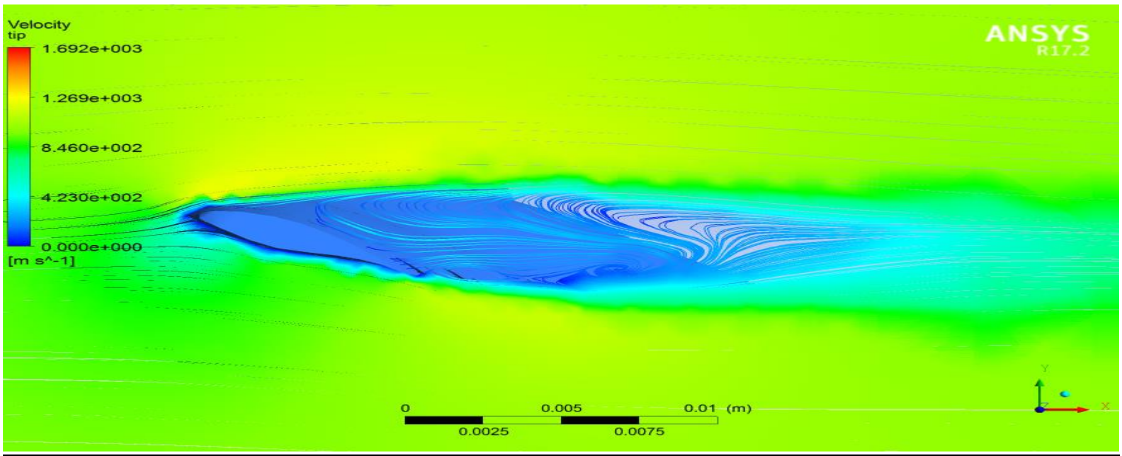

Figure 6.19 : Separated Flow at Tip-Section at α= 15°

6.2.1.3. At an Angle of Attack of (20^0)

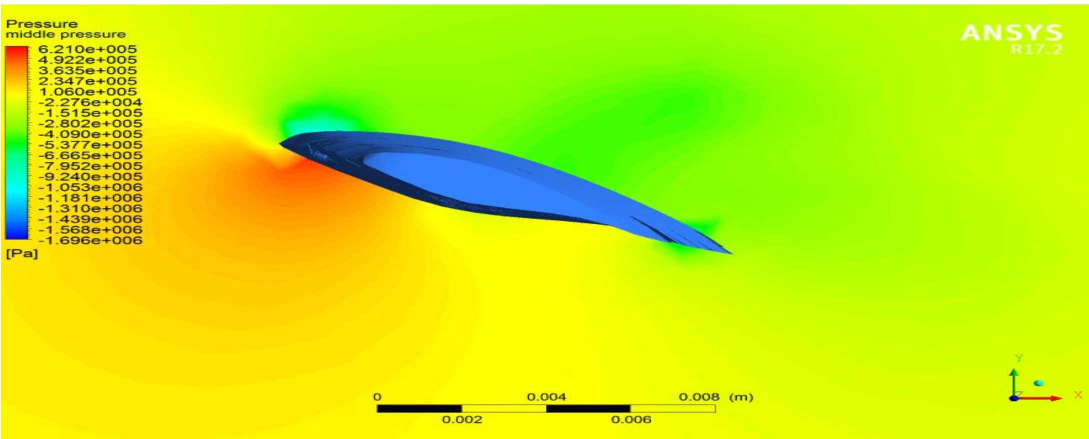

Figure 6.20 : Pressure Contour at Mid-Section, **α= 20^0**

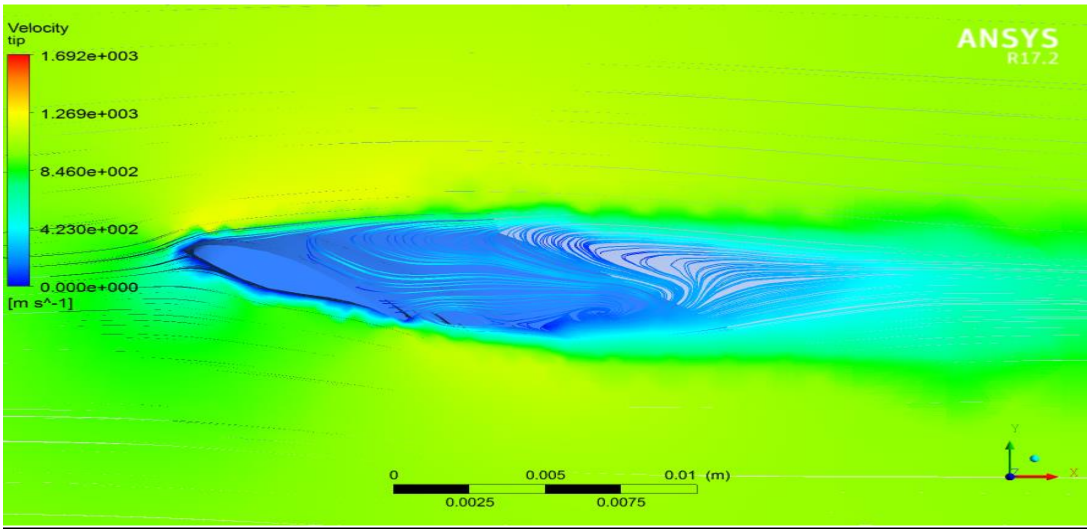

Figure 6.21 : Velocity Streamline At Mid-Section **α= 20^0**

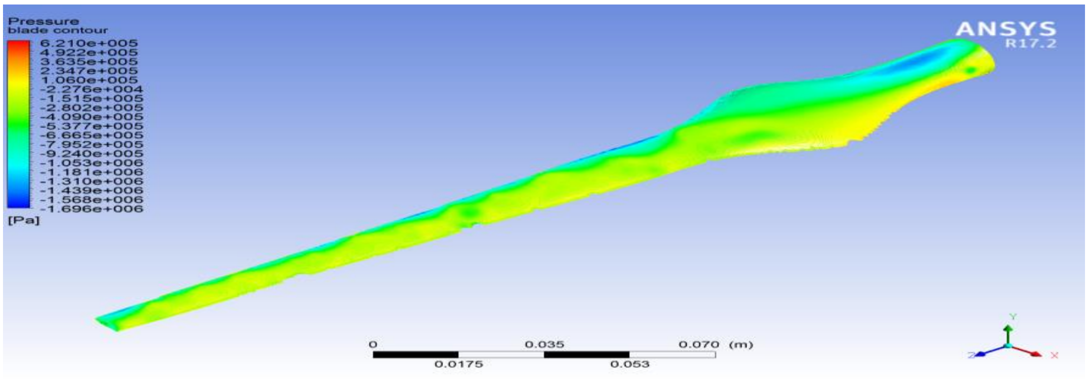

Figure 6.22 . Suction-Side Pressure Contour at Mid-Section, **α= 20⁰**

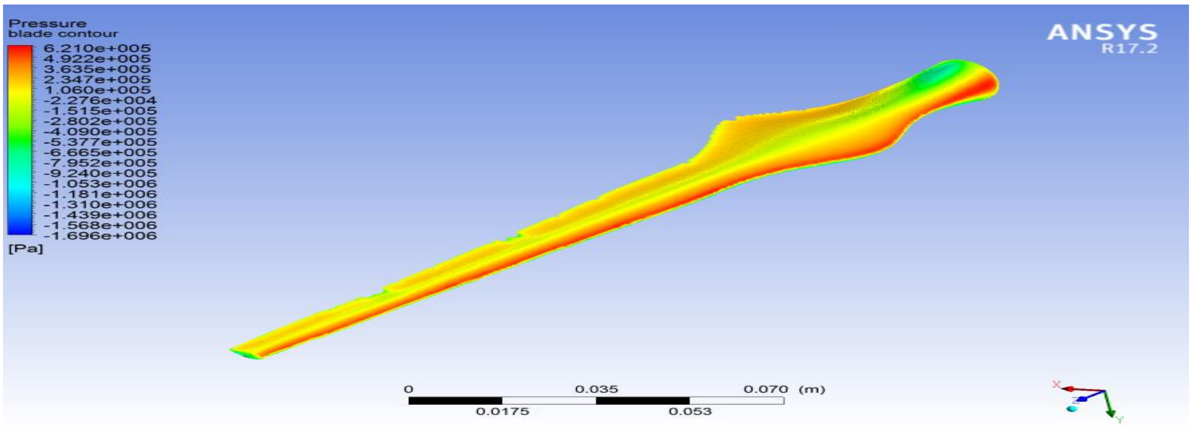

Figure 6.23 . Pressure-Side Pressure Contour At Mid-Section, **α= 20⁰**

6.2.1.4. At an Angle of Attack of (25⁰)

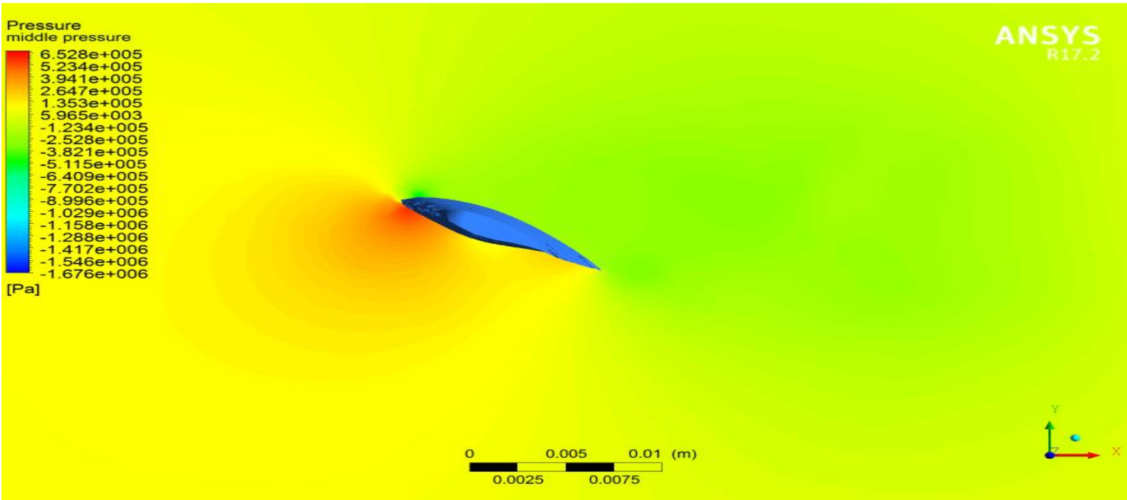

Figure 6.23 : Pressure Contour at Mid-Section, **α= 25⁰**

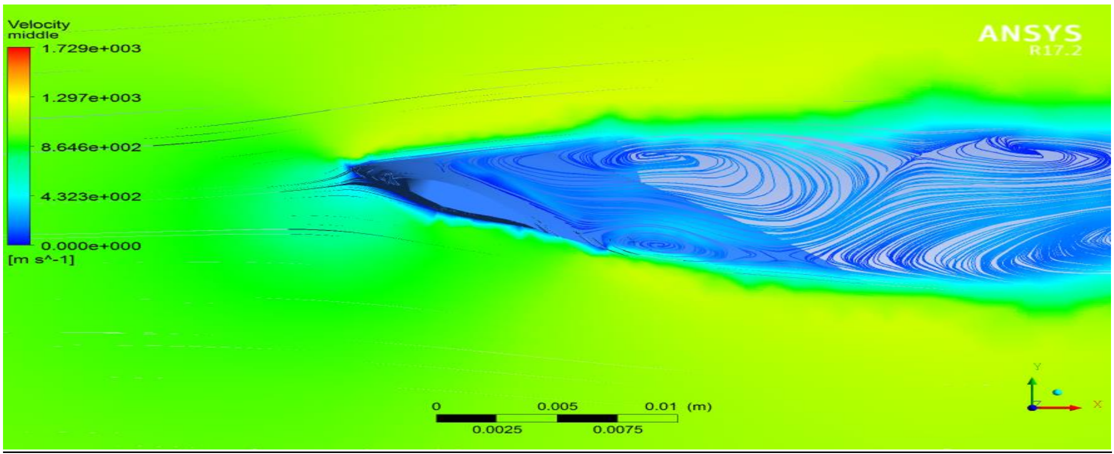

Figure 6.24 : Velocity Streamline At Mid-Section **α= 25^0**

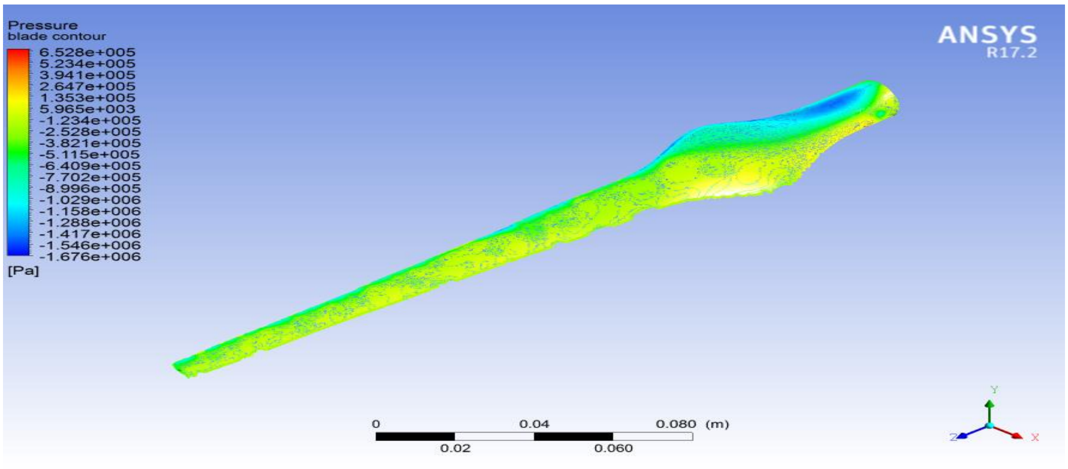

Figure 6.25 : Suction-Side Pressure Contour At Mid-Section, **α= 25^0**

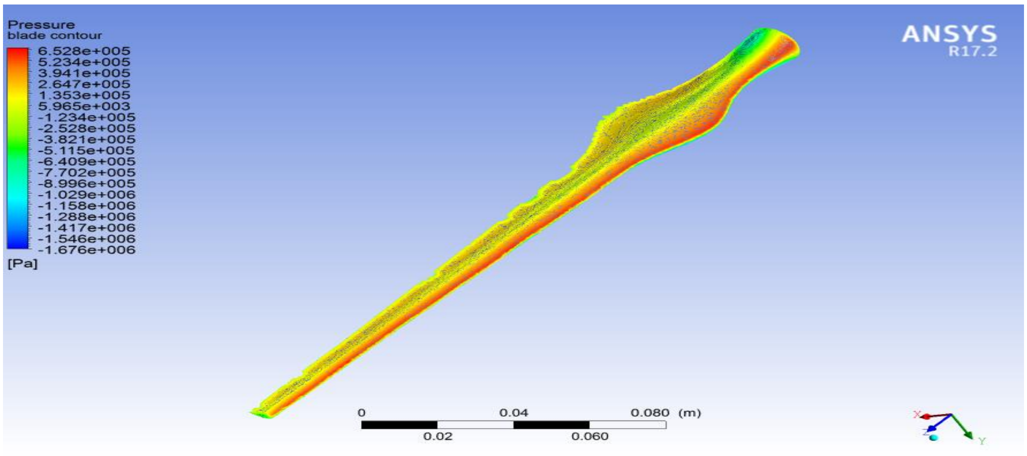

Figure 6.26 : Pressure-Side Pressure Contour At Mid-Section, **α= 25^0**

The flow phenomena at α=15^0, α=20^0 and α=25^0 is presented in the above velocity streamline figure (Figure 6.19, 6.21 and 6.24). The figures vividly shows the fluid element reaching the leading age will not reach at the trailing age; in situations of lower α values the fluid element adhere the surface starting from the leading edge to trailing edge .As the angle of attack of the blade is enhanced there is tendency of stall occurrence . for the baseline blade stall starts at an angle of attack of 15^0 around the tip section latter on if the angle of attack is further increased the stall will propagate throughout the blade and Eventually, no lift force will be generated

Aerodynamic performance of wind turbine, vehicle, aircraft, or any other device or component is examined by calculating the ratio of lift force to drag force .The lift coefficient and drag coefficient of the designed blade at different angle of attack is calculated using LES results. All The CFD result of the simulation are presented in the Appendix; based on those result the following graphs are plotted. These graph represent the lift coefficient, drag coefficient and aerodynamic performance of the baseline blade.

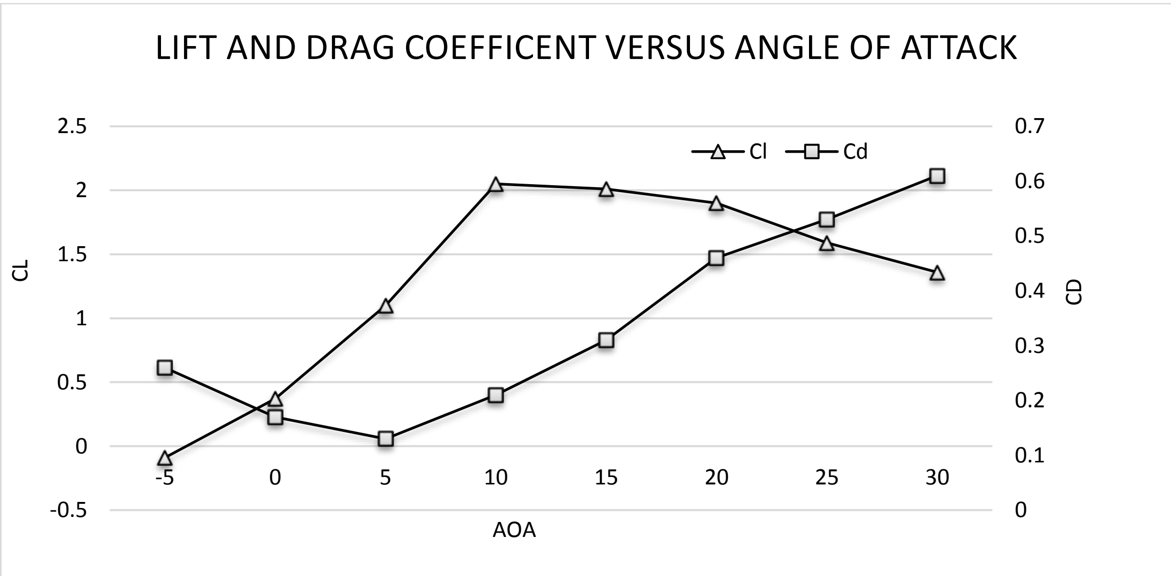

Figure 6.27 : Lift and Drag Coefficient versus AOA

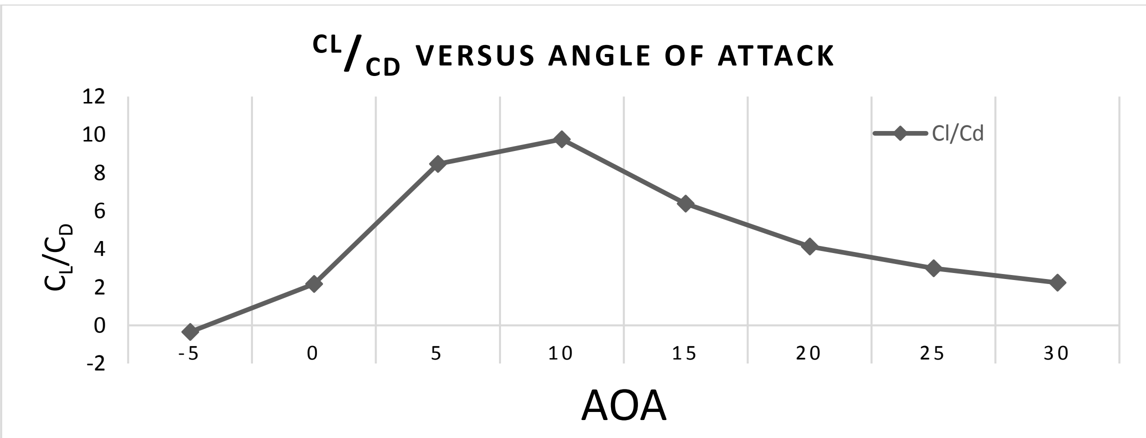

Figure 6.28 Aerodynamic Performance Versus AOA

As it is illustrated in the previous section flow separation on the designed wind turbine blade starts form angle of attack of 15^0. The above two figures also demonstrate the decrement of lift force and aerodynamic performance after AOA of 15^0 due to stall. Hence the designed wind turbine should operate with angle of attack range of 3^0 to 12^0.

6.2.2 Grid Independence Test

In section 4.2.3 the effect of the selected mesh size for the simulation were studied by varying the size of mesh. The hereunder graphs shows that both lift and drag coefficients are not dependent up on the selected mesh size.

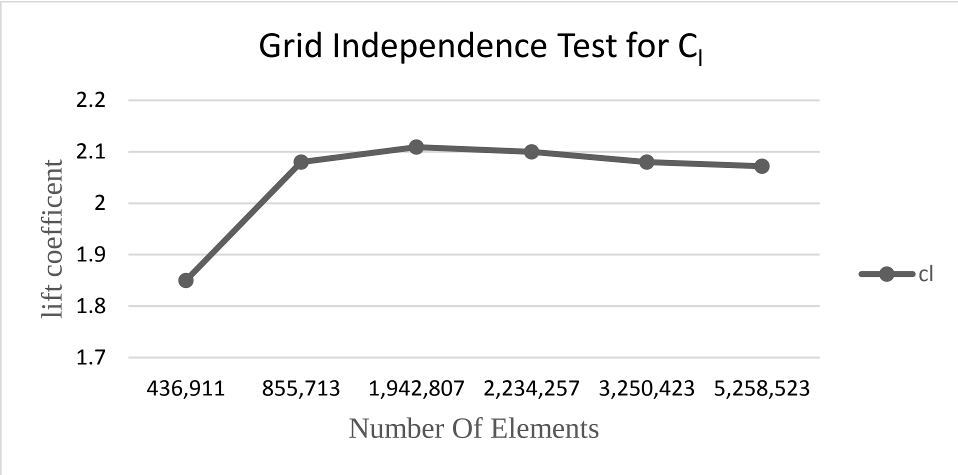

Figure 6.29 : Grid Independence Test Result for C_l

The lift and drag coefficient have little variation with variation of the number of elements. Hence the selected mesh size (1 mm) with number of element 1,942,807 is accurate enough to capture the flow phenomena.

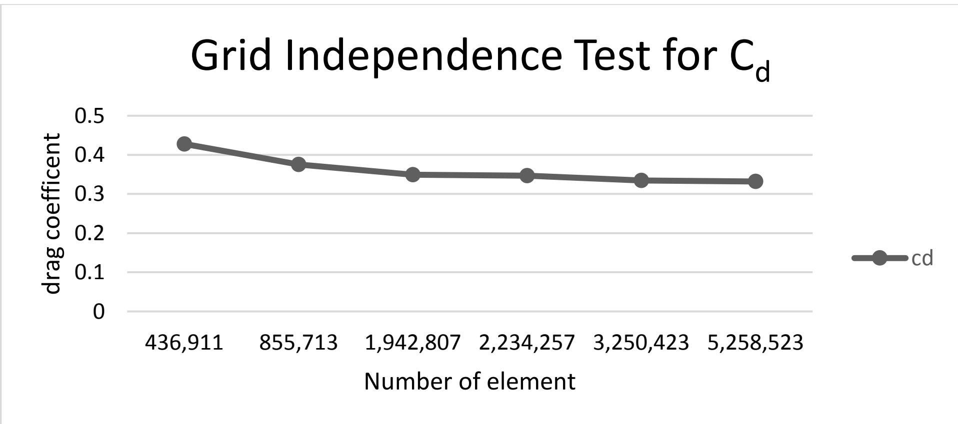

Figure 6.30: Grid Independence Test Result for C_d

6.2.3 Validation

CFD simulations are a very promising method for predicting the aerodynamic behavior of wind turbines in an inexpensive and accurate way. One of the major drawbacks of this method is the lack of validated models. For this thesis experimental result of small scaled S830 airfoil is used for validating the computional work.Similar computional fluid dynamics procedures, mesh type,mesh size and solution scheme is used for the scaled models CFD analysis. Figure 6.31 shows experiematal and CFD result of S830 airfoil at a Reynold number of 114,234. The results show that the variation of lift coefficent among the CFD analysis and expermental evaluation ranges between (7 up to 12) %,Therefore the mesh type,mesh size and the solution scheme of the CFD analyiss is good and acceptable.

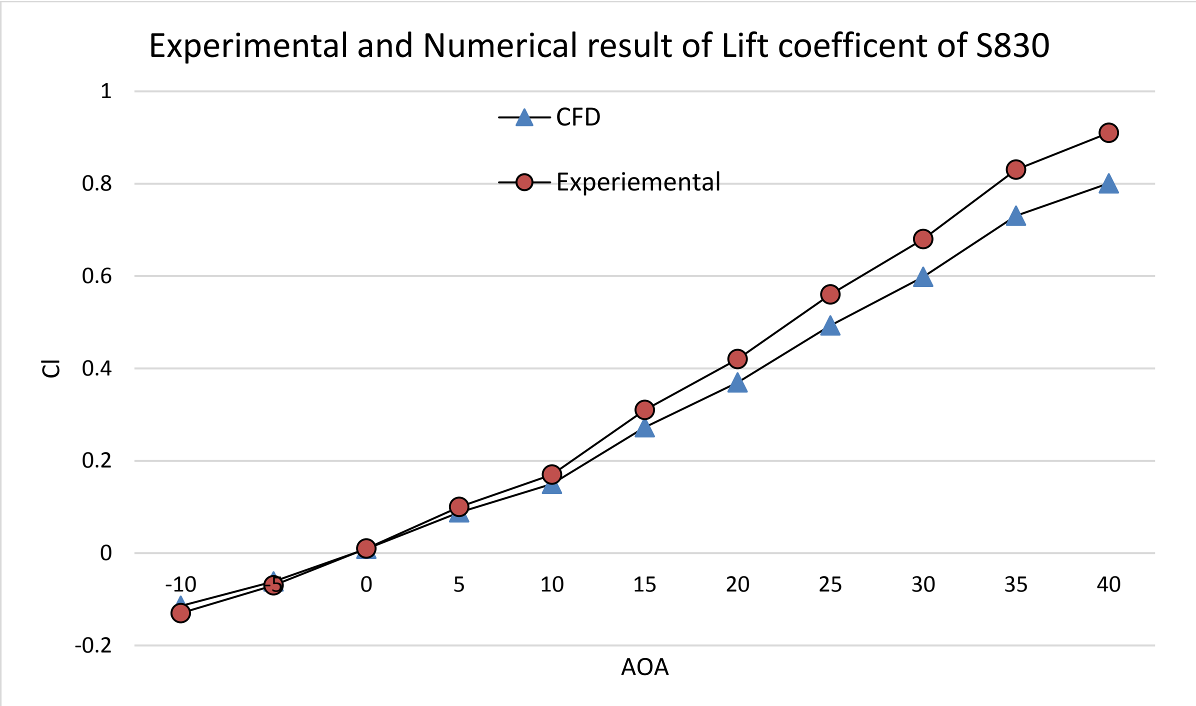

Figure 6.31 : Comparison of Experimental and Numerical Analysis result

6.3 Aerodynamic Characteristics of Blade with Dimples

In section 6.2 the aerodynamic characteristics of the designed blade were presented and the corresponding results shows that stall had mitigate the aerodynamic performance after an angle of attack of 15^0.In the hereunder portion the evaluation result of different dimple configuration for delaying flow separation is presented.

Six different dimple configuration were studied after a preliminary parametric study on dimple. Both inward and outward dimples were studied. In the first model fifty five outward dimples with a diameter of 10 cm at a chord length ratio of 0.5 were imparted. The result of model one explicate clearly that outward dimple will not delay flow separation rather they will induce additional drag force on the blade.

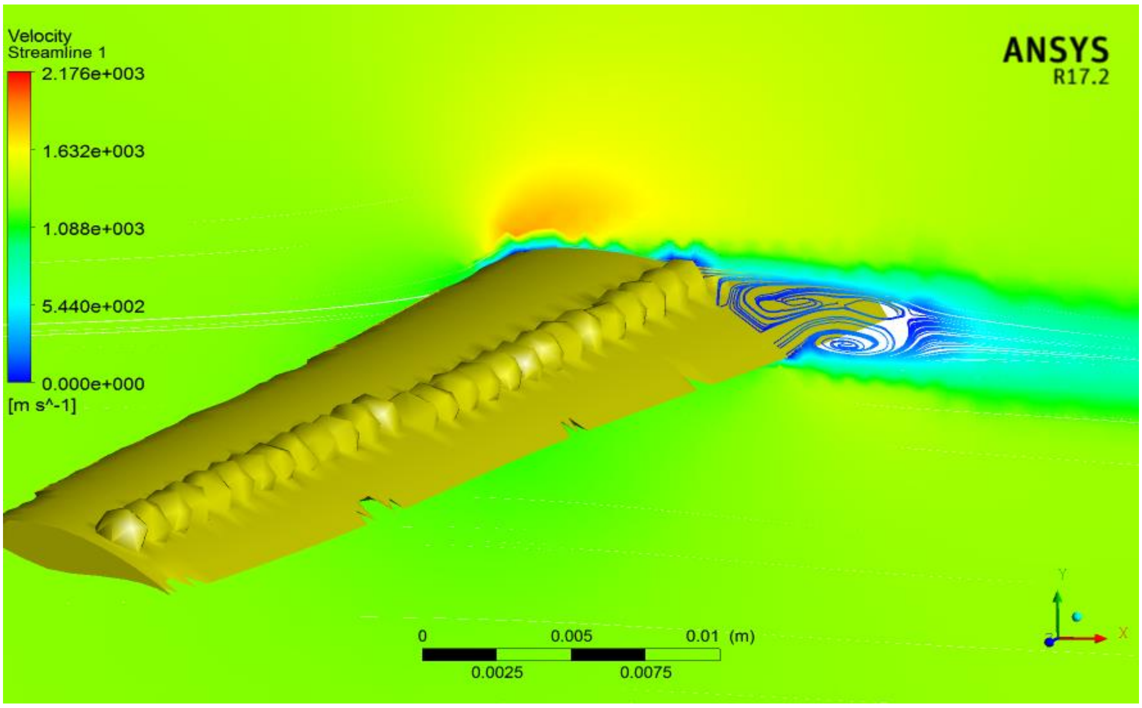

Figure 6.32 : Separated Flow At α=15^0 for CONFIG#1

The second dimple orientation consists of fifty eight inward dimple at half of the chord .The dimples were created with a diameter of 20 cm. The study results shows that this orientation have a very good result with respect to delaying flow separation. Consequently this dimple arrangement create a higher lift force than the baseline. In the figure below the velocity streamline at an angle of attack of 17^0 is presented. The figure vividly illustrate dimples configuration number two had created an attached flow on the flow field.

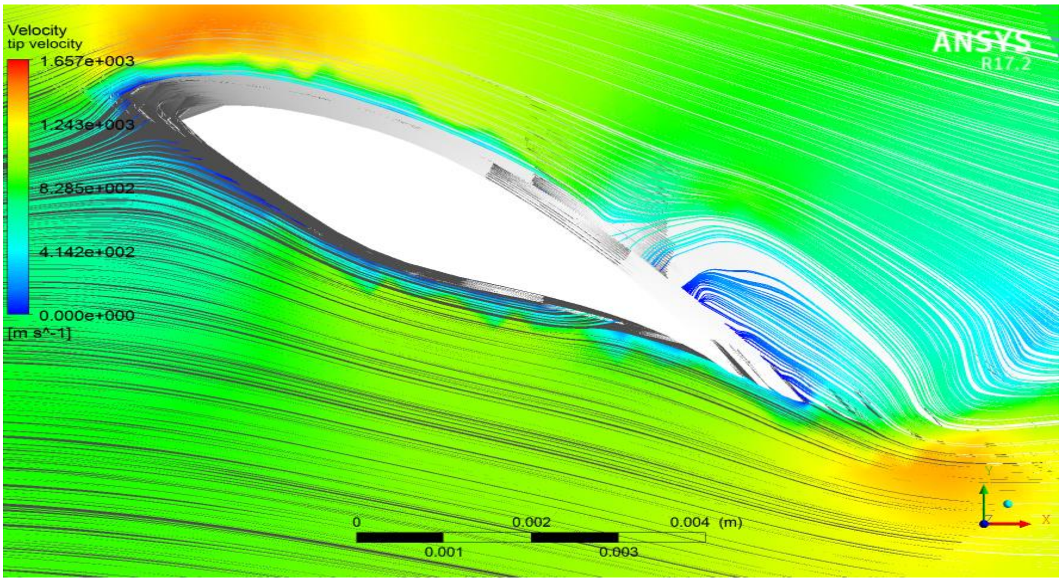

Figure 6.33 . Config#2 Velocity Streamline At α=17^0

The third and fourth configuration models have 5cm outward and 5 cm inward dimples respectively. The location of the dimple for both situations is at 0.4 of the chord length. The study on these dimple arrangement shows that both dimple orientation have enhanced the lift force with a small value, while Dimple orientation number five and six have a different aspect than the previous four situations.CONFIG#5 and CONFIG#6 have surface dimples on both the suction surface and pressure surface; the previous four studies were on dimples at the suction side (low pressure surface) of the blade.

The aerodynamic performance of the fifth and sixth dimple arrangement shows that configuration six possess good quality with regard to delaying flow separation while the fifth arrangement increase both the amount of drag and lift force .

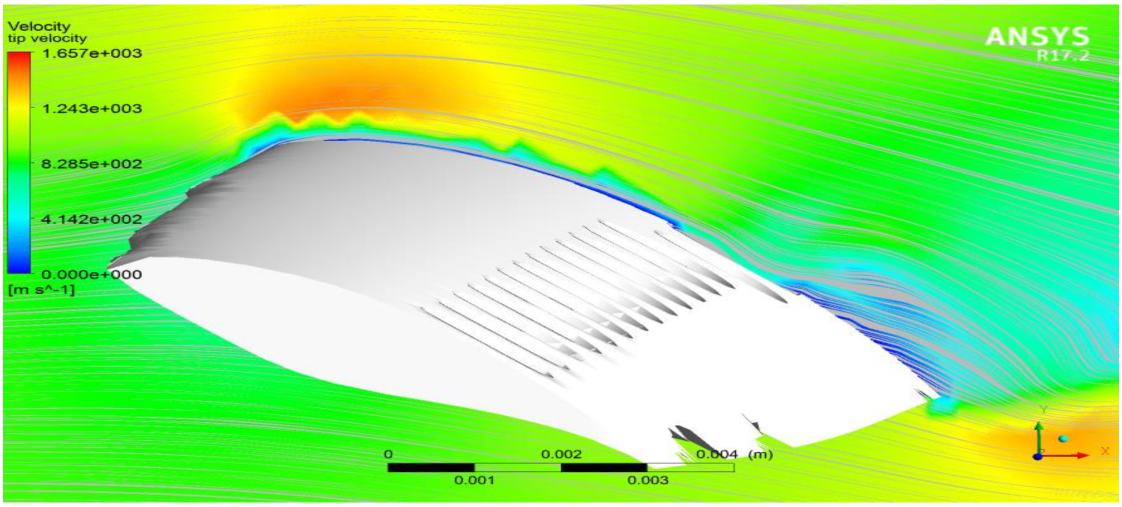

Figure 6.34 : Config#6 Velocity Streamline at α=20

Among these six different configuration of dimples; blade configuration number two and six showed a better result with regard to delaying flow separation. The next two figures shows the blade pressure contour at $\alpha=20^0$ for CONFIG# 2 and CONFIG#6.The legend of the contour shows that these two dimple arrangement have changed the amount of pressure force created along the blade. The baseline blade have a lower a pressure range between the pressure and suction surfaces.

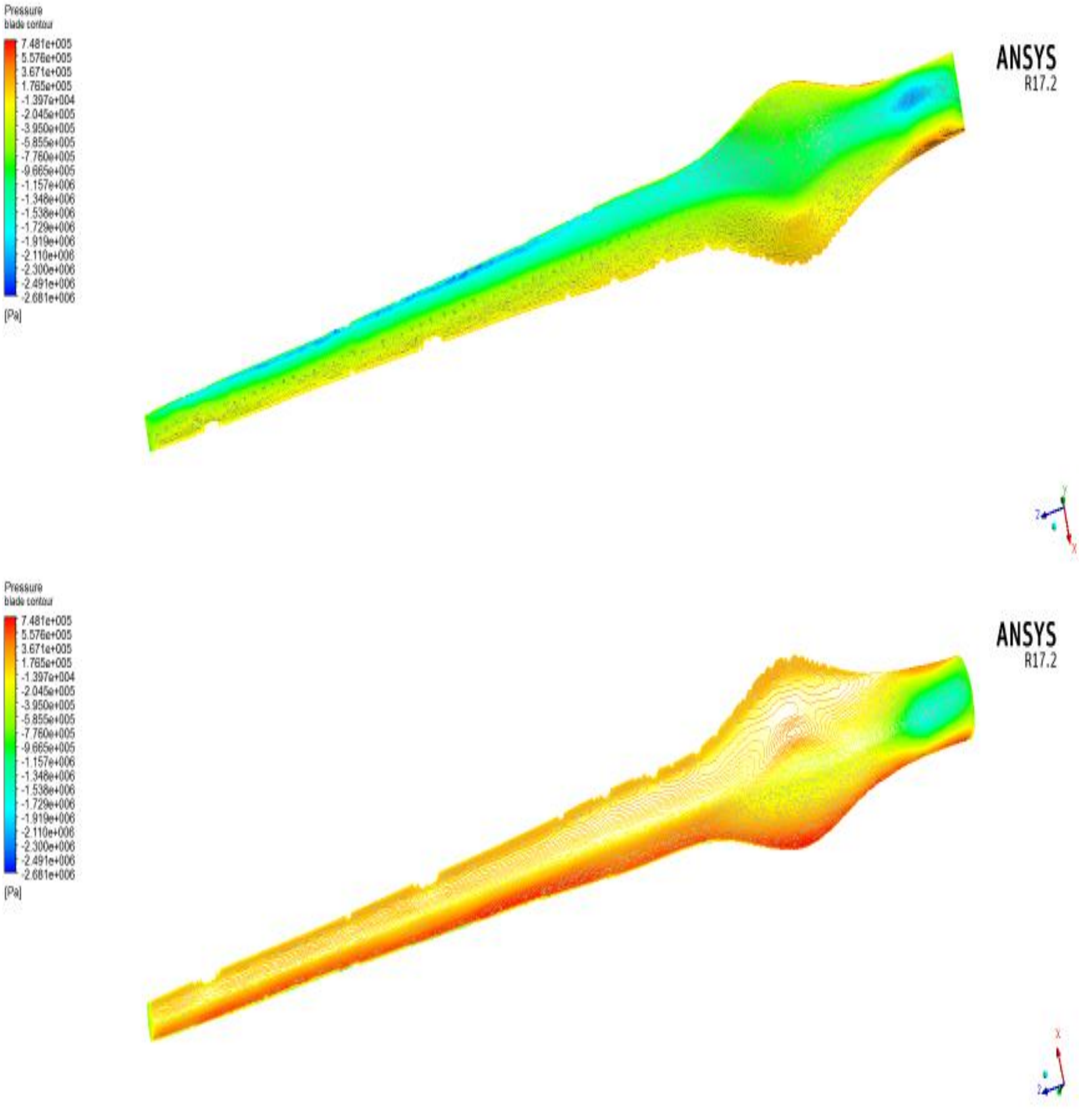

Figure 6.35 : Config#2 Pressure and Suction Side Pressure Contour

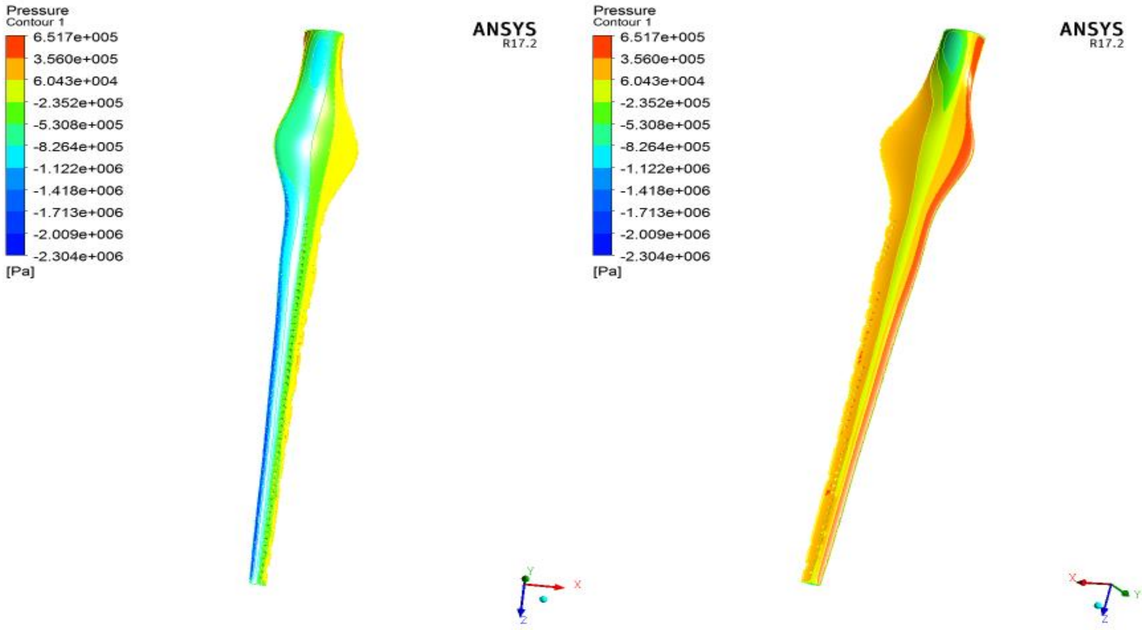

Figure 6.36 : Config#6 Pressure and Suction Side Pressure Contour

The amount of lift force is directly related with the flow separation or attachment. The lift and drag coefficient of wind turbine blade with the six distinct dimple arrangement plots for different angle of attack is presented in the Appendix(A-2); using these plots as an input the under lift coefficient comparison among the baseline blade and blade with different dimple configuration is made.

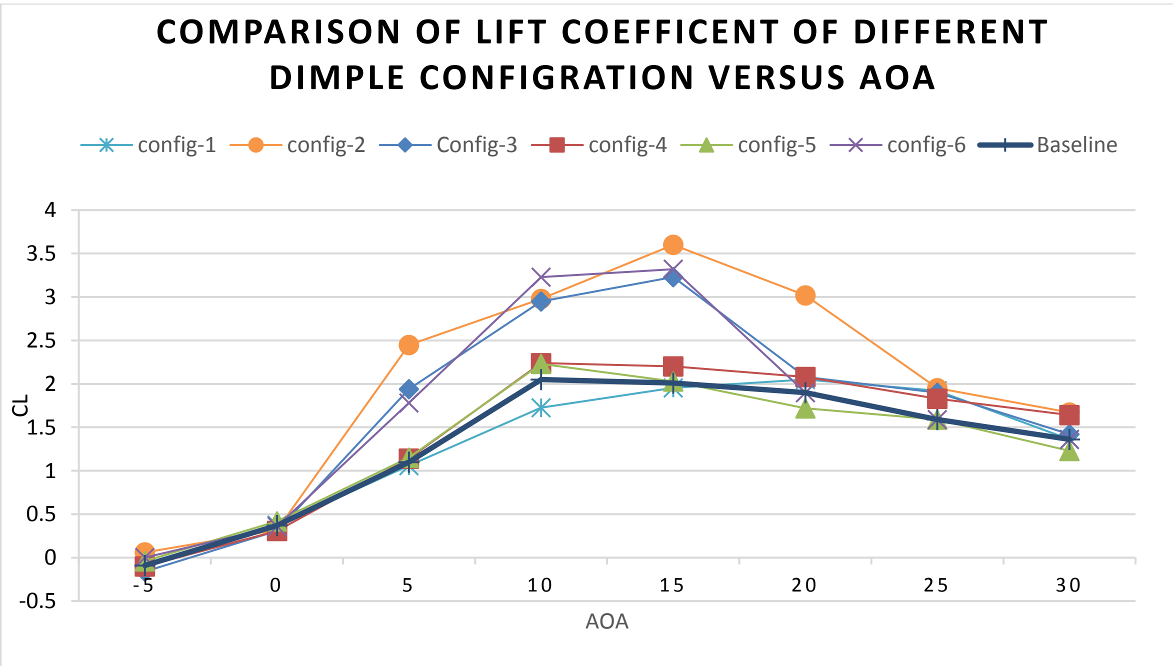

Figure 6.37 : Lift Coefficient of Baseline And Various Dimple Configuration

6.4 Performance Improvement on the Wind Turbine

Wind turbines' extraction efficiency is largely dependent up on the aerodynamic performance of the blade. In the previous sections the aerodynamic performance of the baseline blade and blade with different dimple configuration is presented. These result show that some dimple arrangement enhance the aerodynamic performance of a blade. In this section the effect of aerodynamic performance on the aggregate efficiency of wind turbine blade is analyzed and discussed

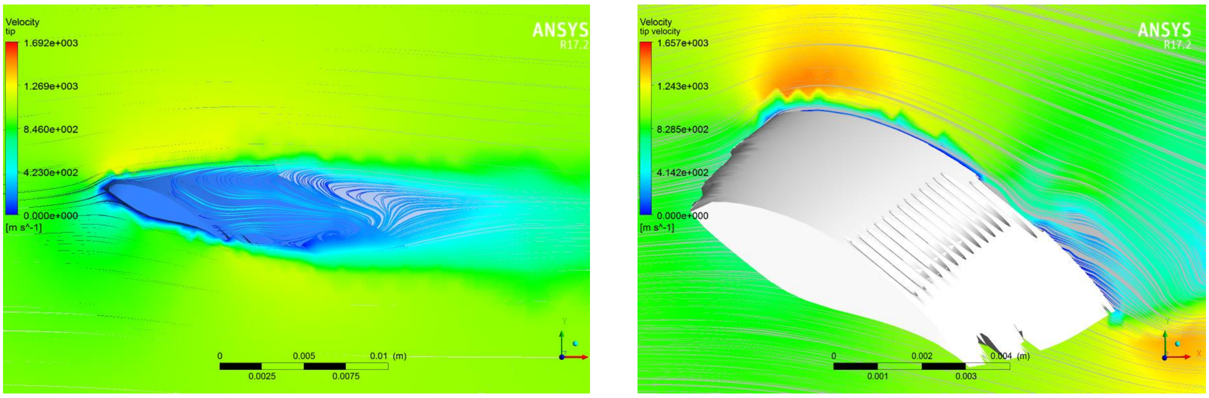

Figure 6.38 : Comparison of Flow Stream Line for Baseline Blade and Blade with Dimple

Aerodynamic performance is the ratio of lift force to drag force. The aerodynamic performance of the baseline and blade with dimple is analyzed and the hereunder result is found.

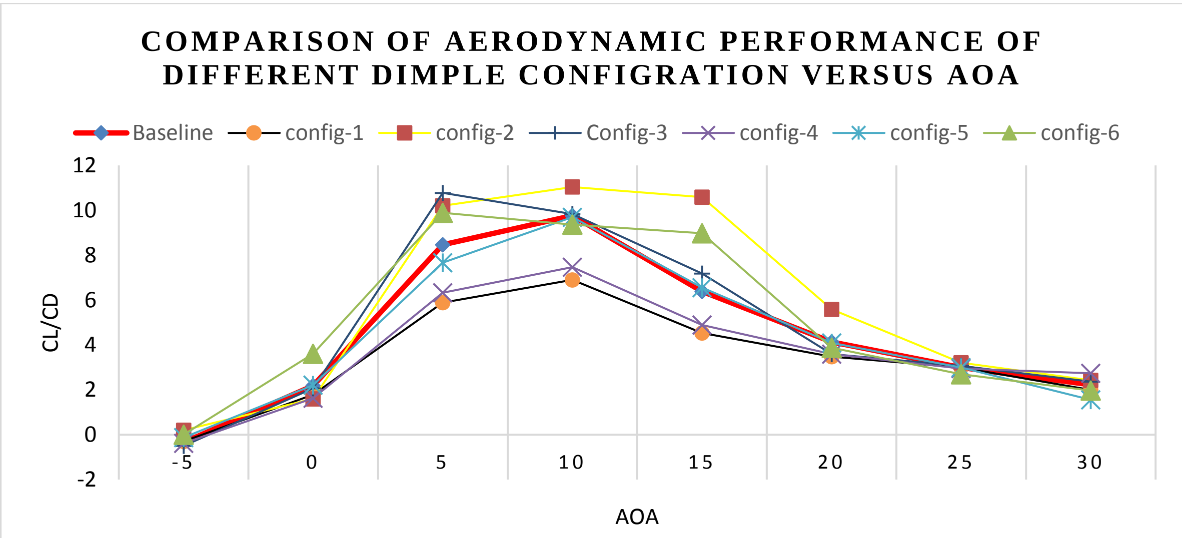

Figure 6.39 : Aerodynamic Performance of Baseline and Various Dimple Arrangement

Presuming if the designed wind turbine blade reaches the Betz limit the amount of power could be extracted is 1.2 MW. Nevertheless no wind turbine had ever reach this efficiency. The maximum amount of power coefficient of the designed turbine is presented in the figure below.CONFIG-2 wind turbine is preferred among the six different dimple configuration examined blades; by its higher aerodynamic performance. The power extraction coefficient of baseline and CONFIG#2 blade is analyzed by selecting number of blade as three and comparison among the power could be extracted is done. Using cetin correlation the amount of power extraction coefficient (C_p) for designed blade becomes 0.4181 and for wind turbine with CONFIG#2 blade have $C_p$value of 0.4467. (Peter, 2012).Using the corresponding C_p values, at a rated wind speed the amount of power could be extracted at the site is plotted for consecutive years starting from 2009 up to 2018.The baseline blade could extract an average power of 501.856 kW while CONFIG#2 blade can extract an average power of 535.7952 kW from 2009-2018.

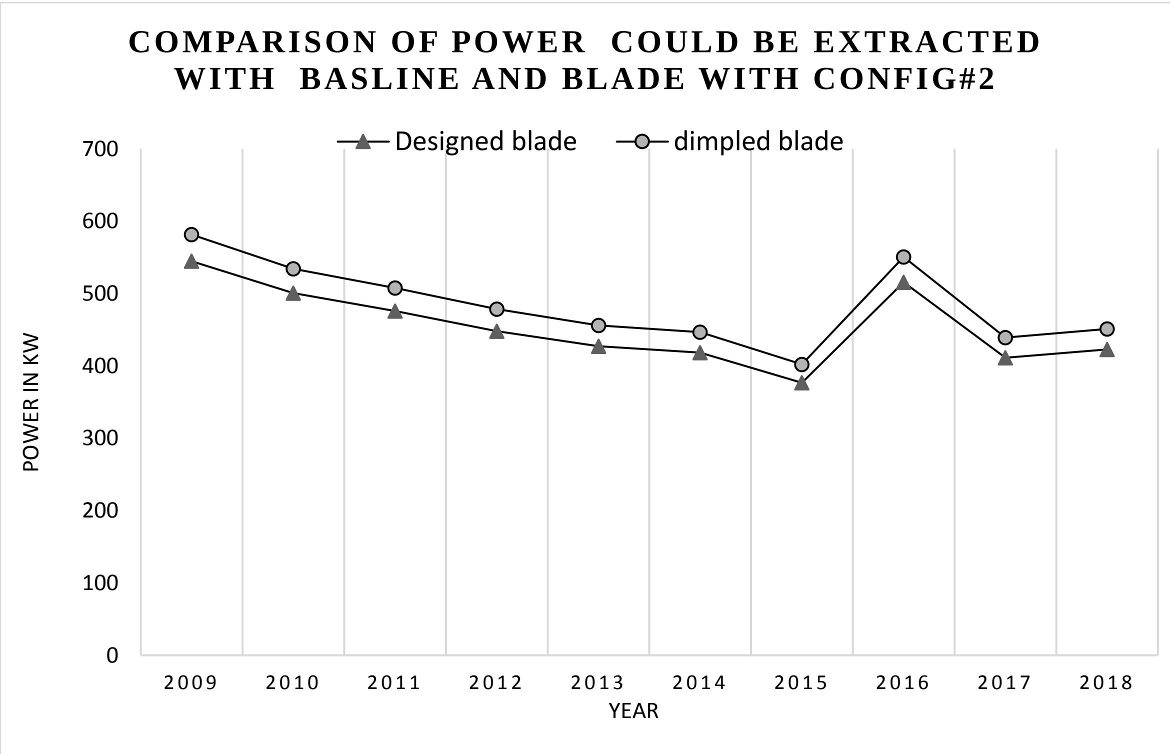

Figure 6.40 : Power Extracted By Baseline and Config#2 Dimpled Blade

6.5 Experimental Result

In addition to the CFD work the aerodynamic effect of dimple on wind turbine surface were examined by using a small scale 3D printed S830 wind turbine airfoil. Six different experiment by varying the wind speed is carried and the following results were found on each experiment.

The first test was done at wind speed of 8.4m/s the Reynold number of the test was 57,117.As it is proofed on the CFD Analysis the aerodynamic performance of the dimpled airfoil exhibit a better result than the baseline airfoil.

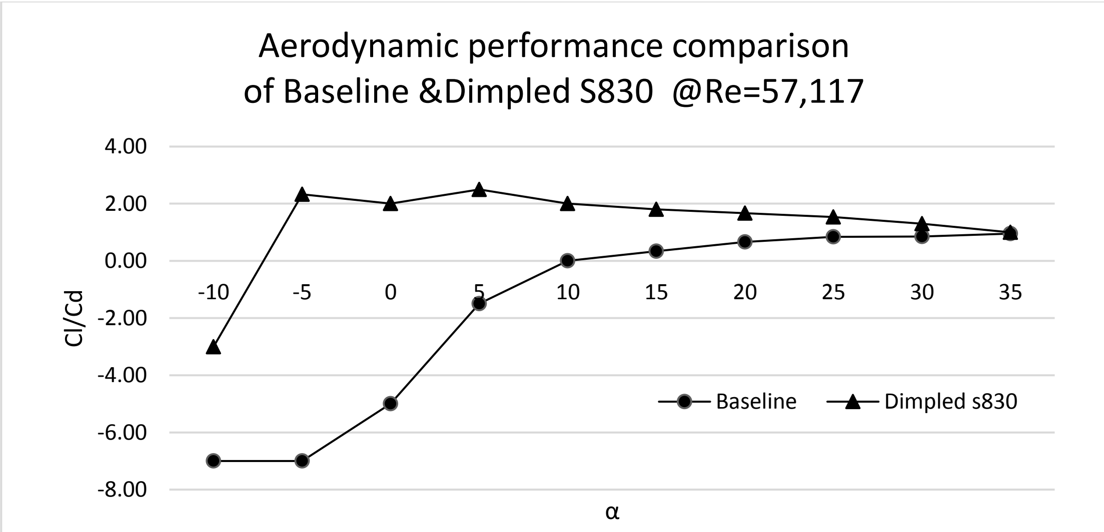

Figure 6.41 : Experiment One Result

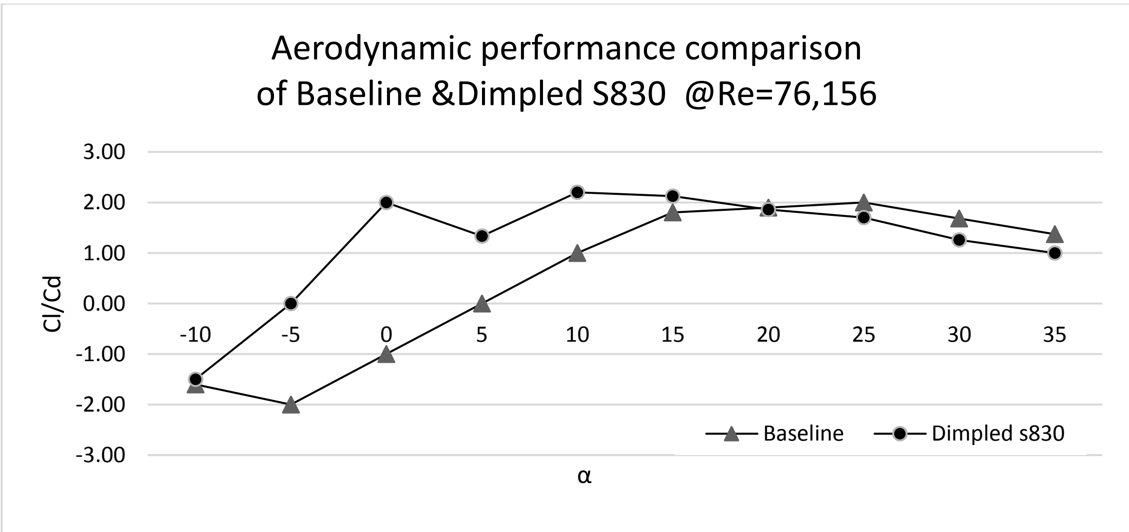

Figure 6.42 : Experiment two Result

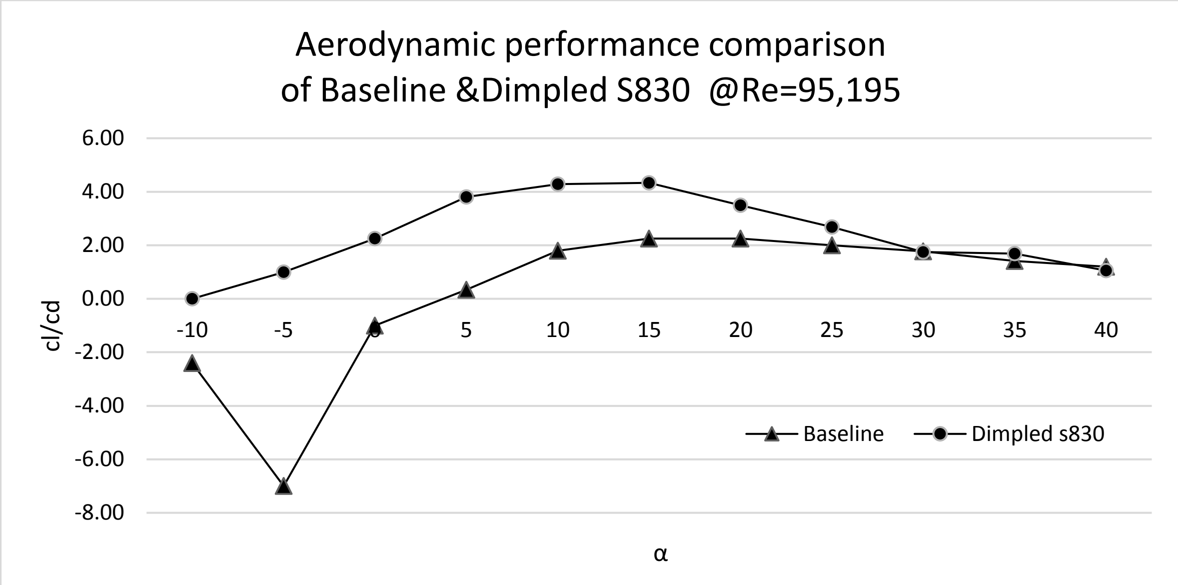

Figure 6.43 : Experiment Three Result

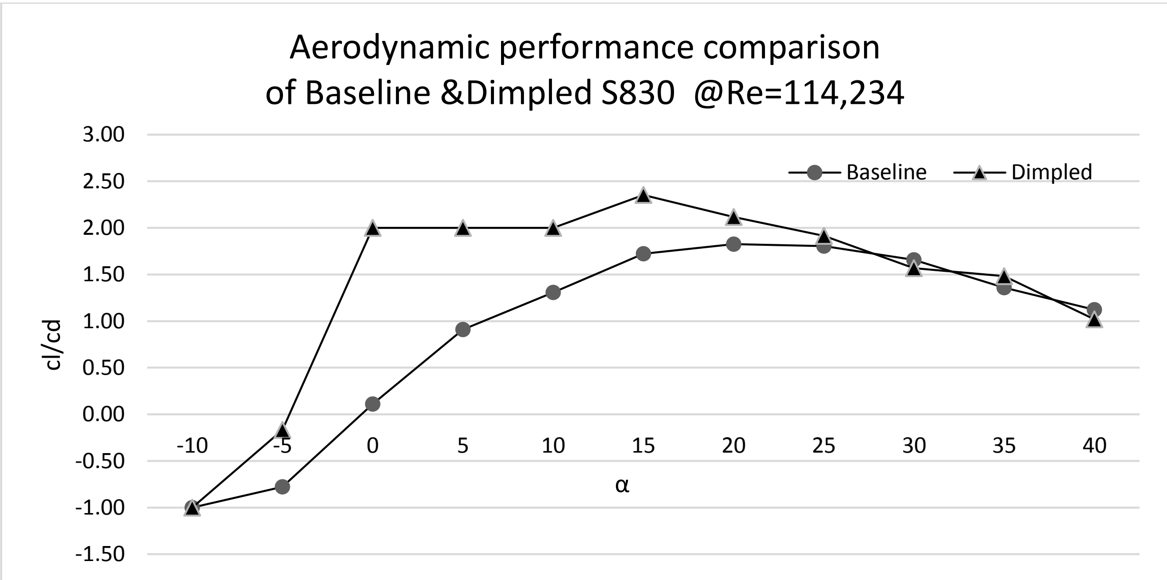

Figure 6.44 : Experiment Four Result

Test two, three and four were performed at wind speed of 11m/s,14m/s,16.8 m/s respectively. The result of these test is presented in figure 6.42, 6.43, and 6.44; which shows even for a higher Reynold number the aerodynamic effect of dimple for performance enhancement still sustained.

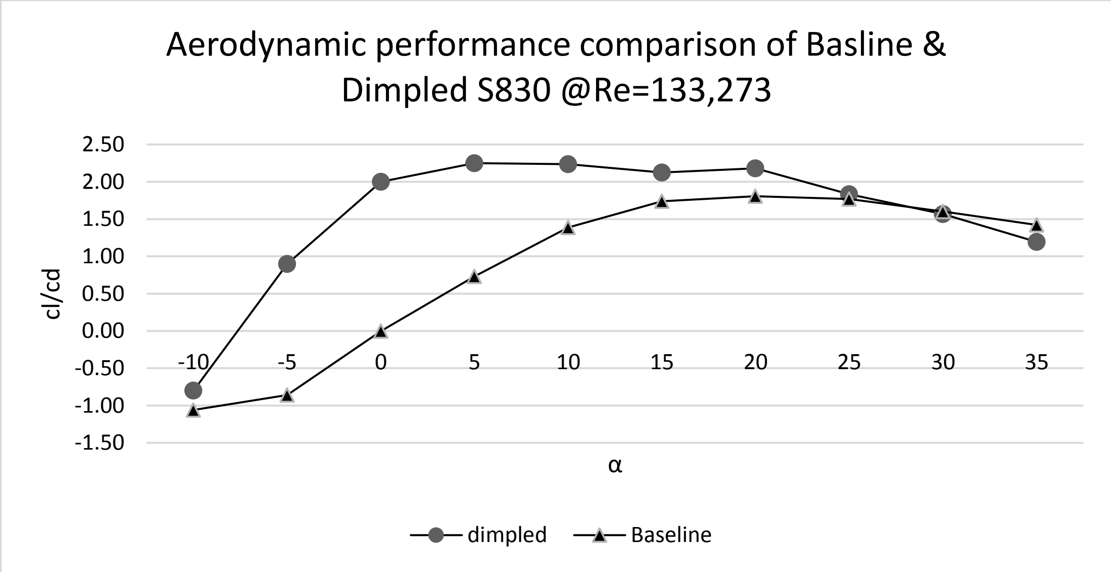

Figure 6.45 : Experiment Five Result

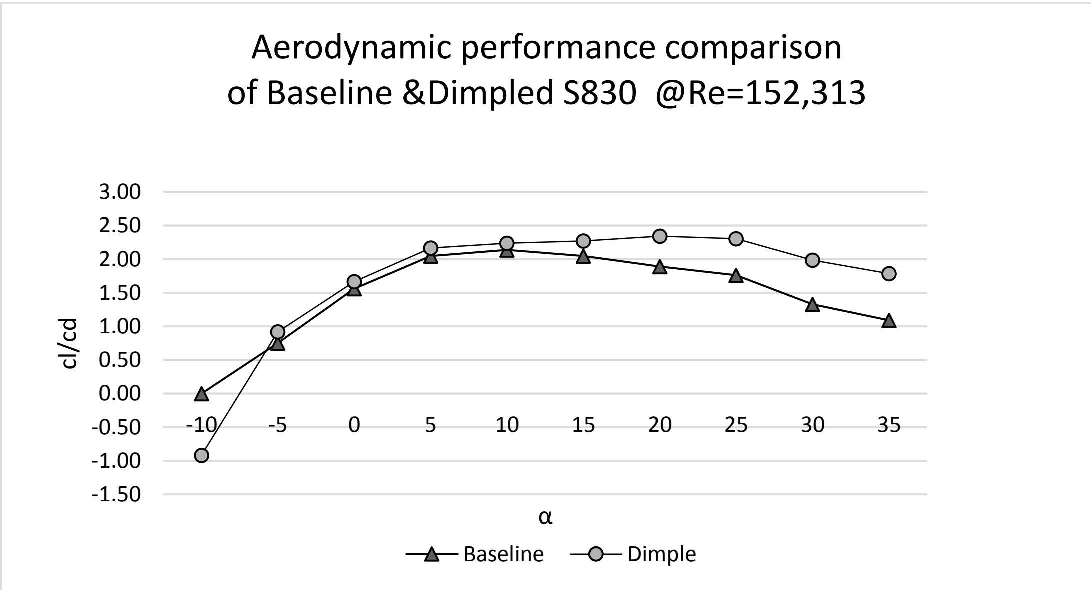

Figure 6.46 : Experiment Six Result

Eventually hence all tests reveal that surface dimple enhance the aerodynamic performance it's possible to say the computational fluid dynamics analysis results which claim dimples enhance aerodynamic performance is valid.

CHAPTER SEVEN

CONCLUSION AND RECOMMENDATIONS

7.1 Conclusion

This research had focused on the wind energy potential assessment of Eastern Ethiopia district named WETER, design of wind turbine blade and investigative work on the aerodynamic effect of dimples.

From these research results, the following conclusions can be drawn;

The mean wind speed ranges between 2.5m/s to 18m/s , monthly mean power density varies between 62.196 W/m^2 (*January*) and 2296.29 W/m^2 (*July*) at an altitude of 80m while the annual mean power density for ten years (2009 to 2018) varies between 458.96 W/m^2 and 663.63 W/m^2. Finally, WETER that is an onshore area, can be proposed as one of the favorable locations for wind turbines installation. Based up on site wind phenomena and BEM method HAWT blade is designed for cut in ,rated & cut off wind speed of 3m/s ,10m/s and 22 m/s respectively. The tip speed ratio of 6.8 and radius of 25 m was selected. NREL's airfoil S830 is selected for blade profile from aerodynamics performance comparison among different airfoils. The chord distribution from root to tip ranges between 3.39m to 0.77m, while angle of twist ranges from 31.139^o to – 3.73^o.

The aerodynamic performance of the designed blade was evaluated using LES. Maximum aerodynamics performance of the blade occur at an AOA of $12^{o.}$ Presuming if the designed wind turbine blade reaches the Betz limit the amount of power could be extracted is 1.2 MW. At angle of attack higher than 14^0 flow separation occur at pressure side of the baseline blade.This adverse phenomena will lessen the efficencey of the Turbine. Based up on the cetin correlation the power extraction coefficient of designed blade is found to be 0.41

Different Dimples size and configuration on the surface of designed blade were added and the aerodynamic performances were evaluated. Among the examined dimple configurations aerodynamic performance of config#2 (i.e. fifty-eight Inward dimple on the suction surface with a diameter of 10 cm at 0.4 chord length with 10 cm spacing between them) show a very good enhancement than others with a maximum reachable AOA of 17^0 . At a rated wind speed of 10 m/s; By using Cetin's correlation the power extraction coefficient of Config#2 were found to be 0.4415. The first model (Config#1) fifty five outward dimples with a diameter of 10 cm at a chord length ratio of 0.5 were imparted. The result of model one explicate clearly that outward dimple will not delay flow separation for wind turbine blades rather they will induce additional drag force on the blade; with maximum aerodynamic performance of 6.9 which is lesser than the baseline. The aerodynamic performance of Model six (10cm inward dimples at the suction surface and 5 cm inward dimple at the pressure side) enhanced the aerodynamic performance of the baseline blade to 9.93, while the remaining three configuration have small enhancement which is approach to 1 %.To validate the result of computational work on effect of dimples, experiment were carried out at small scaled S830 airfoil using subsonic wind tunnel. By varying the Reynold number six different experiments were done for both dimpled and Baseline models. The experiment result show that dimples will increase the aerodynamic performance by delaying flow separation.

Eventually, this study come across a conclusion of Eastern part of Ethiopia have a tremendous potential of wind energy; more specifically the site studied have an average power density of 610 w/m^2.Therefore the site is suitable for installing wind farm. Power extraction coefficient of wind turbine blade can be enhanced using inward dimples hence, the result shows that dimple will delay flow separation. In this study dimples extend the maximum reachable AOA before stall from 15^0 to 17^o; at a rated wind speed wind turbine blade with dimple have a 6.76% Increment on amount of power extracted than the baseline.

7.2 Recommendation for Future Works

- The selected site have a superb wind energy potential so the GOE should make further studies using a number of wind mast on the site and install a wind Farm .Hence this study is carried using wind data from Diredawa metrological station mast and satellite data.
- There are a lot of add-on device on aircraft to enhance the aerodynamic performance. For future work recommend to investigate those add-on device’s suitability for wind turbine blade.
- Investigation of Aeroacoustics and Aero elastic effect of Dimples on Wind turbine.
- Experimental work is carried using small scale S830 airfoil. The aerodynamic performance and dimple effect should be investigated on full scale wind turbine blade.

- LES is an accurate turbulence model to predict flow phenomena. Even though, Direct Numerical Simulation (DNS) have a better accuracy to predict turbulence. Recommend to future researcher to utilize this method if it’s accessible.
- Exergy analysis based on the second law of the thermodynamics can support to create the strategies and managements for more economical and effective use of energy sources. For future studies recommend to utilize Exergy analysis to study wind energy system.

REFERENCE

1. Arun K.K., Deepanshu K., Srivastav J. (2018). Analyzing the effect of dimples on wind turbine efficiency using CFD. *International Journal of Applied Engineering Research,* 13(6): pp. 4484-4489.
2. Abdoulkader I., Ramadan A. and Idris O. (2019).Wind energy potential and micro-turbine performance analysis in Djibouti-city, Djibouti. *Engineering Science and Technology*, V.51, pp.1245-1255.
3. Bharani R., Sivaprakasam A., (2019). A large volume wind data for renewable energy applications. *Data in brief*, V.25, pp.104291.
4. Belabes B., Youcef A., Guerri O., M. Djamai & A. Kaabeche (2015). Evaluation of wind energy potential and estimation of cost using wind turbines for electricity generation in north of Algeria. *Renewable and Sustainable Energy Reviews*. V.51, P.1245-1255.
5. Burger C. & Hartfield R. (2006). Wind turbine airfoil performance optimization using the vortex lattice method and genetic algorithm. 4th AIAA Energy Conversion Engineering Conference AIAA 2006-4051, 26-29.
6. Betz A. (1935) .*Applied Airfoil Theory: a general review of progress* Volume IV, Division 1st edition, McGraw-Hill.
7. Bechmann (2006). A Large-Eddy Simulation of atmospheric flow over complex terrain. Technical University of Denmark.
8. Booma D. , Tanjim A. & Rubiat M. (2016) ,Computational analysis of cavity effect over aircraft wing, *International Journal of Mechanical, Aerospace, Industrial, Mechatronic and Manufacturing Engineering*,V-10,Issue-4.
9. David F. Anderson & Scott Eberhardt (2001), Understanding Flight, 1st edition, McGraw-Hill.
10. Deepenshu Srivastav (2012). Flow control over airfoils using different shaped dimples. International Conference on Fluid Dynamics and Thermodynamics Technologies (FDTT) IPCSIT, Volume 33, IACSIT Press, Singapore, 2012.
11. Freudenreich T. M., & Brown R. E. (2002). Simulation of wind turbine wake interaction using the vorticity transport model. *Wind Energy*, 13, 587-602.
12. GTZ Wind Park Development (2006). Feasibility study for two wind parks development in Ethiopia. First Draft Report- Nazareth.

13. GTZ (2006). Feasibility study for wind park development in Ethiopia and capacity building, Ashegoda Wind Park Site, Final Report.
14. Harun Chowdhury (2016). A study of dimple characteristics on golf ball drag. *Procedia Engineering* 147 87 – 91.
15. Hansen and Butterfield C. (1993). Aerodynamics of horizontal-axis wind turbines. 1st edition, McGraw-Hill.
16. Haseeb S., Boorsma K., Kim C, and cho T., (2011).Analysis of detailed aerodynamics measure on a 4.5 m diameter rotor placed in the large German Dutch wind tunnel DNW. In proceedings of EWEA, Brussels, Belgium.
17. Josué Njock Libii (2006) Design of an experiment to test the effect of dimples on the magnitude of the drag force on a golf ball, World Transactions on Engineering and Technology Education Vol.5, No.3.
18. Jonkman, J., Butterfield, S., Musial, W., & Scott, G. (2009). Definition of a 5-MW Reference Wind Turbine for Offshore Development. National Renewable Energy Laboratory.
19. Jason R. Gregg, (2011), "Design and Experimental Testing of Small-Scale Wind Turbines", Baylor University.
20. Jones W. and Launder B. (1972), The prediction of laminarization with a two-equation model of turbulence. *International Journal of Heat and Mass Transfer*. 15(2):301–314.
21. Kalogirou S.A., (2014) - Wind Energy Systems: Renewable Energy Engineering (Second Edition), Academic Press, Boston, 735-762.
22. Kasahun Gashu, (2014). Design of small scale wind turbine blade for rural villages' electrification .Addis Ababa University Press.
23. Lilly D. (1966). On the application of the eddy viscosity concept in the inertial subrange of turbulence. *Near. Manuscript* 123.
24. Livya. E, Anitha. G, Valli. P,(2015) Aerodynamic analysis of dimple effect over aircraft wing, *International journal of mechanical aerospace industrial and mechatronics engineerin*g, Volume 9. Number 2, Pages 350-353
25. Liaquat Ali (2013) Wind potential assessment and optimization of wind turbine blade for coastal area of Jiwani, Pakistan. *International Journal of Materials, Mechanics and Manufacturing*, Vol. 1, No. 2.

26. Mengesha Wudu (2015).Wind energy resource analysis: A situation study of Aysha wind farm. Addis Ababa University Press
27. Makridis A, Chick J. (2013) Validation of a CFD model of wind turbine wakes with terrain effects. *Journal of Wind Engineering and Industrial Aerodynamics*. 123, PartA
28. Mahu R. and Popescu F. (2011) NREL Phase VI Rotor Modeling and Simulation Using ANSYS Fluent 12.1. Mathematical Modeling in Civil Engineering. P.185–194
29. Menter Fr. (1993) Zonal Two-Equation K-Ω Models For Aerodynamic flows. Aiaa.1993 ;(93-2906).
30. Makridis A, Chick J. CFD (2009) modeling of the wake interactions of two wind turbines on a gaussian hill. In: Eacwe 5. P. 9.
31. Mulugeta Biadgo, (2009), "Computer-aided aerodynamic and structural design of horizontal- axis wind turbine blades", AAU.
32. MOFAOD, Ministry Of Foreign Affairs of Denmark (2016), Accelerating Wind Power Generation in Ethiopia. Thematic Programme Document
33. Moses D., Sitzki L, and Hahm T. (2016), CFD study on aerodynamic effects of dimples on aircraft wings, *International Journal of Engineering & Science Research*, Volume-6, Issue-11, Pages pp.245-248.
34. Nikolai N., Guðrún P. , Halldór B. , Andrea N. Hahmann (2014), The wind energy potential of Iceland. Renewable Energy 69 290-299
35. Ozgur M. (2006) Assessment of the Wind Energy Potential of Kutahya, Turkey. *Energy Exploration & Exploitation* · Volume 24 · Number 1-2 · pp. 113–130
36. Peter J. Schubel and Richard J. Crossley, (2012) "Wind Turbine Blade Design", University of Nottingham, Nottingham NG7 2RD, UK.
37. Pope, S. B. (2010). Turbulent Flows. New York: Cambridge University Press
38. Porté-Agel, F., Wu, Y.-T., Lu, H., & Conzemius, R. J. (2011). Large-eddy Simulation of Atmospheric Boundary Layer Flow through Wind Turbines and Wind Farms. Journal of Wind Engineering and Industrial Aerodynamics, 99, 154-168.
39. Qunfeng L, Et.Al. (2011) Study of CFD Simulation of A 3-D Wind Turbine. In: Materials for Renewable Energy Environment (Icmree). Vol. 1; 2011. P. 596–600.
40. Raethorae P., (2009), Wind turbine wake in atmospheric turbulence.Aalborg university.

41. Reynolds O (1883). An Experimental Investigation Of The Circumstances Which Determine Whether The Motion Of Water Shall Be Direct Or Sinuous, And Of The Law Of Resistance In Parallel Channels. Philosophical Transactions of the Royal Society of London. 174:935–982.
42. Reynolds O. (1895) On the Dynamical Theory of Incompressible Viscous Fluids and the Determination of the Criterion. Philosophical Transactions of the Royal Society of London (A); 186:123–164
43. Siraj Ahmed, (2011) "Design and Analysis of Horizontal Axis Wind Turbine Rotor", Maulana Azad National Institute of Technology, Bhopal.
44. Serhat Duran, (2005) "Computer- Aided design of Horizontal- axis wind turbine blades", Middle east technical university.
45. Shu Z.R., Q.S. Li and P.W. Chan (2015), "Statistical analysis of wind characteristics and wind energy potential in Hong Kong, *Energy conversion and management*, Vol.101, Pages 644-657.
46. Snel H. (2003). Review of Aerodynamics for Wind Turbines. Wind Energy. 6:203–211
47. Smagorinsky J. (1963) General Circulation Experiments with the Primitive Equations. *Monthly Weather Review*. 91:99–164.
48. Stull Rb. (1988) An Introduction To Boundary Layer Meteorology. *Kluwer Academic Publishers.*
49. Sonia Chalia and Manish Kumar, (2017).Experimental Study of Aerodynamic Characteristics of Airfoils Using Different Shaped Dimples. *The International Journal of Engineering and Science (IJES)*, Volume- 4, Issue- 1, Pages PP.13-17
50. Thamodharan B, Amzad Hossain and Rubiat Mustak (2016), Numerical analysis of effect of dimples on aerodynamics of an airfoil, *International Conference on Explorations and Innovations in Engineering & Technology*.
51. Tachos, N. S., Filios, A. E., & Margaris, D. P. (2010). A comparative numerical study of four turbulence models for the prediction of horizontal axis wind turbine flow. *Journal of Mechanical Engineering Science*, 224.
52. Usha Rao K & Kishore VVN. (2009). Wind Power Technology Diffusion Analysis in Selected States of India. *Renewable Energy*; 34: 983–88
53. Versteeg, H and Malalasekera, W. (2007). An Introduction to Computational Fluid Dynamics, The finite volume method, 2nd edition. Pearson Education Limited

54. White Fm. (2009) Fluid Mechanics (Sixth Edition). *Mcgraw-Hill*;
55. Wilcox Dc (2006). Turbulence Modeling In CFD. DCW; *Mcgraw-Hill*
56. Wubow S, Sitzki L, Hahm T. (2007) 3d Simulation of the Turbulent Wake Behind A Wind Turbine. *Journal of Physics Conference Series* 75; 012033.
57. Yanfeng Zhaoa, Dilip A.,and Shah. J. (2016) Experimental studies of dimpled surface effect on the performance of linear cascade under different incidence angles. *Procedia CIRP* 56 137 – 142

Webpage References

1. http:// interface.vortexfdc.com**:** interface.vortexfdc.com **A**nnual Average wind speed contour of Horn of Africa. Vortex Interface, February 2nd ,2019,
2. http:// airfoilstools.com, Airfoil Tools, Aug-3, 2019.
3. https://www.google.com/maps/place/Weter. Geographical Location of the Site, Google Map. June,2019

APPENDIX

A -1 Aerodynamic Property of S830, S827, Sg6041and Sg6050 Airfoils

Table: Legend

(S-830-nr) NREL's S830 AIRFOIL
(S827-nr) NREL's S830 AIRFOIL
(Sg6041-il)SG6041
(Sg6050-il) SG6050

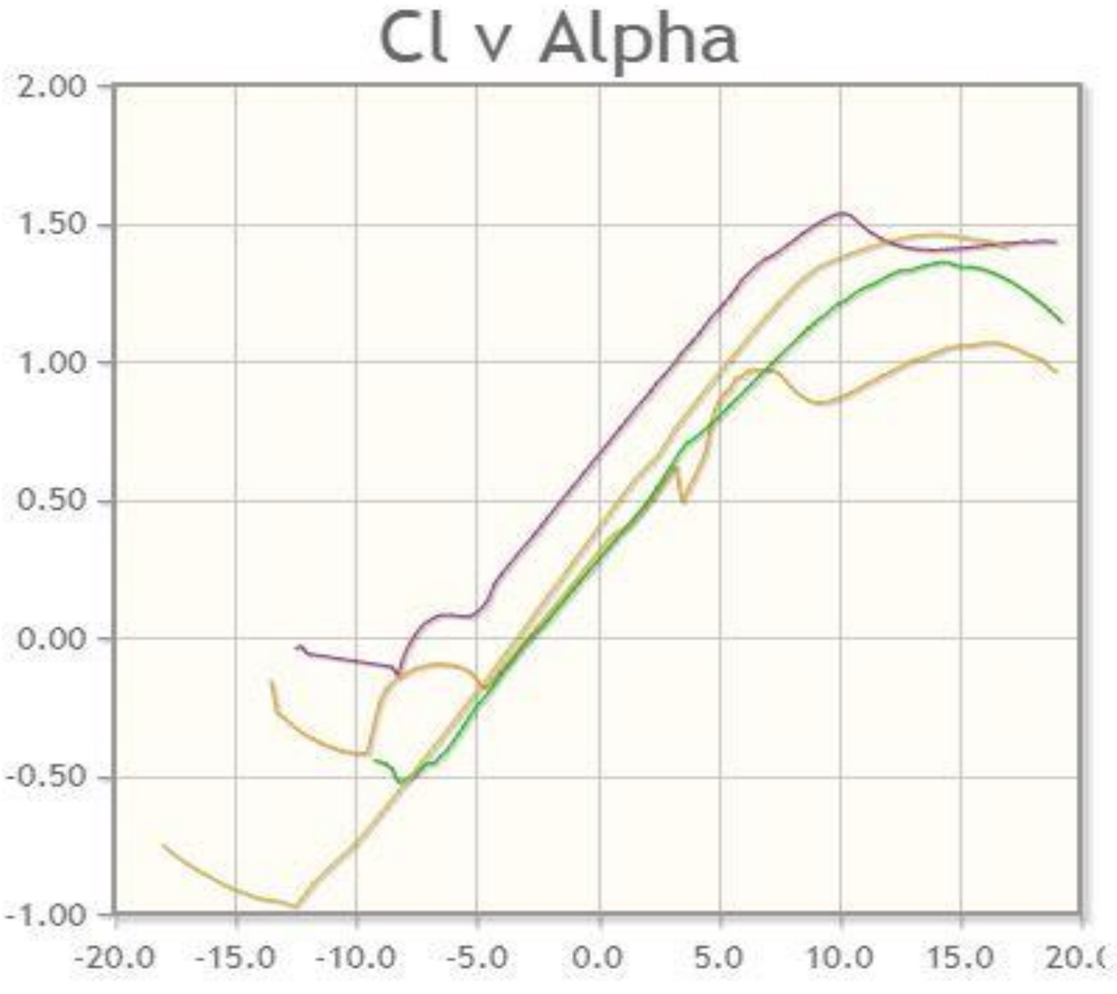

Fig:Cl versus AOA (Aerofoiltools.com, 2019)

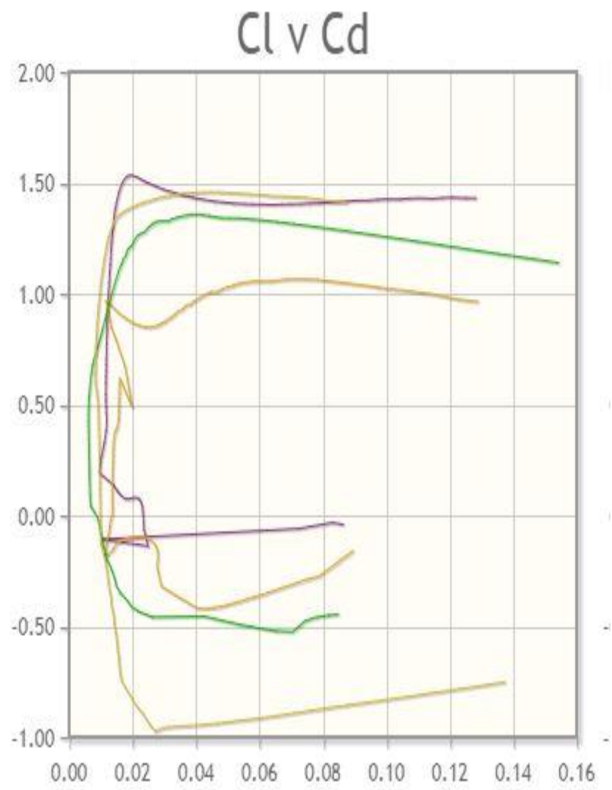

Fig: cl versus cd (*Aerofoiltools*.com, *2019*)

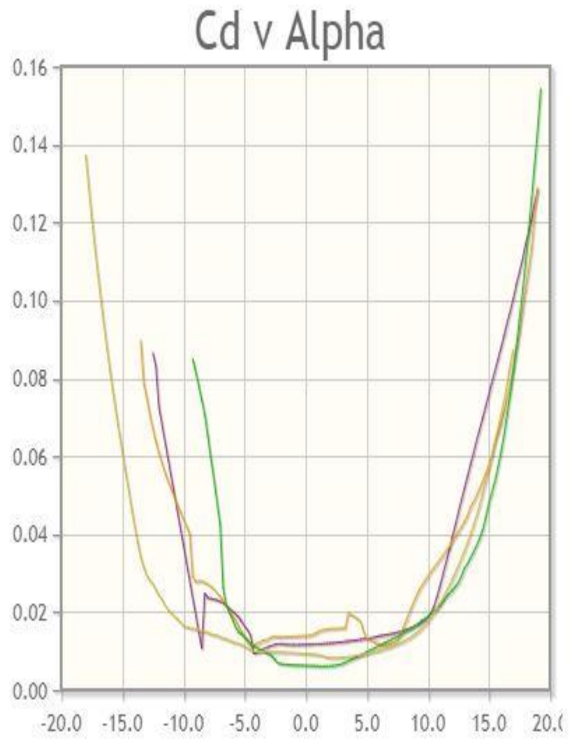

Fig: cd versus AOA (*Aerofoiltools*.com, *2019*)

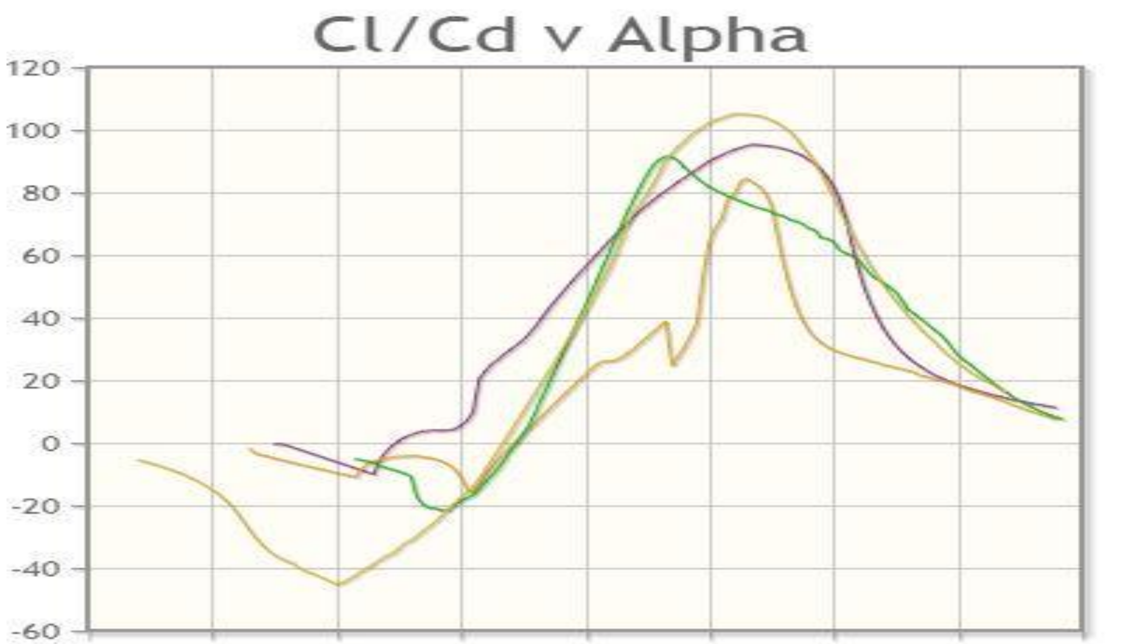

Fig: Cl/Cd versus AOA (*Aerofoiltools.com*, *2019*)

A-2 ANSYS FLUENT Result Plots

For Baseline Model

Lift Coefficient

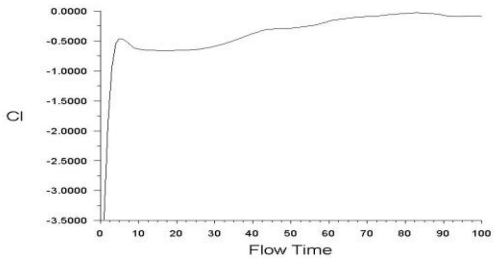

Fig Baseline lift coefficient at **α= -5^{0}**

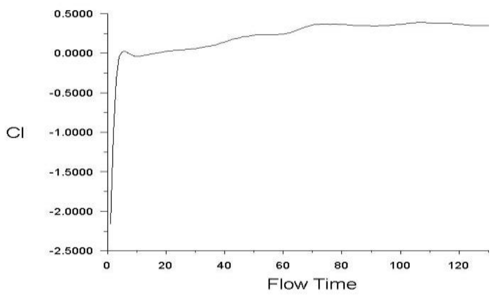

Fig Baseline lift coefficient at **α= 0^{0}**

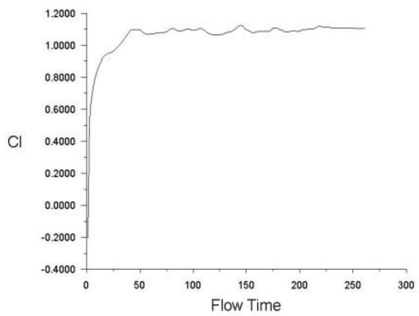

Fig Baseline lift coefficient at **α= 5^{0}**

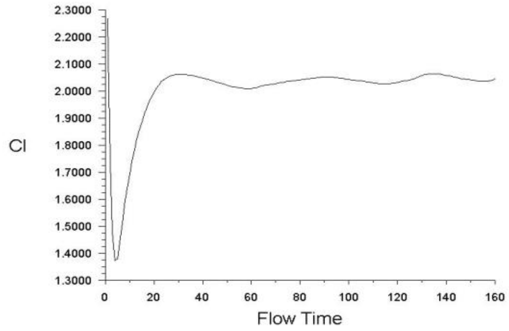

Fig Baseline lift coefficient at **α= 10^{0}**

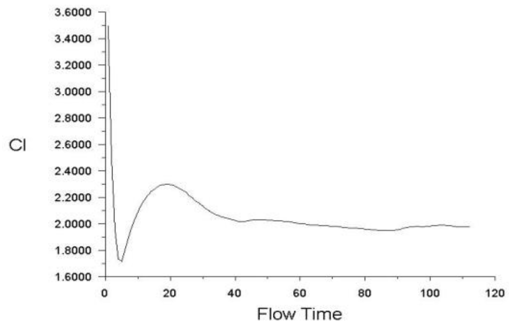

Fig Baseline lift coefficient at **α= 15^{0}**

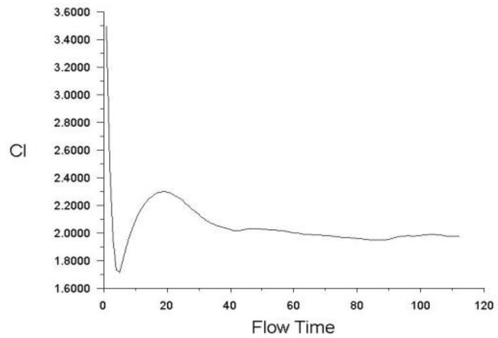

Fig Baseline lift coefficient at **α= 20^{0}**

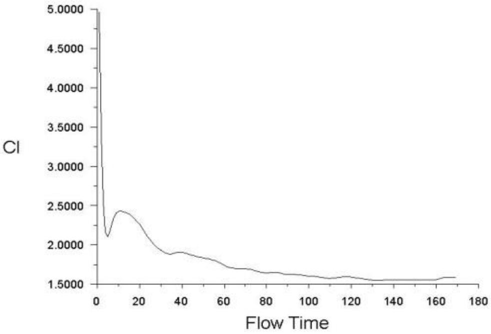

Fig Baseline lift coefficient at **α= 25^0**

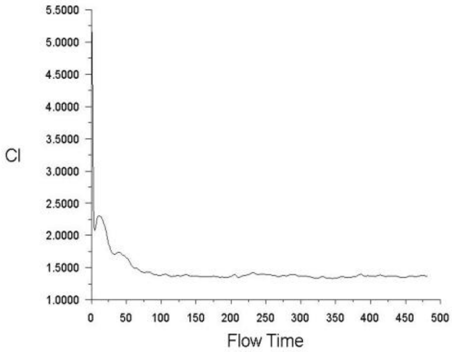

Fig Baseline lift coefficient at **α= 30^0**

Drag Coefficient

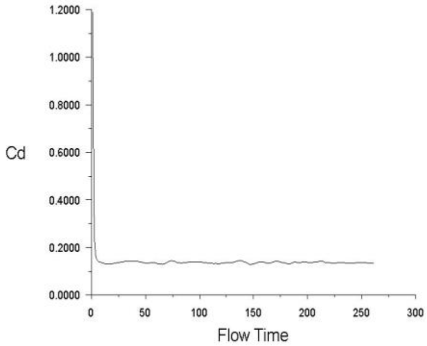

Fig Baseline Drag coefficient at **α= 0^0**

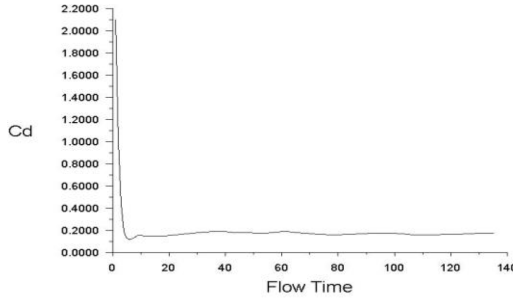

Fig Baseline Drag coefficient at **α= 5^0**

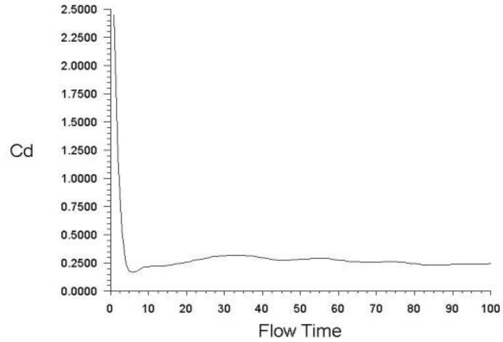

Fig Baseline Drag coefficient at **α= 10^0**

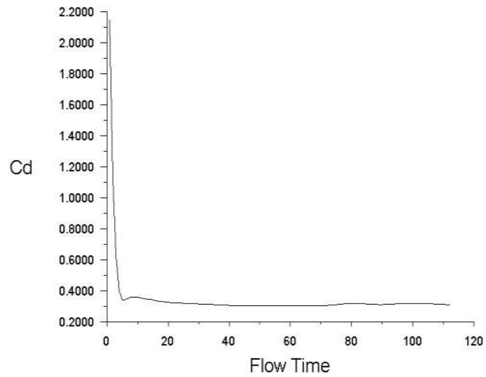

Fig Baseline Drag coefficient at **α= 15^0**

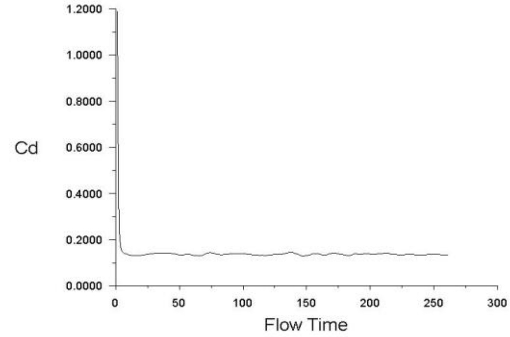

Fig Baseline Drag coefficient at **α= 20^0**

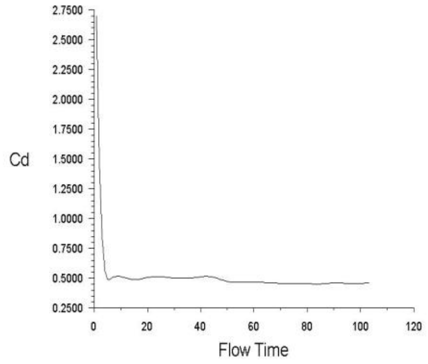

Fig Baseline Drag coefficient at **α= 25^0**

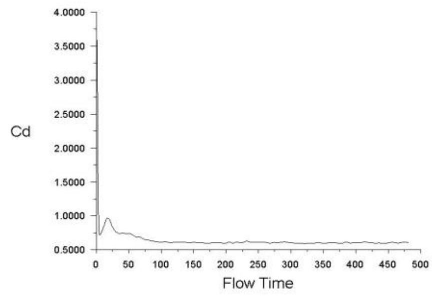

Fig Baseline Drag coefficient at **α= 30^0**

CONFIG#1 BLADE

Lift Coefficient

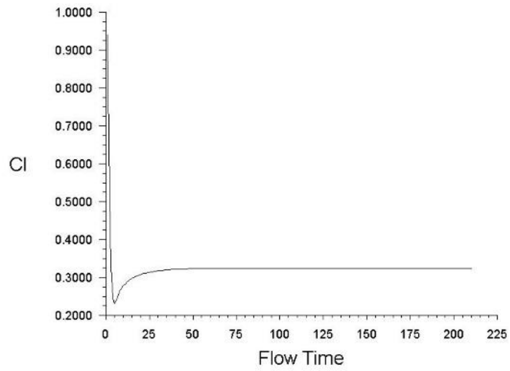

Fig Config#1 lift coefficient at **α= 0^0**

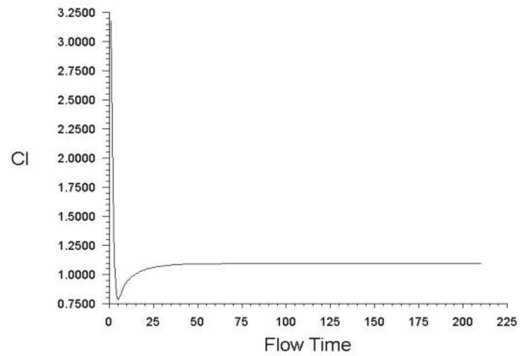

Fig Config#1 lift coefficient at **α= 5^0**

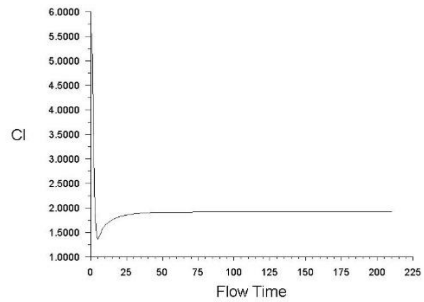

Fig Config#1 lift coefficient at **α= 10^0**

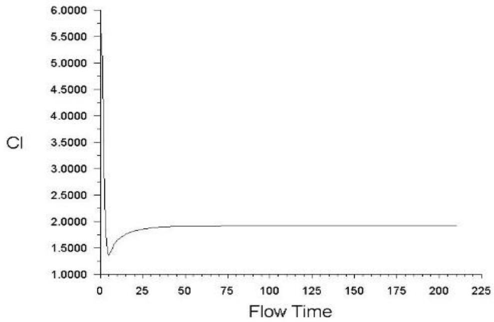

Fig Config#1 lift coefficient at **α= 15^{0}**

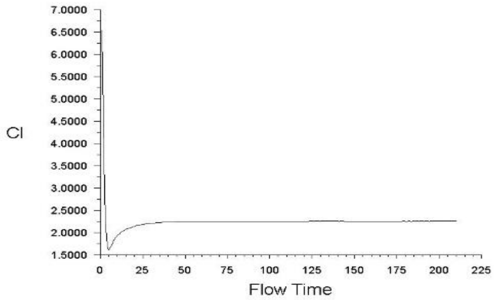

Fig Config#1 lift coefficient at **α= 20^{0}**

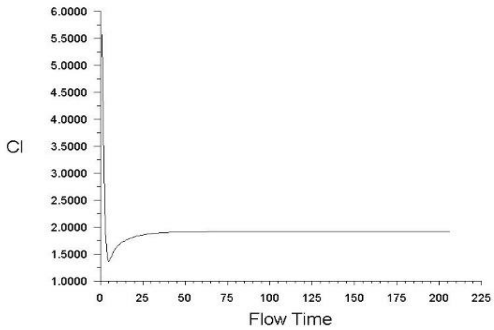

Fig Config#1 lift coefficient at **α= 25^{0}**

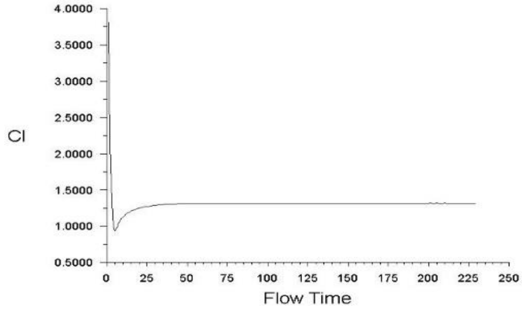

Fig Config#1 lift coefficient at **α= 30^{0}**

Drag Coefficient

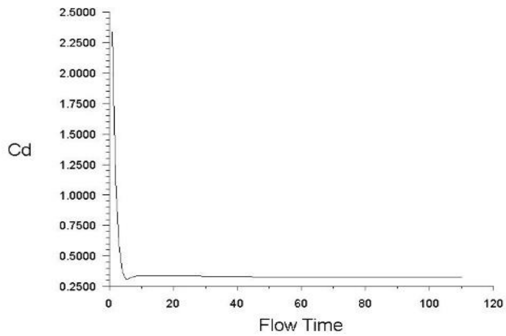

Fig Config#1 drag coefficient at **α= -5^{0}**

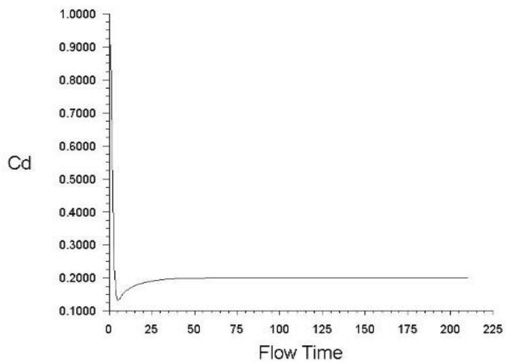

Fig Config#1 drag coefficient at **α= 0^{0}**

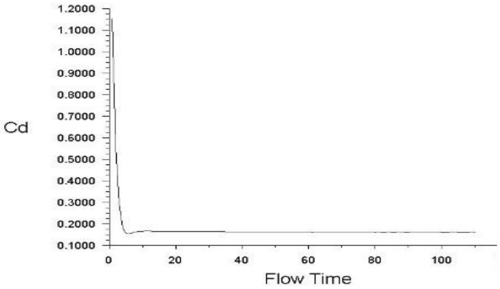

Fig Config#1 drag coefficient at **α= 5^{0}**

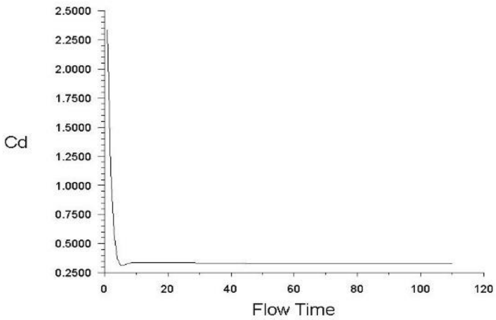

Fig Config#1 drag coefficient at **α= 10^{0}**

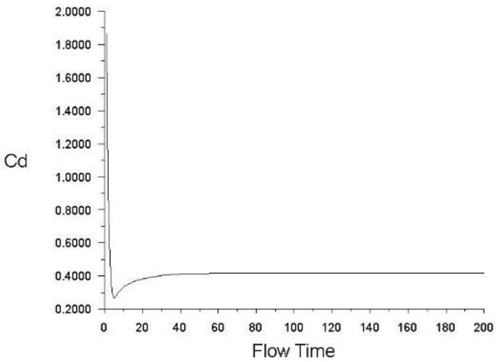

Fig Config#1 drag coefficient at **α= 15^{0}**

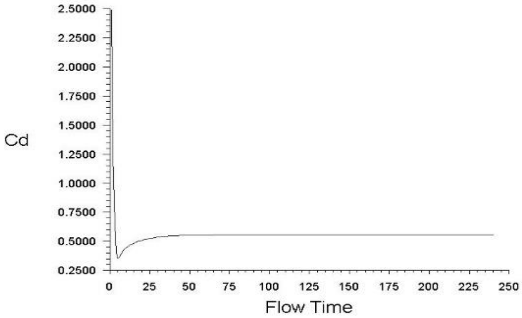

Fig Config#1 drag coefficient at **α= 20^{0}**

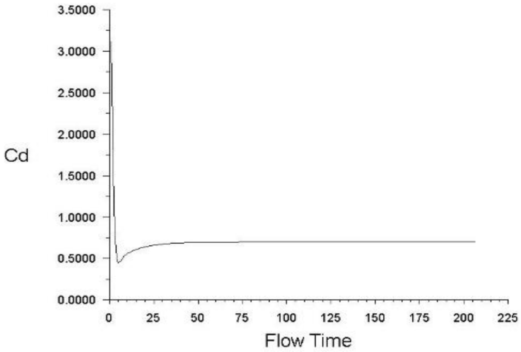

Fig Config#1 drag coefficient at **α= 25^{0}**

CONFIG #2 Blade

Lift coefficient

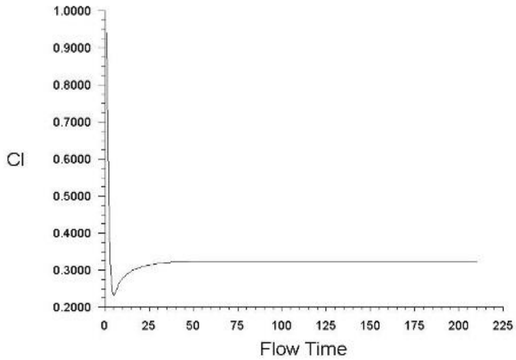

Fig Config#2 lift coefficient at **α= 0^{0}**

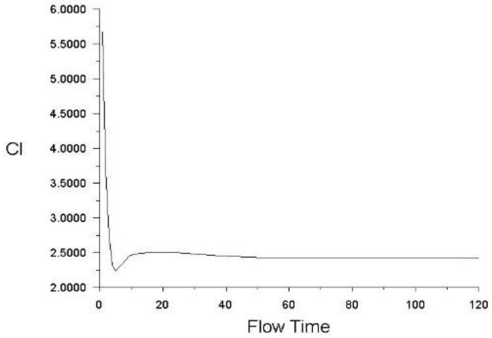

Fig Config#2 lift coefficient at **α= 5^{0}**

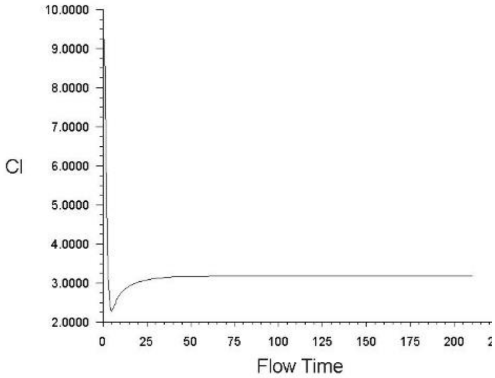

Fig Config#2 lift coefficient at **α= 10^{0}**

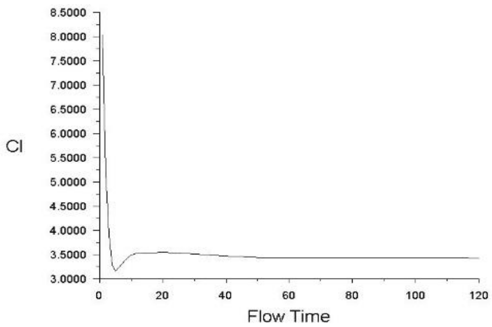

Fig Config#2 lift coefficient at **α= 15^{0}**

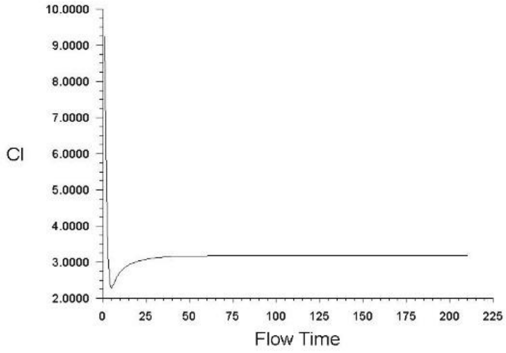

Fig Config#2 lift coefficient at **α= 20^{0}**

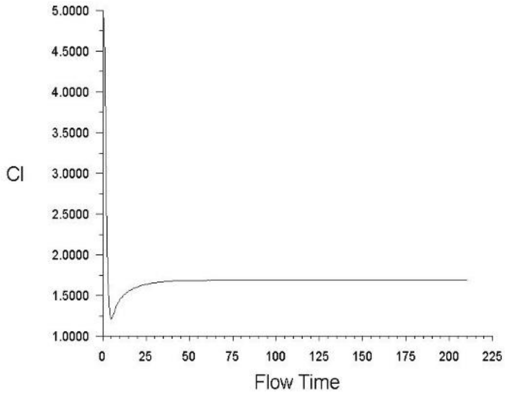

Fig Config#2 lift coefficient at **α= 25^{0}**

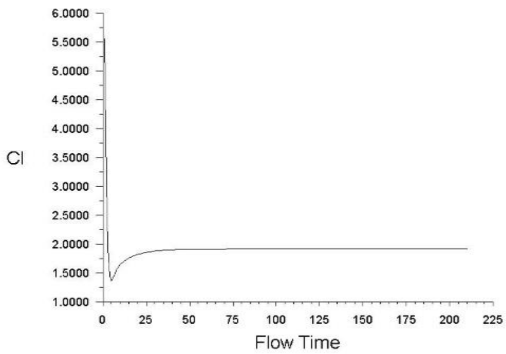

Fig Config#2 lift coefficient at **α= 30^{0}**

Drag Coefficient

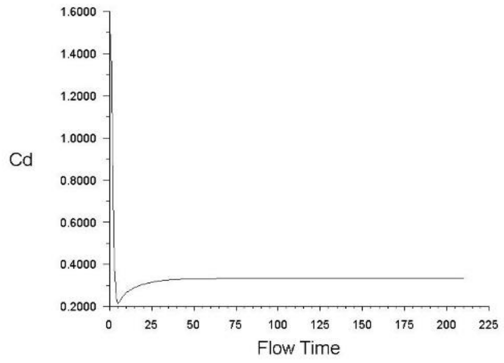

Fig Config#2 drag coefficient at **α= -5⁰**

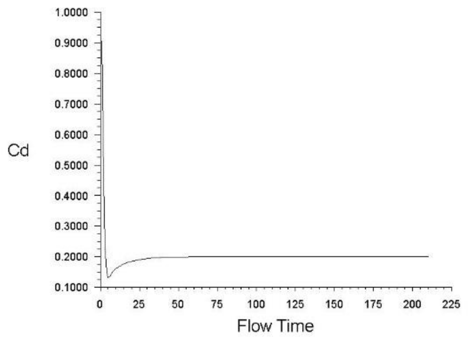

Fig Config#2 drag coefficient at **α= 0⁰**

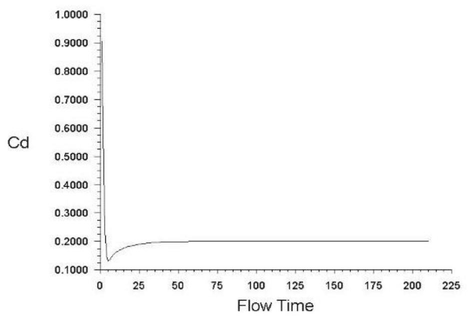

Fig Config#2 drag coefficient at **α= 5⁰**

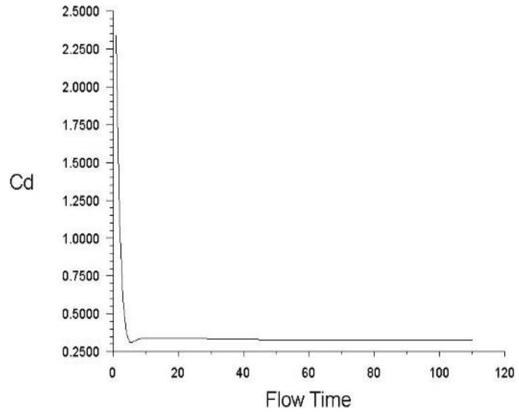

Fig Config#2 drag coefficient at **α= 10⁰**

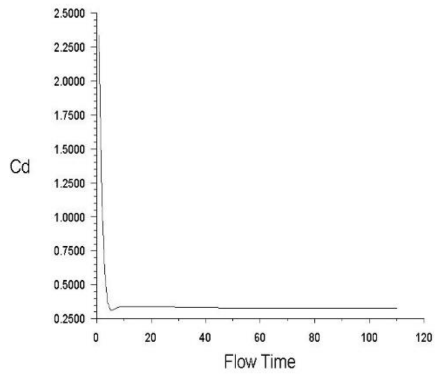

Fig Config#2 drag coefficient at **α= 15⁰**

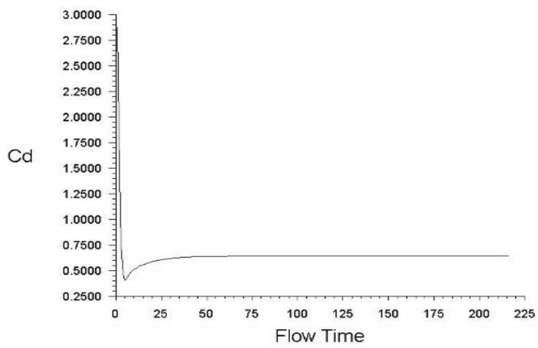

Fig Config#2 drag coefficient at **α= 20⁰**

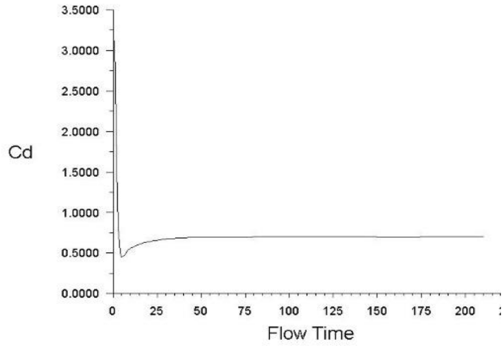

Fig Config#2 drag coefficient at **α= 25⁰**

CONFIG#3 BLADE

Lift coefficient

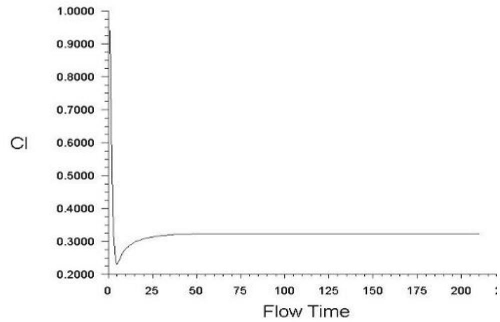

Fig Config#3 lift coefficient at **α= 0⁰**

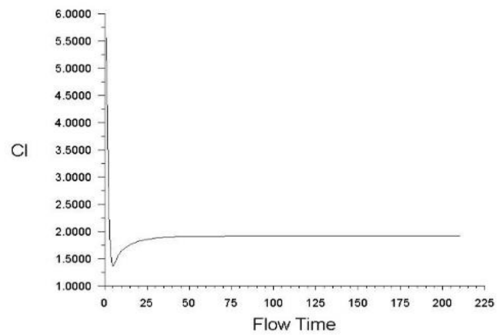

Fig Config#3 lift coefficient at **α= 5⁰**

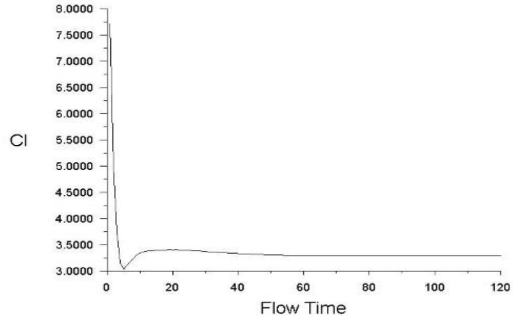

Fig Config#3 lift coefficient at **α= 15⁰**

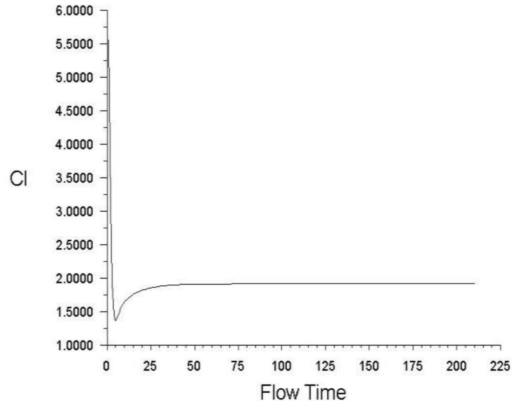

Fig Config#3 lift coefficient at **α= 25⁰**

Drag Coefficient

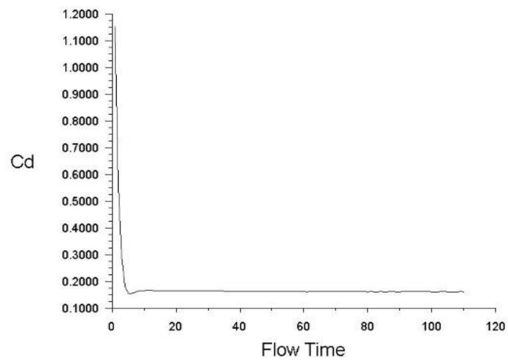

Fig Config#3 drag coefficient at **α= 5⁰**

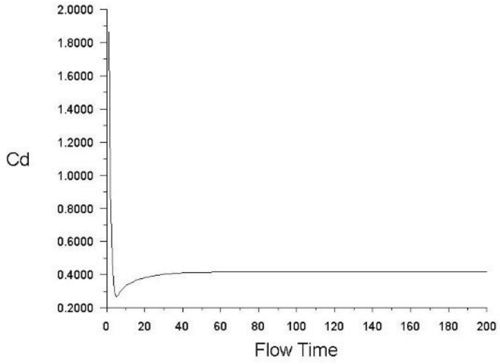

Fig Config#3 drag coefficient at **$\alpha = 15^{0}$**

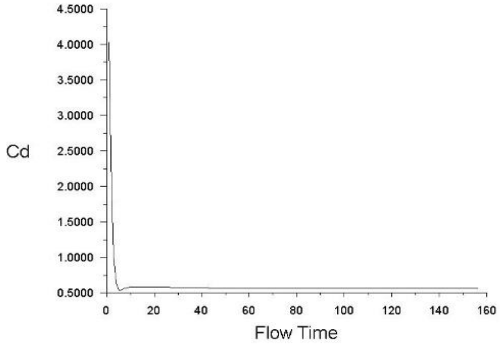

Fig Config#3 drag coefficient at **$\alpha = 20^{0}$**

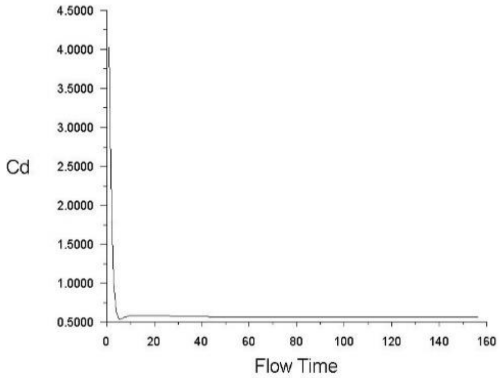

Fig Config#3 drag coefficient at **$\alpha = 30^{0}$**

CONFIG#4 BLADE

Lift Coefficient

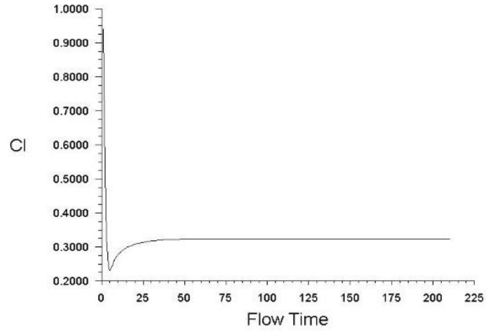

Fig Config#4 lift coefficient at **$\alpha = 0^{0}$**

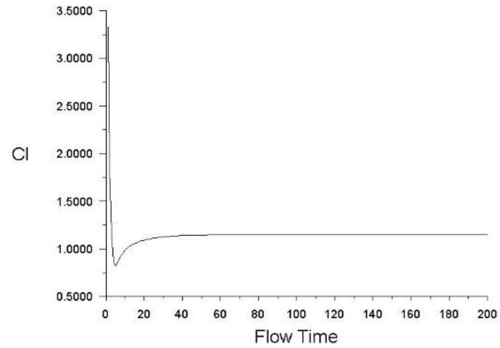

Fig Config#4 lift coefficient at **$\alpha = 5^{0}$**

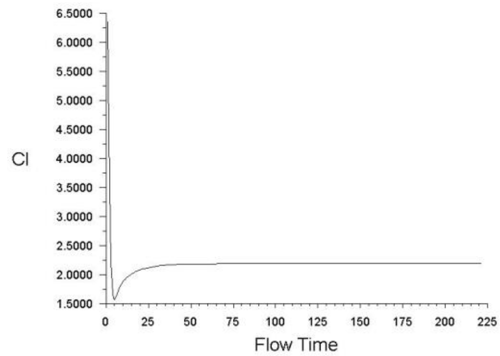

Fig Config#4 lift coefficient at **$\alpha = 15^{0}$**

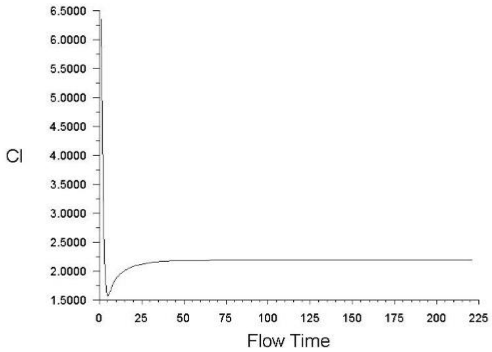

Fig Config#4 lift coefficient at **α= 20^{0}**

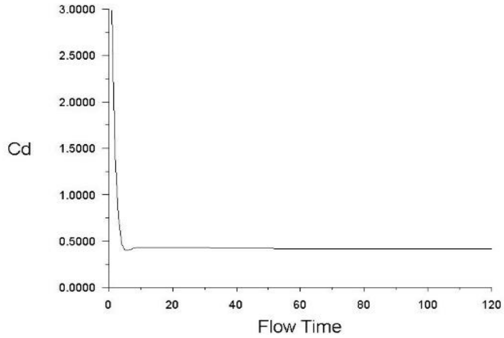

Fig Config#4 drag coefficient at **α= 15^{0}**

Drag Coefficient

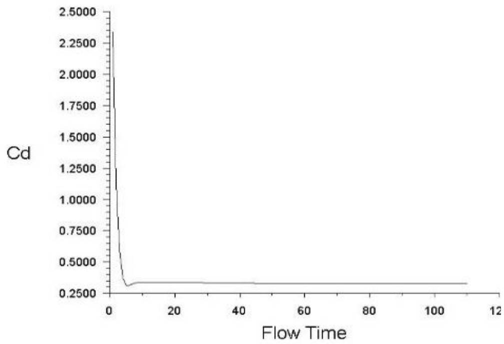

Fig Config#4 drag coefficient at **α= -5^{0}**

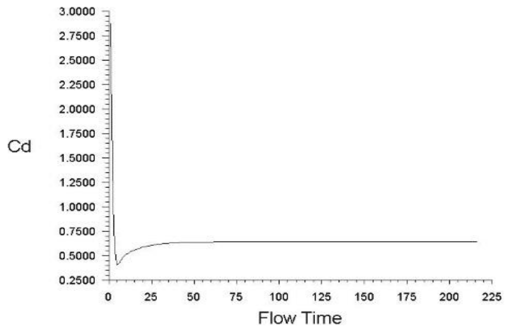

Fig Config#4 drag coefficient at **α= 20^{0}**

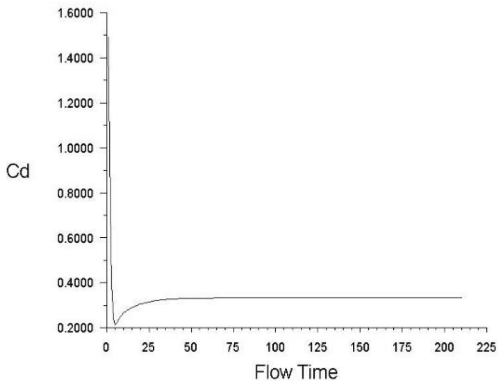

Fig Config#4 drag coefficient at **α= 10^{0}**

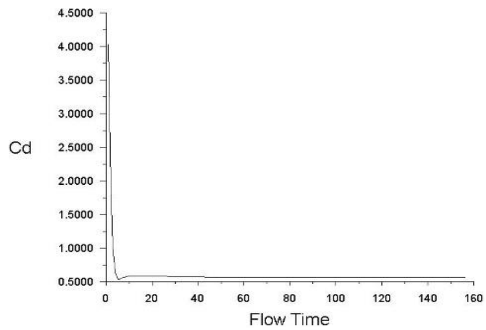

Fig Config#4 drag coefficient at **α= 25^{0}**

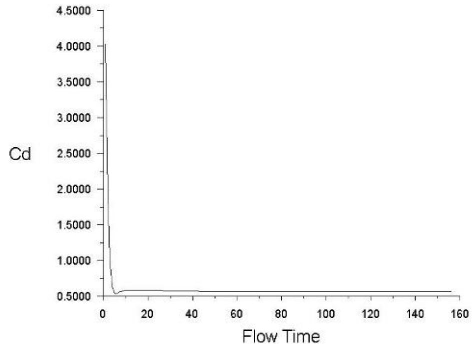

Fig Config#4 drag coefficient at **α= 30^0**

CONFIG #5 BLADE

Lift Coefficient

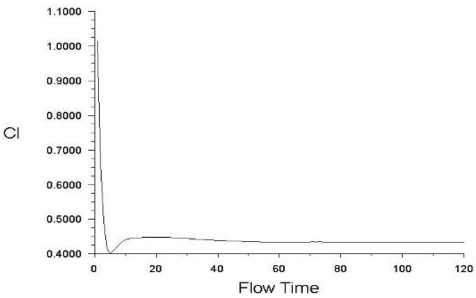

Fig Config#5 lift coefficient at **α= 0^0**

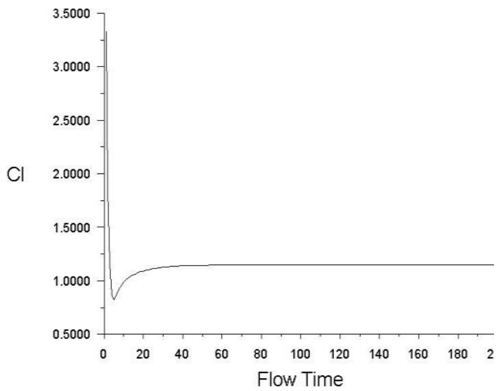

Fig Config#5 lift coefficient at **α= 5^0**

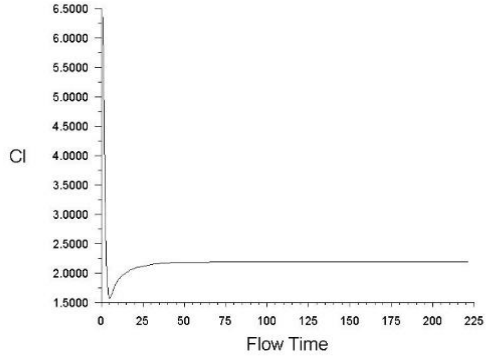

Fig Config#5 lift coefficient at **α= 15^0**

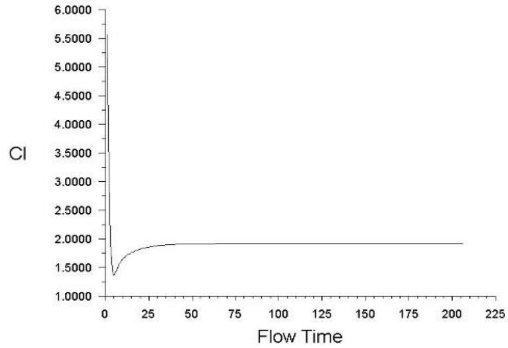

Fig Config#5 lift coefficient at **α= 20^0**

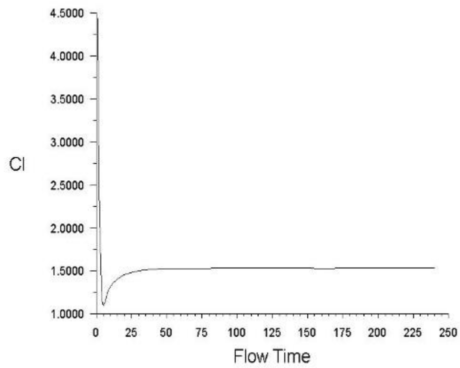

Fig Config#5 lift coefficient at **α= 25^0**

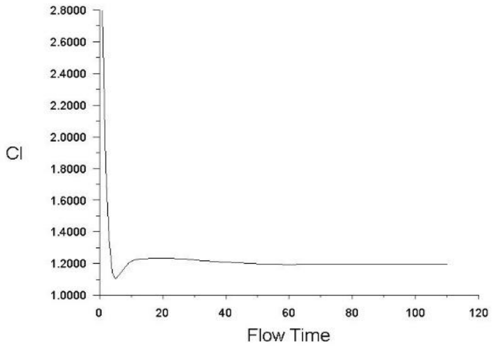

Fig Config#5 lift coefficient at **α= 30⁰**

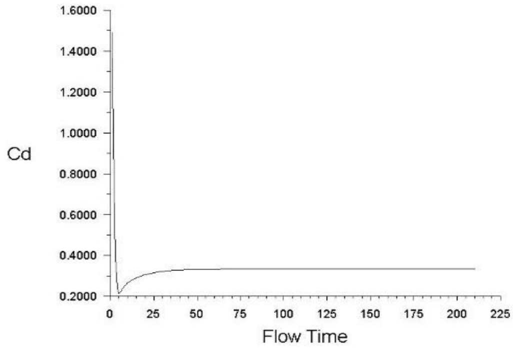

Fig Config#5 lift coefficient at **α= 15⁰**

Drag coefficient

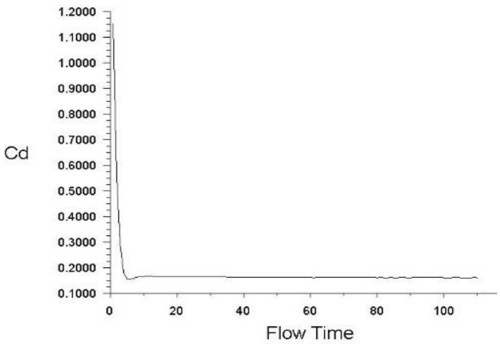

Fig Config#5 lift coefficient at **α= 0⁰**

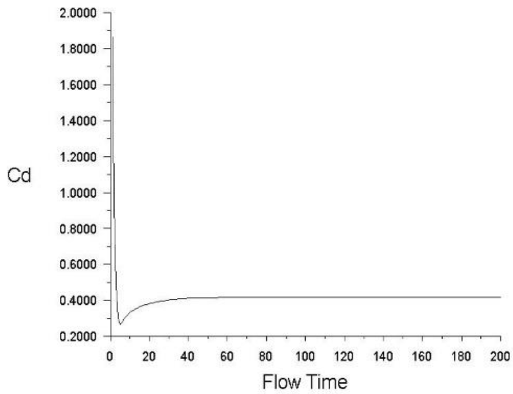

Fig Config#5 lift coefficient at **α= 20⁰**

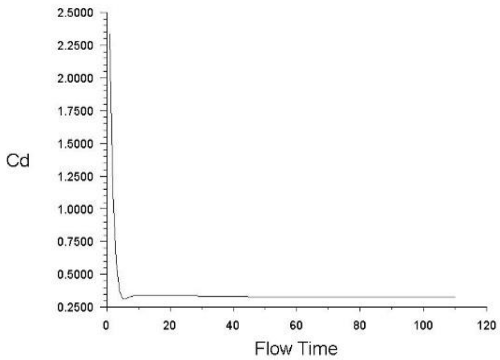

Fig Config#5 lift coefficient at **α= 10⁰**

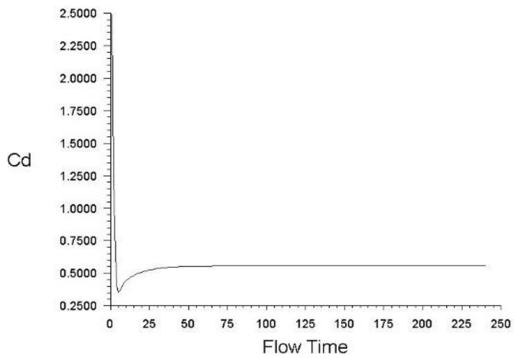

Fig Config#5 lift coefficient at **α= 25⁰**

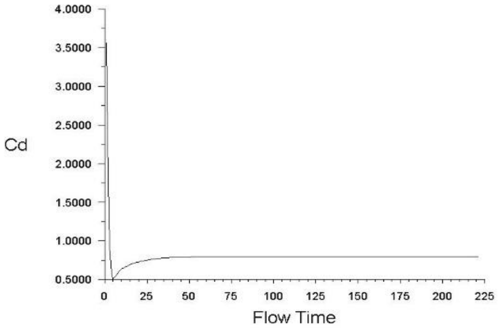

Fig Config#5 lift coefficient at **α= 30^0**

CONFIG #6 Blade
Lift coefficient

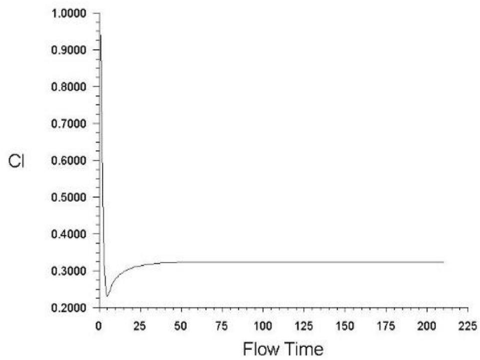

Fig Config#6 lift coefficient at **α= 0^0**

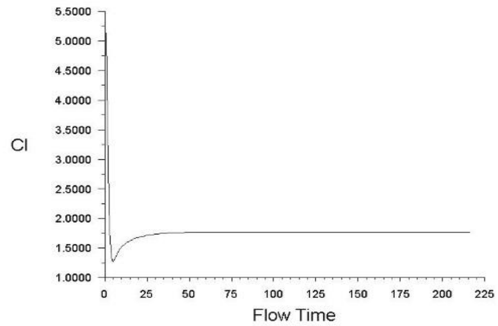

Fig Config#6 lift coefficient at **α= 5^0**

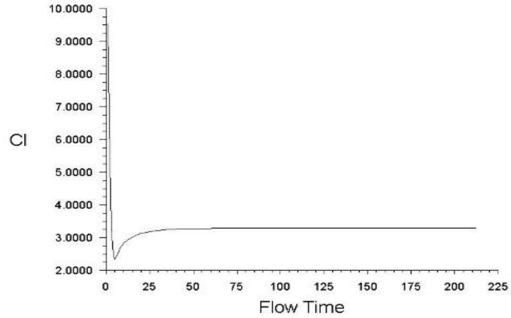

Fig Config#6 lift coefficient at **α= 10^0**

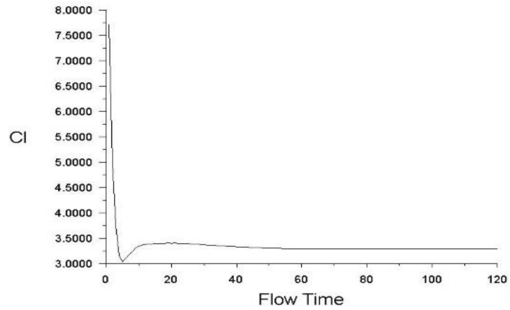

Fig Config#6 lift coefficient at **α= 15^0**

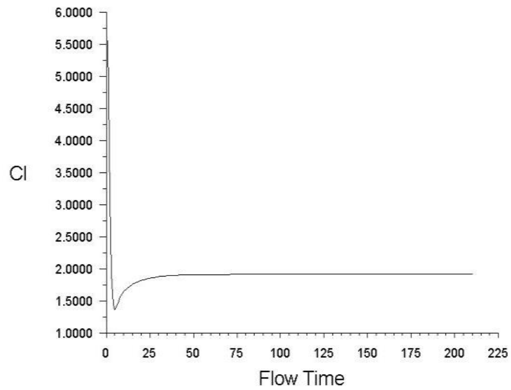

Fig Config#6 lift coefficient at **α= 20^0**

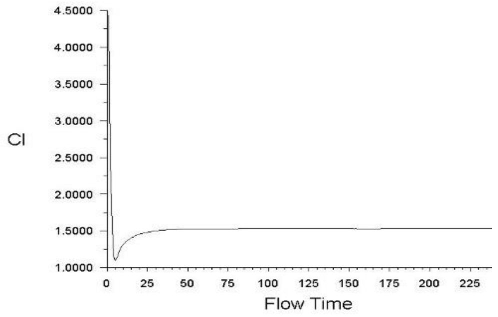

Fig Config#6 lift coefficient at **α= 30^0**

Drag coefficient

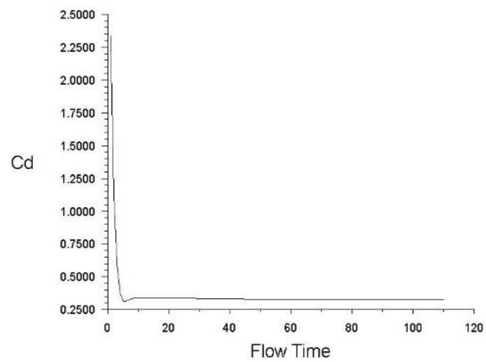

Fig Config#6 drag coefficient at **α= -5^0**

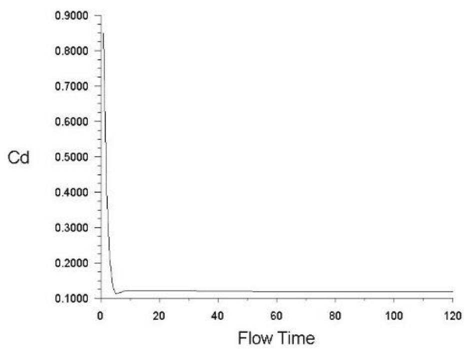

Fig Config#6 drag coefficient at **α= 0^0**

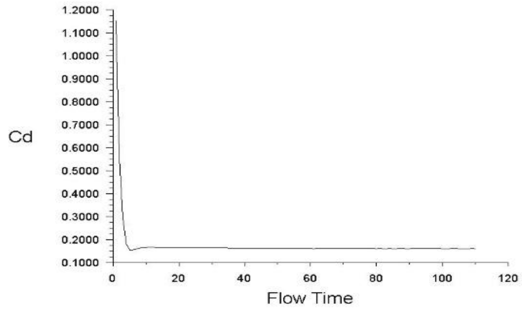

Fig Config#6 drag coefficient at **α= 5^0**

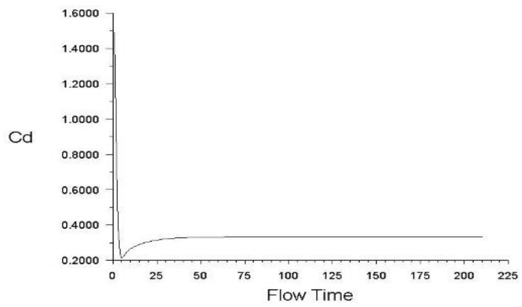

Fig Config#6 drag coefficient at **α= 10^0**

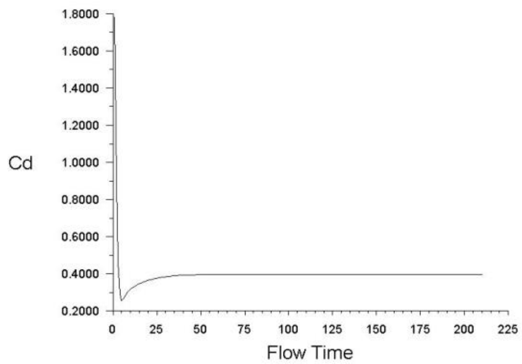

Fig Config#6 drag coefficient at **α= 15^0**

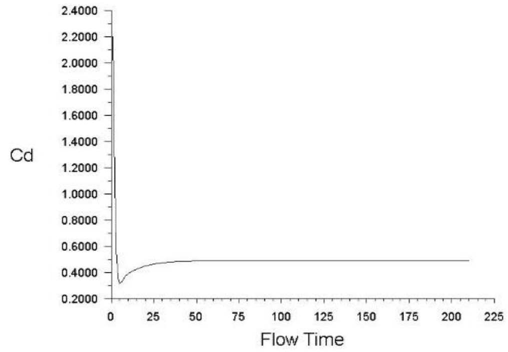

Fig Config#6 drag coefficient at **α= 20^0**

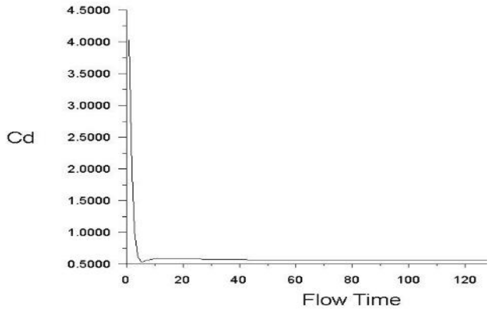

Fig Config#6 drag coefficient at **α= 25^0**

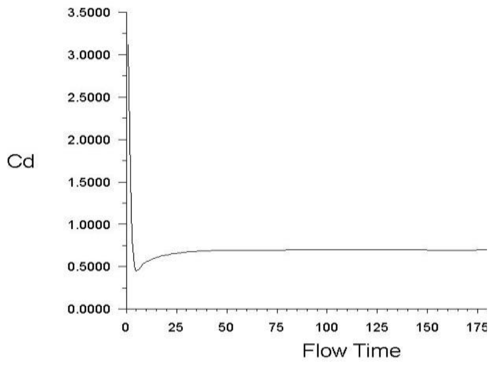

Fig Config#6 drag coefficient at **α= 30^0**

A-3 Grid Independent Test Setup

Details of "Mesh"

Sizing	
Size Function	Proximity and Curvature
Relevance Center	Medium
Initial Size Seed	Active Assembly
Smoothing	Medium
Transition	Slow
Span Angle Center	Fine
Curvature Normal A...	Default (18.0 °)
Num Cells Across G...	Default (3)
Proximity Size Functio...	Faces and Edges
Min Size	3.0 mm
Proximity Min Size	Default (0.130180 mm)
Max Face Size	Default (13.0180 mm)
Max Tet Size	Default (26.0360 mm)
Growth Rate	Default (1.20)
Automatic Mesh Base...	On
Defeature Size	Default (6.5091e-002 mm
Minimum Edge Length	7.48270 mm
Inflation	
Use Automatic Inflation	Program Controlled
Inflation Option	Smooth Transition
Transition Ratio	0.272
Maximum Layers	5
Growth Rate	1.2
Inflation Algorithm	Pre
View Advanced Options	No
Assembly Meshing	
Advanced	
Statistics	
Nodes	75892
Elements	436911
Mesh Metric	None

Fig: Mesh #1 setup

Details of "Mesh"

Defaults	
Sizing	
Size Function	Proximity and ...
Relevance Center	Medium
Initial Size Seed	Active Assembly
Smoothing	Medium
Transition	Slow
Span Angle Center	Fine
Curvature Normal Angle	Default (18.0 °)
Num Cells Across Gap	Default (3)
Proximity Size Function Sources	Faces and Ed...
Min Size	3.0 mm
Proximity Min Size	Default (0.130...
Max Face Size	Default (13.01...
Max Tet Size	Default (26.03...
Growth Rate	Default (1.20)
Automatic Mesh Based Defeaturing	On
Defeature Size	Default (6.509...
Minimum Edge Length	7.48270 mm
Inflation	
Use Automatic Inflation	Program Cont...
Inflation Option	Smooth Transi...
Transition Ratio	0.272
Maximum Layers	5
Growth Rate	1.2
Inflation Algorithm	Pre
View Advanced Options	No
Assembly Meshing	
Advanced	
Statistics	
Nodes	149757
Elements	855713
Mesh Metric	None

Fig: Mesh-2 setup

Details of "Mesh"

Display	
Defaults	
Sizing	
Size Function	Proximity and Curvature
Relevance Center	Medium
Initial Size Seed	Active Assembly
Smoothing	Medium
Transition	Slow
Span Angle Center	Fine
Curvature Normal Angle	Default (18.0 °)
Num Cells Across Gap	Default (3)
Proximity Size Function Sources	Faces and Edges
Min Size	3.0 mm
Proximity Min Size	Default (0.130180 mm)
Max Face Size	Default (13.0180 mm)
Max Tet Size	Default (26.0360 mm)
Growth Rate	Default (1.20)
Automatic Mesh Based Defeaturing	On
Defeature Size	Default (6.5091e-002 mm)
Minimum Edge Length	7.48270 mm
Inflation	
Use Automatic Inflation	Program Controlled
Inflation Option	Smooth Transition
Transition Ratio	0.272
Maximum Layers	5
Growth Rate	1.2
Inflation Algorithm	Pre
View Advanced Options	No
Assembly Meshing	
Advanced	
Statistics	
Nodes	337007
Elements	1942807
Mesh Metric	None

Fig: Mesh#3 setup

Details of "Mesh"

Sizing	
Size Function	Proximity and Curvature
Relevance Center	Medium
Initial Size Seed	Active Assembly
Smoothing	Medium
Transition	Slow
Span Angle Center	Fine
Curvature Normal A...	Default (18.0 °)
Num Cells Across G...	Default (3)
Proximity Size Functio...	Faces and Edges
Min Size	3.0 mm
Proximity Min Size	Default (0.130180 mm)
Max Face Size	Default (13.0180 mm)
Max Tet Size	Default (26.0360 mm)
Growth Rate	Default (1.20)
Automatic Mesh Base...	On
Defeature Size	Default (6.5091e-002 mm)
Minimum Edge Length	7.48270 mm
Inflation	
Assembly Meshing	
Advanced	
Statistics	
Nodes	388188
Elements	2234257
Mesh Metric	None

Fig: Mesh#4 setup

Details of "Mesh"

Sizing	
Size Function	Proximity and Curvature
Relevance Center	Medium
Initial Size Seed	Active Assembly
Smoothing	Medium
Transition	Slow
Span Angle Center	Fine
Curvature Normal A...	Default (18.0 °)
Num Cells Across G...	Default (3)
Proximity Size Functio...	Faces and Edges
Min Size	3.0 mm
Proximity Min Size	Default (0.130180 mm)
Max Face Size	Default (13.0180 mm)
Max Tet Size	Default (26.0360 mm)
Growth Rate	Default (1.20)
Automatic Mesh Base...	On
Defeature Size	Default (6.5091e-002 mm)
Minimum Edge Length	7.48270 mm
Inflation	
Use Automatic Inflation	Program Controlled
Inflation Option	Smooth Transition
Transition Ratio	0.272
Maximum Layers	5
Growth Rate	1.2
Inflation Algorithm	Pre
View Advanced Options	No
Assembly Meshing	
Advanced	
Statistics	
Nodes	911696
Elements	5258523
Mesh Metric	None

Fig: Mesh#5 setup